Optimal Operation of Solar Energy Driven Single-Double-Effect Absorption Chiller

太陽熱で駆動する一重二重効用吸収冷凍機の最適運用に関する研究

February 2019

ARNAS

アルナス

Optimal Operation of Solar Energy Driven Single-Double-Effect Absorption Chiller

太陽熱で駆動する一重二重効用吸収冷凍機の最適運用に関する研究

February 2019

Waseda University

Graduate School of Fundamental Science and Engineering

Department of Applied Mechanics,

Research on Dynamics and Control of Mechanical Systems

ARNAS

アルナス

Abstract

Absorption chillers constitute a valuable option for utilising solar energy. Specifically, when installed in tropical regions, this technology ideally matches the needs for refrigeration and air-conditioning because of the abundance of solar energy throughout the year. A single-double-effect absorption chiller combines the single and double-effect configurations to compensate for the unpredictable instantaneous availability of solar radiation and cooling load fluctuations. By combining system in one unit several advantages can be achieved, such as compact dimension, back-up/second system has a quick response, easy to synchronize both systems. However, this configuration could be associated with other operability issues, particularly, the operation strategy of this system becomes more complex.

This study presents the most advanced combined solar-cooling system based on the criteria of high utilisation of waste heat/solar energy and low primary energy consumption, and clarifies the possibility of additional performance improvements that lead to significant primary energy saving. Specifically, new system configuration of a single-double-effect absorption chiller for solar-cooling applications is under analysis. The single-double-effect absorption chiller is modelled for simulating the steady-state and the transient or dynamic conditions, and the model is validated by experimental data in order to confidently search for the best performance operation with high reliability. A newly developed performance maximisation method is suggested, where the operation performance of this system can be improved by manipulating the absorber outlet solution flow rate and the solution distribution ratio, achieving a significant reduction of the primary energy consumption, without any additional cost. Based on this method, a suitable operation strategy for controlling this advanced system configuration in various operation conditions is suggested to minimise the primary energy consumption during real operation.

Keywords: absorption chiller, operation strategy, internal parameter, single-effect, double-effect, solar cooling.

Acknowledgement

In the name of Allah. First and above all, all praise be to Allah the lord of the worlds, on whom ultimately we depend for sustenance and guidance.

I would like to thank to my parents, my parents in law and my grandmother for their prayer and support from the beginning of my Doctoral degree at Waseda University until reaching this step. And also thank my beloved wife Mirta Wardhani Soeripto who always listened to my research problem patiently, my sons who gave me more energy to finish my study: Alkhalifi Hiroshi Lubis, and Arroyyan Naoki Lubis. Thanks to my family for their help: bang Dedi, Pian, Doni, Mpok Wani, Raffa, DJ, Ilham, and Arfah.

My sincere gratitude to my advisor Prof. Kiyoshi Saito for the continuous support of my Doctoral study and related research, for his patience, time, motivation, and immense knowledge. His guidance and his kindness helped me in all the time research and writing of this Doctoral Thesis.

Besides my advisor, I would like to thank the rest of my thesis committee: Prof. Masafumi Katsuta, Prof. Hiroshi Muto, and Prof. Yoshiharu Amano for their comments and encouragement in the reviewing process.

My sincere thanks also go to Prof. Jongsso Jeong and Prof. Seiichi Yamaguchi for their help, assistance and discussion of various issues. Also, many thanks to Prof. Naoyuki Inoue for his valuable experience to help me construct the dynamic model and understand the operational strategy of the absorption machine.

Special thanks to my advisor Prof. Muhammad Idrus Alhamid and Prof. Nasruddin for their help and support, therefore, I entered and finished the Doctoral degree at Waseda University.

Thanks to Mr Hajime Yabase and Mr Akira Hirai for their valuable information about the single-double-effect absorption chiller system.

Many thanks to Asst. Prof. Niccolo Giannetti, Ohsaki-san, and Lisa Kuo for all their help regarding my study and my daily life problems.

I want to thank all of my friend in Saito Laboratory who helped me doing the Doctoral study: Kimura-san, Ohno-san, Nakanishi/Takahashi, Sakamoto, Hatada, Richard, Dane, Mark, Sholeh, and mas Hifni. Also, all my Pejaten's brother who supported me: Haolia, Babam, Isal, Hendra, Uji, Wiko, and Andi.

This research work was conducted by "Entrusted Business on the Technical Cooperation for Co-benefit Type Solar-aided Air-conditioning System in Indonesia during the Fiscal Years-2014" commissioned by Ministry of the Environment Japan, Research Institute for Science and Engineering (RISE) Waseda University as part of the research project of "Next generation heat pump technology" and Interdisciplinary Institute for Thermal Energy Conversion Engineering and Mathematics.

Table of contents

Nomenclature

A	area, m^2
C_p	specific heat, kJ/kgK
dt	delta time, s
h	specific enthalpy, kJ/kg
l	height, m
m	power function of parameter ratio, -
M	mass storage, kg
MC_p	heat capacity
P	pressure, kPa
PQ	percentage in charge, %
Q	heat transfer rate, kW
R	heat transfer resistance, m^2K/kW
Re	Renault number, -
RR	resistance ratio, -
T	temperature, ºC
UA	overall heat transfer coefficient, kW/K
U	overall heat transfer coefficient, kW/m^2K
V	Volumetric flow rate, m^3/h
Vl	volume, m^3
X	solution concentration, -
α	heat transfer coefficient, kW/m^2K
$\dot{m}$	mass flow rate, kg/s
ΔT	delta temperature, ºC
γ	solution distribution ratio, -
ρ	density, kg/m^3

Subscript

A	absorber
atm	atmosphere
avg	average
btm	bottom
C	condenser
CL	crystalllisation line
cw	cooling water
chw	chilled water
CON	conventional
DE	double-effect
E	evaporator
full	full
HTG	high-temperature generator
HHX	high-temperature solution heat exchanger
hw	hot water

in	inlet
inside	inside
LHX	low-temperature solution heat exchanger
LMTD	log mean temperature difference
LTG	low-temperature generator
M	mixer
M1	mixer 1
M2	mixer 2
Max	maximum
out	outlet
P2	solution pump 2
r	refrigerant
s	solution
S	separator
sat	saturation
SC	special condenser
ss	strong solution
STG	special-temperature generator
tb	tube
v	vapour
ws	weak solution

Chapter 1
Introduction

1. Research Background

The high daily temperatures in Asian tropical climates [1] (Fig. 1.1) necessitate air-conditioning systems, which create a thermal comfort zone for the daily indoor activities. During the hot season, the air-conditioning system is required even more. Consequently, the energy consumption of the building sector could increase and this would burden the energy load of a country. For example, in Singapore, the electricity demand of the building sector only for cooling is around 31% of the total electricity consumption [2]. Furthermore, approximately 40% of the total energy in the building sector is consumed by air-conditioning systems [3].

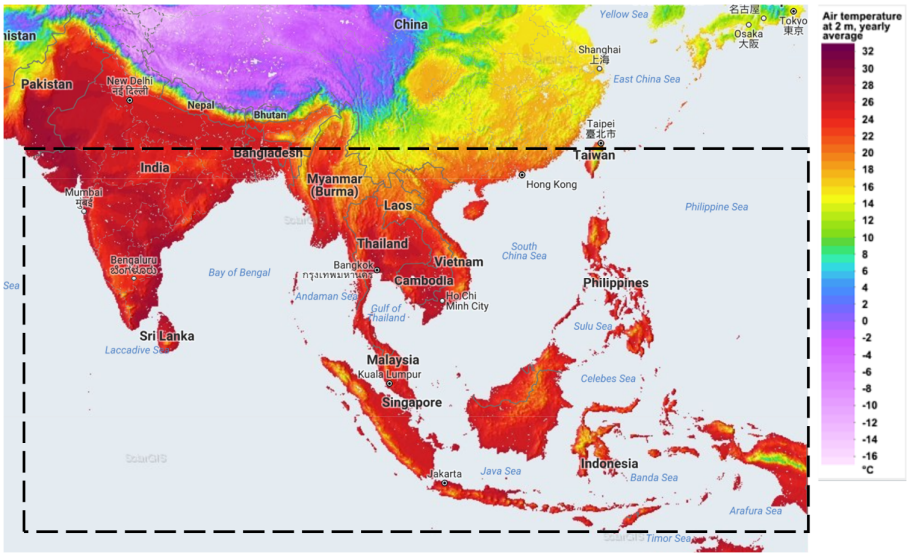

Fig. 1.1 Air temperature at 2 m, yearly average [4]

Due to the high electricity consumption of the building sector's cooling systems, solar energy is one of the most promising future alternative energy sources, because non-renewable energy, such as fossil fuels that are still in use, is limited and associated to environment issues. Moreover, solar energy can be obtained from nature without direct cost. Some tropical Asian countries are geographically aligned with the equator, and their locations are thus characterised by the abundant availability of solar energy throughout the year (Fig. 1.2). Tropical Asian countries have the potential for an average daily solar radiation of approximately 4–7 kWh/m^2/day [5–10].

The utilisation of solar energy indirectly reduces carbon dioxide emissions from power plants [10] and Asian tropical areas have a significant potential for using solar energy [12] [13]. Therefore, air-conditioning systems that can be driven by solar energy are excellent options for reducing the solar heat gains in the building sector [14], while that solar radiation absorbed by solar collector is also used to produce chilled water for the building.

As a thermally driven technology, absorption chillers can be efficiently driven by solar energy in a wide range of heat input temperatures [15]. Utilising solar energy for an absorption chiller system in Asian tropical areas comes along with the significant advantage of large availability of radiant heat, which constitutes a power source able to make up for the high ambient temperature throughout the year.

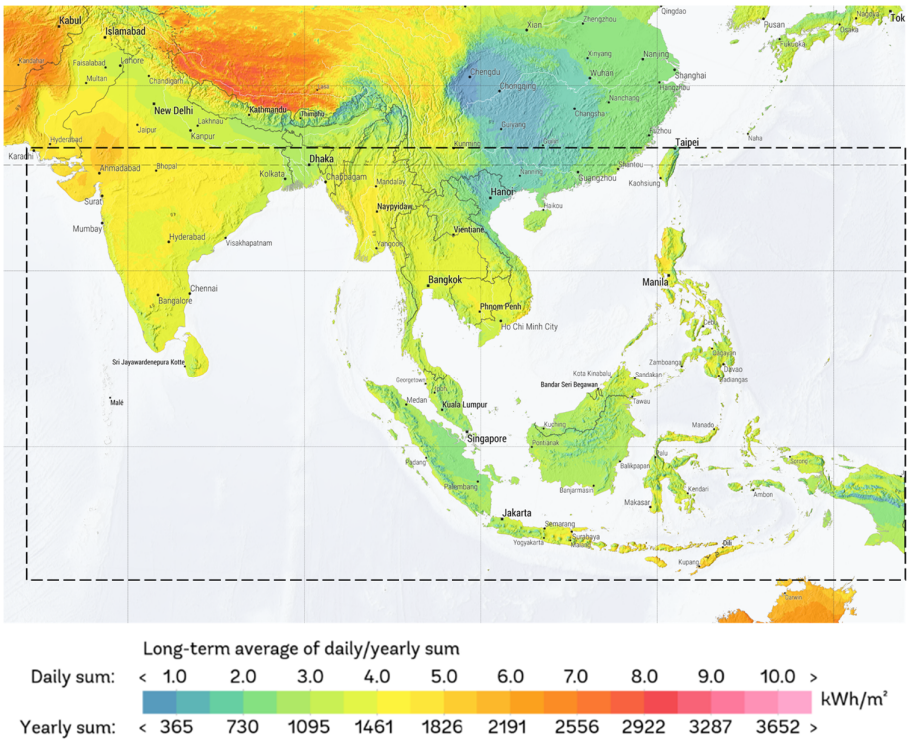

Fig. 1.2 Direct normal irradiation [11]

Absorption chillers that use solar energy as heat input, together with the related technology of the absorption heat pumps (heat transformers) driven by industrial waste heat [16] [17], have been described as one of the promising cooling systems that could meet all the requirements needed to solve the energy and environmental issues [18]. The excellence of this system is its high performance, low-temperature heat input, low operational costs, and environmentally friendly working fluids. Therefore, in several countries, many types of solar cooling systems, with single or double-effect absorption chiller systems, have been investigated in order to understand their characteristics and performance [19–27].

Single-effect absorption chillers have been extensively used since the 1960s, and in 1980s, the double-effect was developed [28]. Subsequently, multiple-effect configurations have been developed to overcome the performance limitation imposed by the single-effect type, and accordingly, have elicited higher coefficient of performance (COP) values [29]. Conventionally, absorption chillers are driven by heat from gas flaring, waste heat from engines, and other sources. Since the input heat needed for the single-effect absorption cycle is not required to have a high-temperature level, a system was conceived for the use of heat from solar energy [30].

A solar cooling system with single-effect absorption chiller can use low-temperature input around 70–100 °C [31–34]; thus, any solar collectors (flat plate collector, evacuated tube collector, compound parabolic collector, parabolic through collector) can be applied to this system to generate hot water [35]. From previous literature results (experiment and simulation) [36–38], it can be confirmed that the design COP of the solar cooling system with single-effect absorption chiller is around 0.6–0.76. The operation performance of this system is considerably affected by the weather conditions.

Many direct-fired double-effect absorption chillers driven by gas have been installed [39, 40] since the advantage of this system does not only have a high performance compared to the single-effect type but also that the gas resource itself is commonly available. Therefore, the gas demand for absorption system can usually be fulfilled even though the use of this technology increases. Additionally, in several countries the gas price per calorific value is relatively low, so using this system can reduce the operational cost. From the environmental point of view, gas is friendlier than other fossil fuels [41, 42].

The performance of a double-effect absorption chiller overcomes the performance limitation of a single-effect, but the first system needs a higher input temperature level than the single-effect absorption chiller. On the one hand, a solar cooling system featuring a double-effect absorption cycle requires a special solar collector that can provide hot water to 110–150 °C [39–41, 43–45]. On the other hand, the double-effect absorption chiller can be operated by utilising heat input from gas combustion along with the solar-driven single-effect absorption chiller. Furthermore, this feature is beneficial to assist the operation performance and guarantee continuous operation when the weather fluctuates.

The investigation results of Drosou et al. (2016) [20] showed that solar cooling system with single- or double-effects could cope with the cooling loads of the building depends on the suitability of the solar collectors. Probably, the initial cost of solar cooling systems is much higher than the conventional vapour compressor, but this can be compensated by a lower operational cost [21], provided that the system performance is properly controlled.

A single-double-effect absorption chiller combines the single and double-effect systems to take advantage of the merits of both these individual configurations. In the combined system, there are two possibilities of combination, first combining two systems, but working separately and second, combining two systems in one unit. Combining systems in one unit has several advantages, such as compact dimension, back-up/second system has a quick response, easy to synchronize both systems. Therefore, in this study, the author presents the best-combined system based on the criteria of high utilisation of waste heat or solar energy and low primary energy consumption. However, this configuration could be associated with other operability issues, particularly, the operation strategy of this system becomes more complex.

Based on the author’s experience, there is little academic research investigating the operation strategy of the single-double-effect absorption chiller. In particular, the proper selection of the operation points in terms of internal parameters under the effect of varying external conditions, is

very rare. Thus, this study firstly introduces the current operational strategy selected according to the technical experience from a maker, where solution flow rates and gas flow rate are controlled in the single-double-effect absorption chiller. Field test of the operative system are gathered and analysed. Even though the performance of the single-double-effect absorption chiller is high, when considering the complexity of the configuration and the annual performance factor (APF) of this system, the possibility of further enhancement of the performance of this system to minimise its primary energy consumption is explored. Finally, a performance maximisation method based on the proper adjustment of internal parameters is developed and an applicable operation strategy able to approach the maximal efficiency is suggested.

1.2 Research Objective

The aim of combining the single-effect and double-effect absorption chiller systems in one system for solar cooling application is to eliminate the drawback of each system and to improve the whole system performance. However, this makes the configuration of the combined system more complex than the conventional absorption chiller. Referring to the initial design, this system is able to achieve higher performance. But in the real condition, especially for the annual operation, this system might operate differently from the initial design, thus, the result performance of this system is even further from the optimum COP. This specific problem lowers the annual performance factor (APF) of the system. Therefore, in this situation, it is not enough just considering the initial design of the combined systems, but also an optimal operation of the system. This can maximise the APF of the system.

A new system configuration of a single-double-effect absorption chiller for solar-cooling applications is under analysis. The characteristics and performance of this system are interesting to be investigated for the academic field. This study presents one of the latest progress in the solar-cooling field and clarifies the behaviour of a complex system with reference to the influence of internal parameters. A newly developed performance maximisation method is suggested. The operation performance of this system can be improved by manipulating the absorber outlet solution flow rate and the solution distribution ratio, achieving a significant reduction of the primary energy consumption, without any additional cost. Furthermore, for this advanced system configuration in various operation conditions, an optimal operation strategy is suggested to minimise the primary energy consumption.

1.3 Thesis Structure

To embody the main objective of this research, the dissertation discusses three main studies. First the basic performance and characteristics, second operation performance enhancement, and third suggested operation strategy for the single-double-effect absorption chiller. Each study has their own support to bring this study to achieve the main goal. In addition, the current operation strategy and the typical field test in Asian tropical climates are showed. All parts are discussed in the single chapters listed as follows:

Chapter 1 introduces the general background and the main purpose of this study.

Chapter 2 describes the solar cooling system in Indonesia which uses the single-double-effect absorption chiller under analysis. The description includes the detail information of each water flow loop and all single components. Specifically, the detailed description of the single-double-effect absorption chiller, such as working mode and solution/refrigerant cycle are explained.

Chapter 3 shows the current operation strategy of the solar cooling system in general and specifically, the single-double-effect absorption chiller.

Chapter 4 explains the mathematical model of the single-double-effect absorption chiller for steady and dynamic conditions. A new resistance method to calculate the overall heat transfer of heat exchanger are newly introduced in this section.

Chapter 5 discusses specifically the characteristics and the performance of the single-double-effect absorption chiller when it is influenced by the variations of hot water inlet temperature from solar energy and cooling water inlet temperature. The simulation results present the COP of the single-double-effect cycle, gas reduction ratio, and the energy input percentage.

Chapter 6 presents the operation performance enhancement of the single-double-effect absorption chiller by considering the internal parameters. Therefore, in this study, the appropriate combinations of the solution mass flow rate of the outlet absorber and the solution distribution ratio are investigated to enhance the operation performance with respect to the field tests, thus, achieving a significant reduction of the gas usage without any additional cost.

Chapter 7 suggests the applicable operation strategy that can be used for various operation conditions. Therefore, in this chapter, several possibilities operation strategys are compared to find the appropriate operation strategy for the single-double-effect absorption chiller.

Chapter 8 presents the summary and the conclusion of the dissertation and suggests the optimal operation strategy for this system to minimise the primary energy consumption.

Chapter 2
System Description

The solar cooling system using the single-double-effect absorption chiller under analysis was installed in Indonesia at the end of 2013 as a field test (Fig. 2.1) to assess its performance and characteristics in Asiatic tropical regions. This system was chosen because of its large capacity and ability to utilise solar energy, even though the area of the solar collectors is limited. The main feature of this absorption cooling system is a special temperature generator used as the component that is directly heated by solar energy, whereby additional water vapour is desorbed and subsequently condensed in the special condenser. This system also exhibits a different flow direction for the cooling water than usual configurations, whereby the water flows from the condensers to the absorber to maximise the utilisation of solar energy. Basically, this system was designed to maximise the use of solar energy despite the possible limitation of the solar collectors. During a partial-load operation, this absorption chiller system can work either as a single-effect or as a double-effect or as a single-double–effect system. Since no previous study is available about this system in tropical Asia regions, this work is presented to analyse its performance and characteristics, and eventually maximise its performance and suggest an advanced operation strategy.

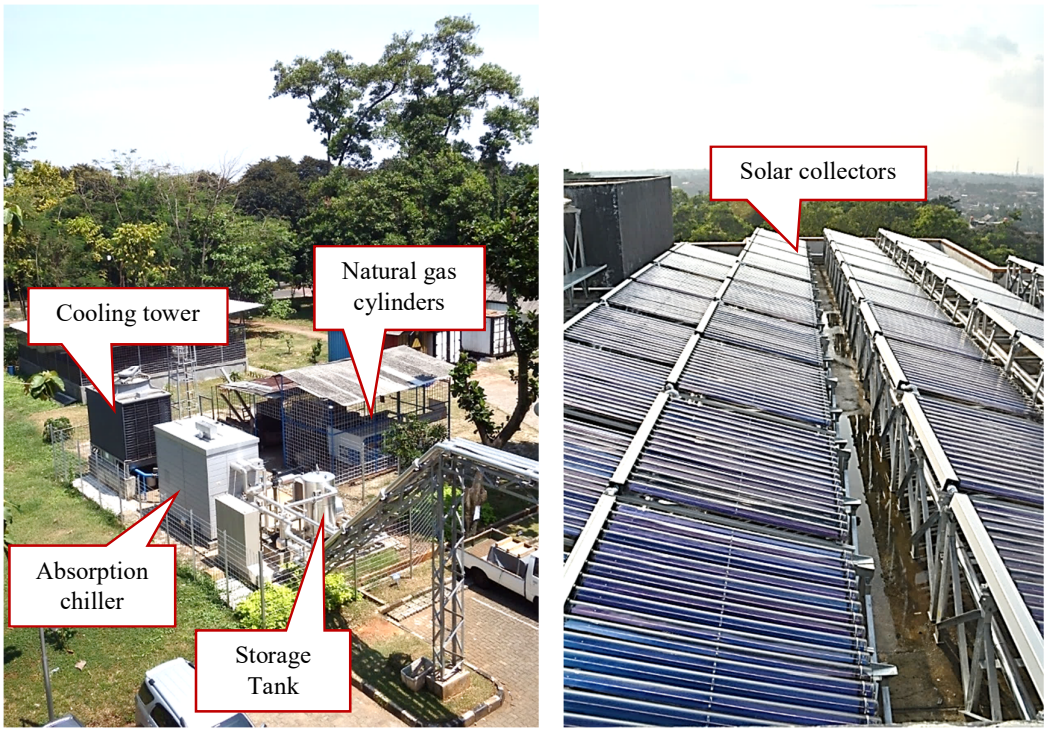

Fig. 2.1 Field test machine in Indonesia (the University of Indonesia)

2.1 Solar cooling system description (System circuits and components)

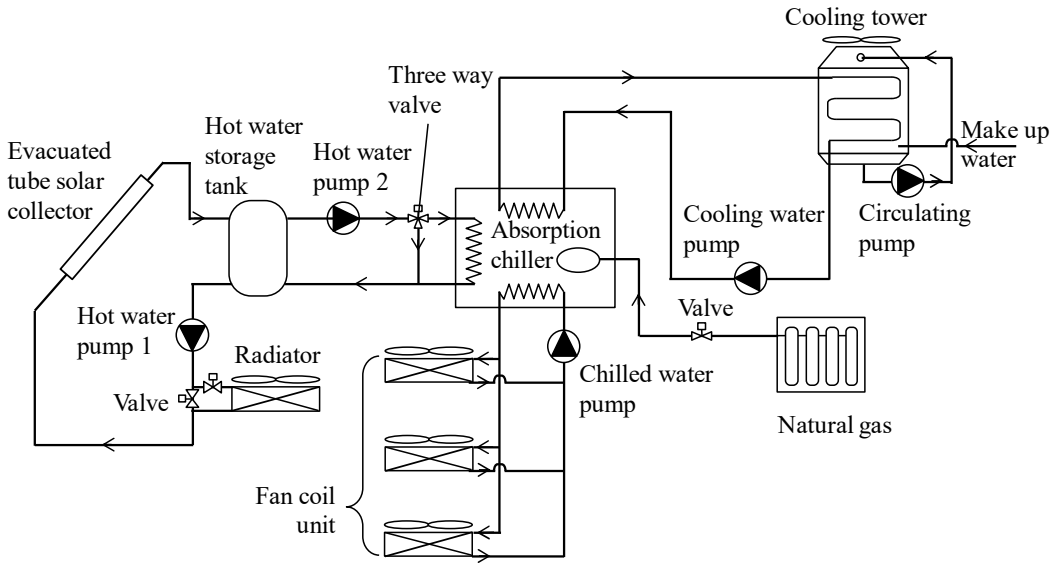

Fig. 2.2 Schematic diagram of the solar cooling system

The solar cooling system using the single-double-effect absorption chiller (Fig. 2.2) supplies chilled water to the mechanical research centre (MRC) building. The building includes laboratories, meeting rooms, and lecturer rooms. The official active hours of the building are between 8:00 until 16:00. Evacuated tube solar collectors, located on the roof top of the MRC building, are used to absorb solar energy. A hot water storage tank is used to maintain the temperature of the hot water stable for driving the absorption chiller. When the temperature of the hot water from the solar collector is above the maximum temperature limit, the radiator releases the heat to the environment in order to maintain the hot water inside the solar collectors in the liquid phase, thereby maintaining safe operational pressure ranges. The chilled water is distributed in parallel to a fan coil unit (FCU) in each floor. The nominal cooling capacity of the single-double-effect absorption chiller machine is 239 kW. The system uses a cooling tower to reject the heat from the condensers and the absorber. For the gas heat source, the compressed natural gas (CNG) is stored in high-pressure cylinders.

As for initial cost (consisting of main equipment, electrical work, civil work, and general installation) and maintenance cost of the system, the highest voice is associated to the main equipment, namely the absorption machine itself, then followed by electrical work and civil work. Lastly, the maintenance cost over one year of operability constitutes approximately 3% of the total cost of the system.

For more information about the investment, the initial cost of the solar cooling system installed at the University of Indonesia is explained and compared with other solar cooling systems by using a different type of solar thermal collector. All the conditions and the calculation method to predict the total initial cost for a solar cooling system that supplies 10 kWh cooling on

daylight with the solar radiation of 7.6 kWh/m^{2}day can be seen in IIR Information 34th Note [46]. The information of other cooling systems such as price (euro/kW of cooling), daily efficiency and price of all collectors (flat plate collector (PTC), evacuated tubular collector (ETC), and parabolic trough collector (PTC)), and COP are referred to IIR Information 34th Note [46]. While this study's solar cooling system information about the price per kW of cooling, the COP and the hot water inlet temperature is obtained directly from the pilot project installed in the University of Indonesia. There are two type of prices, the first price is 479 euro/kW of cooling (only the absorption machine (M)) and the second is 710 euro/kW of cooling (the machine with other main equipment (ME)), and the COP of this system when only use solar energy (the hot water inlet temperature is 90 °C) is 0.8.

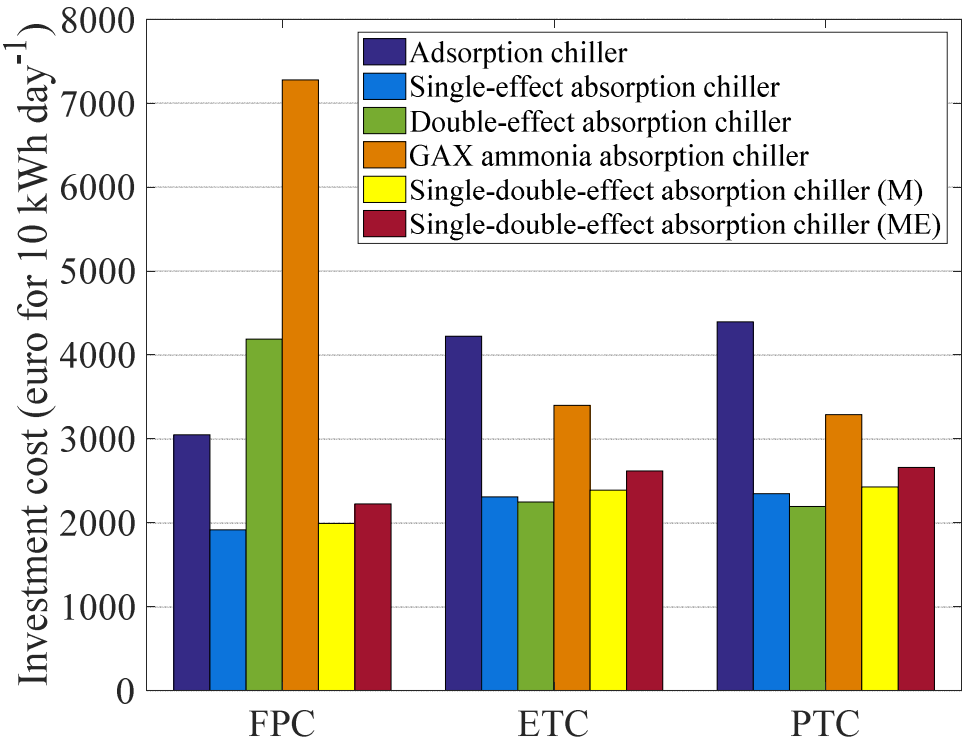

Fig. 2.3 Investment cost of the solar cooling systems with a different type of solar thermal collectors for supplying 10 kWh of cooling

According to Fig. 2.3, the type of solar thermal collector greatly influences the investment cost of the solar cooling systems using adsorption chiller, double-effect absorption chiller, and GAX ammonia absorption chiller, but not for the single-effect and the single-double-effect absorption chiller. The proper combination between the solar collector and the sorption machine can lower the initial cost. Even though this study's solar cooling system with FPC has the lowest initial cost compared to ETC and PTC, but for the field test, this system used ETC because the daily efficiency of this collector is high that is able to reduce the aperture area of the collector.

From Fig. 2.3 can be observed that the investment of this solar cooling system not as expensive as GAX ammonia absorption chiller and adsorption chiller. The investment cost of the single-double-effect absorption chiller with ETC to produce 1 kW of cooling is 2,388.07 euro, and by adding other main equipment such as cooling tower, fan coil units, pumps and storage tank becomes 2,619.07 euro.

2.1.1 Evacuated tube solar collector

Sixty-two modules of evacuator tubular collectors were installed (Fig. 2.4), which combined two modules in series as one unit that consisted of 32 tubes, and they were divided into eight main parallel rows (Fig. 2.4(b)) with each tube in a single module being connected to a manifold. The total aperture area of the evacuated tube solar collectors installed at the roof top of the MRC building is 181.04 m^2. Evacuated tube solar collector is used in this system to provide hot water temperature up to 90 °C. The specification of the individual evacuated tube solar collector can be seen in Table 2.1.

Table 2.1 the specification of the evacuated tube solar collector (DMG100-16 Sunrain)

Parameter	**Unit**	**Value**
Aperture area	m^2	2.92
Number of absorber tubes	-	16
Conversion factor	-	0.754
Heat transfer coefficient a_1	W/m^2K	1.405
Temperature depending heat transfer coefficient a_2	W/m^2K	0.005
Volume flow rate	l/m^2h	73

(a). Original picture

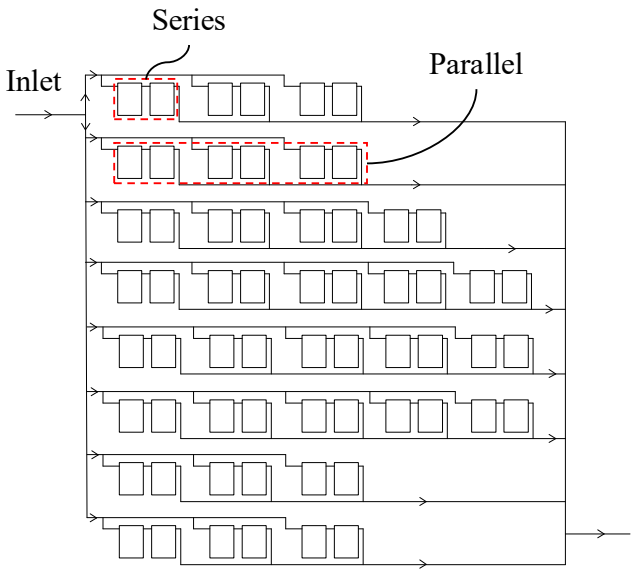

(b). Schematic diagram

Fig. 2.4 Evacuated tube solar collector

2.1.2 Hot water storage tank

This solar cooling system has no backup electric heater in the hot water circuit. But this system has a hot water storage tank with a volume of 1000 L (Fig. 2.5) to keep the hot water temperature supply to the absorption chiller is stable. Therefore, the change of solar radiation will not directly influence the hot water temperature to the absorption machine. The hot water from the evacuated tube solar collector field to the hot water storage tank is circulated by a vertical multistage in line pump.

Fig. 2.5 Hot water storage tank

2.1.3 Single-double-effect absorption chiller machine

This absorption chiller machine (Fig. 2.6) can work as a single-effect mode, a double-effect mode, or a single-double-effect mode. Each mode is depended on the utilisation of solar energy and the amount of cooling load from the MRC building. The specifications of this absorption chiller system are shown in Table 2.2.

Fig. 2.6 Single-double-effect absorption chiller machine (Kawasaki Thermal Engineering)

Table 2.2 operation condition of absorption chiller machine

Parameter	Unit	Value
Chilled water inlet temperature	°C	15
Chilled water outlet temperature	°C	7
Chilled water flow rate	m^3/h	26
Cooling water inlet temperature	°C	32
Cooling water flow rate	m^3/h	68
Hot water inlet temperature	°C	75–90
Hot water flow rate	m^3/h	7.8
Cooling capacity	kW	239

2.1.4 Cooling tower

An evaporative cooling water type is used in this solar cooling system (Fig. 2.7). The cooling water circuit of this system is a close system. The spray water is used at the outside of the cooling water tube to absorb the heat from the cooling water inside the tube; the heat absorbed by the spray water is released to the environment by the fan. Thus, this cooling tower needs makeup water. The cooling water is continuously circulated by the centrifugal end suction pump. The specifications of the cooling tower are listed in Table 2.3.

The effectiveness of the cooling tower can decrease because of the influence of micro-organism such as bacteria, fungi, and algae to the spray water. Therefore, in order to minimise the growing of micro-organism in the spray water, then chemical is put in the spray water storage.

Fig. 2.7 Cooling tower

Table 2.3 the specification of cooling tower

Parameter	Unit	Value
Hot water temperature	°C	37.6
Cold water temperature	°C	30
Wet bulb temperature	°C	28
Volume flow rate	m^3/h	80
Capacity	kW	520.9
Range	-	7.6
Motor fan	kW	7.5

2.1.5 Fan coil unit (FCU)

The chilled water is circulated from the chiller machine to the MRC building by distributing the chilled water to each floor. Each floor has three fan coil units (one unit of 8.79 kW or 30,000 BTU/h FCU and two units of 11.72 kW or 40,000 BTU/h FCU, Fig. 2.8) to take the heat from the room. All the chilled water is distributed and returned in parallel at each room and each floor. The chilled water is circulated by a centrifugal pump.

Table 2.4 the specification of FCU Aicool FD 32 and FD 42 (Fan type – direct driven)

Parameter	**Unit**	**Value**
Cooling capacity	kW	8.79 (FD 32) and 11.72 (FD 42)
Area	m^2	16.5
Air flow rate	m^3/h	1,867
Air inlet temperature	°C	26.6
Humidity	%	55
Chilled water temperature	°C	7.2

Fig. 2.8 Fan coil unit

2.1.6 Radiator

A radiator (Fig. 2.9) is used to release the over heat from the hot water to environment. This equipment works when the hot water collector outlet temperature is over than the allowed maximum hot water temperature (95 °C). The cooling capacity of this radiator is 442.8 kW.

Fig. 2.9 Radiator

2.1.7 Compressed natural gas (CNG)

Compressed natural gas is stored in 35 high-pressure cylinders (Fig. 2.10) with a total capacity of 450 m^3 (being the lower heating value of gas 38.36 MJ/m^3, 450 m^3 gas equals to a heating capacity of 17,262 MJ). CNG cylinders are used in absence of gas pipe lines.

Fig. 2.10 CNG cylinder

2.2 Data acquisition and instrumentation

During the field tests, the data logger records the measurement of temperatures, flow rates, and solar radiation at 1 s time step intervals. For the temperature measurement of the refrigerant, water, solution and ambient, three types of thermometer are used, namely thermistor, copper-constantan thermocouple, and resistance temperature detector (Pt100). The flow rate of the chilled water, cooling water, and hot water is measured by using an electromagnetic flow meter while the gas flow rate is measured by the gas flow meter. As known, this system uses solar energy as one of the energies input, so the solar radiation is measured by pyranometer.

Table 2.5 Measurement equipment list

Measurement equipment	**Brand/type**	**Accuracy**
Data logger		
Water flow meters	MGG11D-080P11LS1AHA-XX /MGG10C-MC3A-1B1X, Azbil	± 0.2% full scale (FS)
	MGG11D-100P11LS1AHA-XX/MGG10C-MC3A-1B1X, Azbil	± 0.2% full scale (FS)
	MGG11D-050P11LS1AHA-XX /MGG10C-MC3A-1B1X, Azbil	± 0.2% full scale (FS)
Gas flow meter	CMG250N030100000, Azbil	± 3% full scale (FS)
Temperature sensors	Thermistor	± 0.3 °C
	Copper-constantan thermocouple	± 0.5 °C
	Resistance temperature detector (Pt100), class A	± 0.1 °C
Solar radiation sensors	LP02, Hukseflux thermal sensors	± 5% (expected)

Fig. 2.11 shows all the measurement points at the solar cooling system and the single-double-effect absorption chiller. By measuring some temperatures points in Fig. 2.11, the Dühring diagram and the performance of this absorption chiller can be known and analysed. The information of brand/type and accuracy of each sensor is summarised in Table 2.5. Table 2.6 gives the enlargement of each symbol in Fig. 2.11 and the sensor of the measurement points.

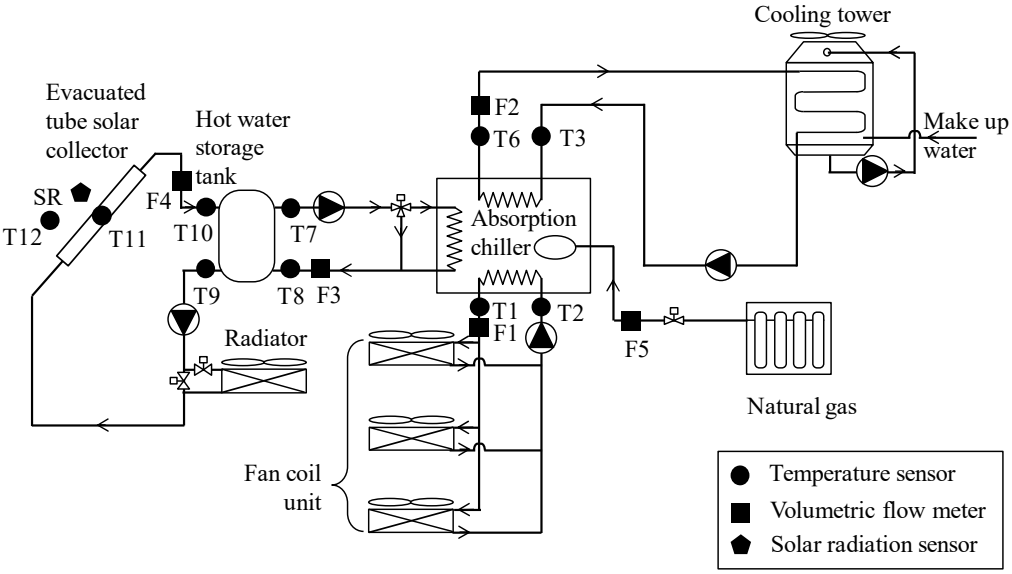

(a). The solar cooling system

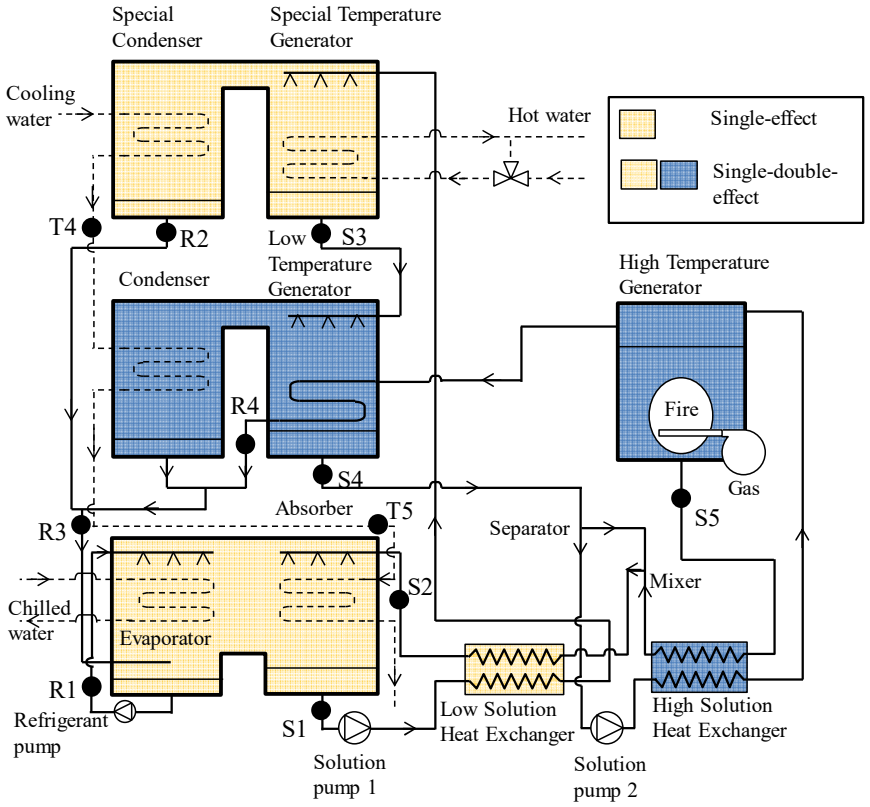

(b). The single-double-effect absorption chiller

Fig. 2.11 Measurement points

Table 2.6 Measurement points

Measurement point	Name	Measurement equipment
T1	Chilled water inlet temperature	Thermistor
T2	Chilled water outlet temperature	Thermistor
T3	Cooling water inlet temperature of the special condenser	Thermistor
T4	Cooling water inlet temperature of the condenser	Copper-constantan thermocouple
T5	Cooling water inlet temperature of the absorber	Copper-constantan thermocouple
T6	Cooling water outlet temperature of the absorber	Thermistor
T7	Hot water chiller inlet temperature	Thermistor
T8	Hot water chiller outlet temperature	Thermistor
T9	Hot water collector inlet temperature	Thermistor
T10	Hot water collector outlet temperature	Resistance temperature detector
T11	Hot water inside collector temperature	Resistance temperature detector
T12	Ambient temperature	Resistance temperature detector
S1	Solution outlet temperature of the absorber	Thermistor
S2	Solution inlet temperature of the absorber	Thermistor
S3	Solution outlet temperature of the special temperature generator	Copper-constantan thermocouple
S4	Solution outlet temperature of the low temperature generator	Copper-constantan thermocouple
S5	Solution outlet temperature of the high temperature generator	Thermistor
R1	Refrigerant outlet temperature of the evaporator	Thermistor
R2	Refrigerant outlet temperature of the special condenser	Thermistor
R3	Refrigerant outlet temperature of the condenser	Thermistor
R4	Refrigerant outlet temperature of the high temperature generator	Thermistor
F1	Chilled water flow rate	Electromagnetic flow meter
F2	Cooling water flow rate	Electromagnetic flow meter
F3	Hot water flow rate of pump 2	Electromagnetic flow meter
F4	Hot water flow rate of pump 1	Electromagnetic flow meter
F5	Gas flow rate	Gas flow meter
SR	Solar radiation	Solar radiation sensor

2.3. Steady-state experiment

The single-double-effect absorption chiller was tested according to the full load design condition before this absorption chiller is installed for the field test. In order to have the same input condition with the design condition, all the inlet temperature of chilled water, cooling water, and hot water are conditioned by the circulating thermal bath. The experimental data at full load (239 kW) is shown in Table 2.7.

Table 2.7 Steady-state experimental data at full load (239 kW)

Measurement	Value	Unit
T1	15.1	°C
T2	7.1	°C
T3	31.9	°C
T4	33.1	°C
T5	34.1	°C
T6	37.6	°C
T7	90	°C
T8	79.4	°C
S1	37.4	°C
S3	76.6	°C
S4	78.7	°C
S5	137.4	°C
S2	42.3	°C
R4	81.3	°C
R2	35.2	°C
R3	35.5	°C

2.4 System description of single-double-effect absorption chiller

This study focuses on the single-double-effect absorption chiller because this system is the main component of the solar cooling system installation. Therefore, more detailed descriptions about the single-double-effect absorption chiller are given in this chapter.

2.4.1 Previous study of single-double-effect absorption chiller

There are several possible configurations of single-double-effect absorption chillers (Figs. 2.12, 2.13, and 2.14), and each one has its main advantages. In the below-mentioned studies, all these systems use dual energy sources in the specific combination dependent on the application case (solar energy, waste heat, or gas (direct-fired/steam)).

Assuming that the temperature and flow rate of the hot water and steam are the same for all cycles, Figs. 2.12(c), 2.13(c), and 2.14(c) show how the utilisation of solar energy/waste heat and its primary energy consumption are affected by the solution flow path. The cycle of S. Kimijima et al. (1998) [47] distributes the solution from the absorber to the special temperature generator (STG) driven by waste heat, and to the high-temperature generator (HTG) driven by steam. This

means that the amount of solution in the STG, driven by waste heat or solar, is not completely circulated, and thus, this condition cannot fully utilise the heat source from solar energy. However, a smaller amount of solution is delivered to the HTG, driven by gas, which can reduce the gas consumption because of the high latent heat. The cycle of K. Saito et al. (1994) [48] features a serial solution flow rate of the STG, driven by hot water, and the high-temperature generator driven by steam. All the solution firstly goes to the STG, which can fully utilise the waste heat. Successively, the entire solution flow rate is delivered to the HTG, bringing along the requirements for a large quantity of sensible heat, thus leading to high primary energy consumption. The system constructed for this study circulates the entire solution amount to the STG, driven by hot water heated from solar energy, and distributes part of the solution amount to the HTG driven by gas, Fig. 2.14. This configuration strategy is chosen because it can fully utilise the solar energy and reduce gas consumption.

Table 2.8 summarises the benefits of the system configuration discussed in this study when compared to the system configurations of prior studies, Figs. 2.12, 2.13 and 2.14.

Table 2.8 Single-double-effect absorption chiller comparison

	S. Kimijima et al. cycle	K. Saito et al. cycle	This study cycle
Number of solution pumps	1	2	2
Waste heat/solar energy utilisation	low (small solution mass flow rate because of the distribution ratio)	high (full solution mass flow rate and weak concentration)	high (full solution mass flow rate and weak concentration)
Gas utilisation	low (can be controlled by the distribution ratio, low flow rate, and small sensible heat)	high (full solution mass flow rate, high flow rate, and high sensible heat)	Low (can be controlled by distribution ratio, low flow rate, and small sensible heat)
Cooling water flow path	Absorber → condenser	Absorber → condenser	Condenser → absorber

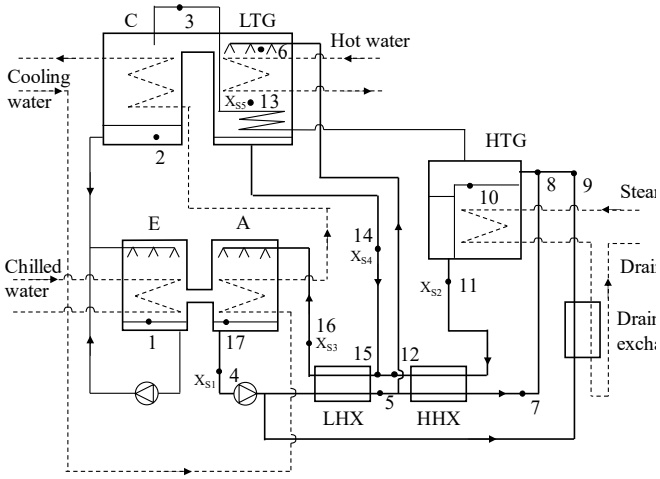

(a) Schematic diagram

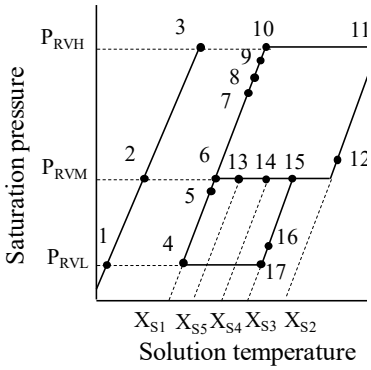

(b) Dühring diagram

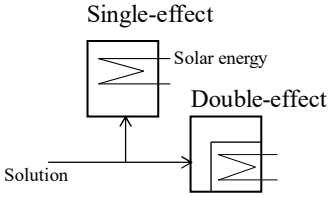

(c) Parallel type of solution flow path

Fig. 2.12 Parallel type single-double-effect absorption chiller of S. Kimijima et al. (1998) [47] cycle.

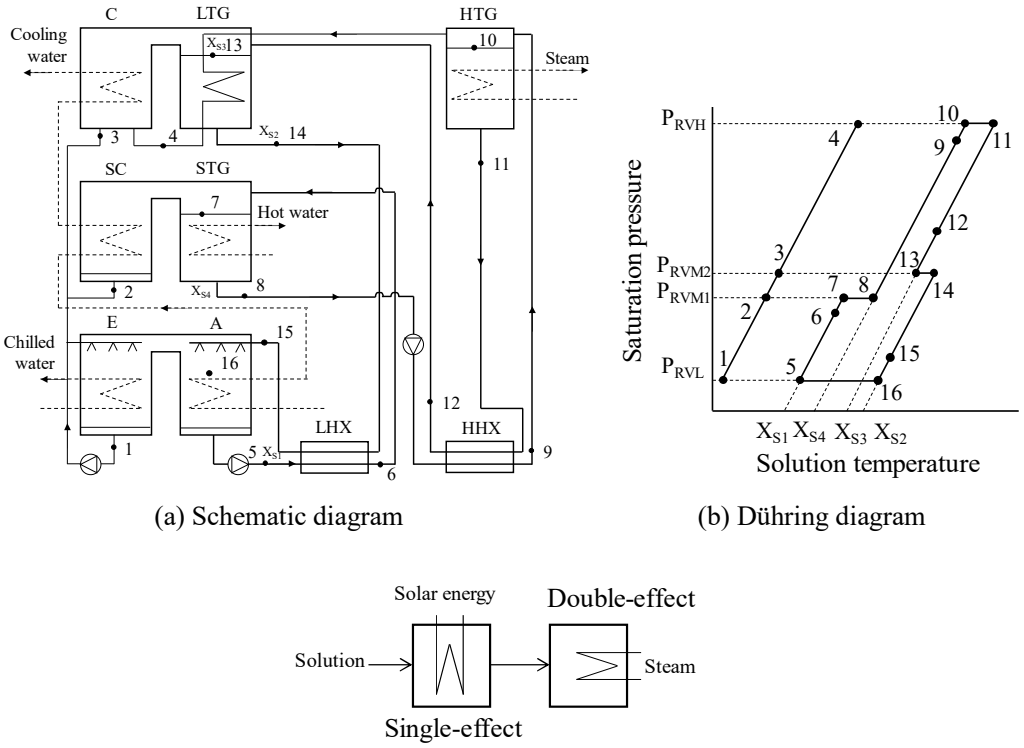

(a) Schematic diagram

(b) Dühring diagram

(c) Series type of solution flow path

Fig. 2.13 Series type single-double-effect absorption chiller of K. Saito et al. (1994) [48] cycle.

2.4.2 New configuration of single-double-effect absorption chiller

The system presented in Fig. 2.14 can work as a single-effect mode, a double-effect mode, or a single-double-effect mode (combination of single and double-effect). The single-effect mode of this system was designed to supply 50% of the maximum cooling load, whereas the double-effect cycle assists for the remaining cooling load. Therefore, 50% to 100% of the total design value can be provided. All the working modes depend on the instantaneous availability of solar energy and the required cooling load. When solar energy is sufficient for the system to provide the necessary cooling capacity, then the system works with a single-effect cycle. The single-effect mode is later adjusted to the single-double-effect mode when the total cooling capacity increases and solar energy is insufficient to provide the full cooling capacity. The double-effect mode is only used when solar energy cannot be utilised. The primary focus of this study is to investigate the characteristics of a system under a single-double-effect mode.

The working principle of the single-double-effect absorption chiller is the same as the conventional single and double-effect absorption chillers. However, a single-double-effect system has two additional components and, in this case, a different cooling water flow path, which starts from the special condenser (SC), continues to the condenser (C) and ends up to the absorber (A). The single-double-effect absorption chiller under consideration consists of seven main

components: an evaporator, an absorber, a special-temperature generator, a low-temperature generator, a high-temperature generator, a special condenser, and a condenser. In the single-effect mode, only four of the components are used while five are used in the double-effect mode. When the system operates in the single-double-effect mode, all components are used. Additionally, two counter-flow solution heat exchangers are used for heat recovery, low-temperature heat exchanger (LHX) and high-temperature heat exchanger (HHX).

(a) Absorption machine

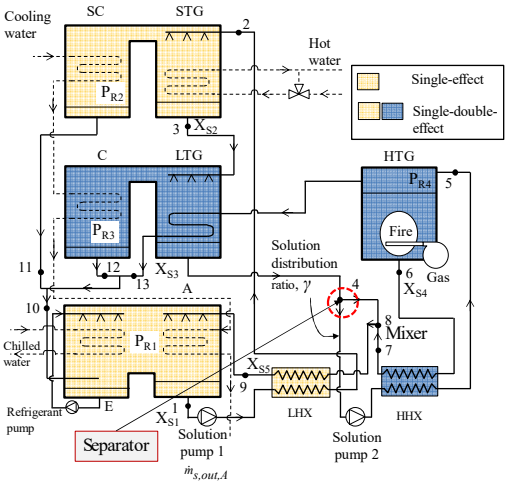

(b) Schematic diagram

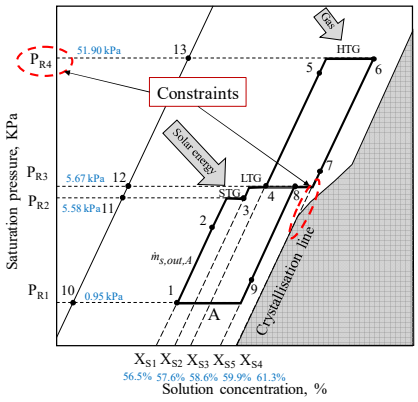

(c) Dühring diagram

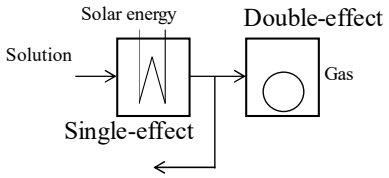

(d) Series and distribution type of solution flow path

Fig. 2.14 Series and distribution type of the single-double-effect absorption chiller.

The working pair of this system is water, as a refrigerant, and lithium bromide (LiBr) as an absorbent. This single-double-effect absorption chiller is designed to maximise the utilisation of solar energy and, at the same time, to reduce the gas consumption as much as possible. Therefore, the entire solution mass flow rate from the absorber passes through the STG to the low-temperature generator (LTG). A separator is installed after the low-temperature generator to control the amount of solution that is sent to the HTG (solution distribution ratio γ) and the mixer

by adjusting the mass flow rate circulated by the solution pump 2, Fig. 2.14(b). The gas consumption can be reduced when a smaller solution amount reaches the HTG by the separator.

Although, previous studies have shown significant savings in the primary energy consumption, in general, the largest share of energy input into the system, at full load, is allocated to the gas combustion. Accordingly, this study focuses on important internal parameters such as the mass flow rate of the solution's absorber outlet, which affects the utilisation of the heat source from solar energy, and the solution distribution ratio, which affects the reduction of the heat source from the gas. The appropriate combinations between the solution mass flow rate of the absorber outlet and the solution distribution ratio, Fig. 2.14(b), are investigated to enhance the operation performance of the system. Thus, it is shown that a large additional reduction of gas usage can be achieved without any supplementary cost.

2.4.3 Solution and refrigerant cycle description

Fig. 2.14(b) shows the schematic diagram of the single-double-effect absorption chiller. This system obeys the same working principle, and also consists of the same components as those in the conventional double-effect absorption chiller. However, this system has additional, special components, namely, a special temperature generator, and a special condenser, that are used to utilise heat from solar energy for desorbing vapour and then condensing it. This system can work in a single-effect mode or in a single-double-effect mode. Actually, the single-effect mode was designed for low cooling loads, and the use of this mode is thus associated with sufficient solar energy for provision of steady cooling capacity. When the solar energy is insufficient, or the cooling load is too large for operation in the single-effect mode, or during a simultaneous occurrence of these conditions, the single-double-effect mode is used. The system then uses dual-heat sources at the same time, namely solar energy and gas. Based on the maximum value of the nominal cooling capacity of this absorption chiller, a detailed discussion follows in this study that focuses on the single-double-effect mode.

The single-double-effect absorption chiller machine consists of several main components, namely, the evaporator (EVA), absorber (ABS), special-temperature generator (STG), low-temperature generator (LTG), high-temperature generator (HTG), low-temperature heat exchanger (LTHex), high-temperature heat exchanger (HTHex), special condenser (SCOND), condenser (COND), expansion valves, and solution pumps. The internal state numbers that characterise the thermodynamic properties of lithium bromide-water solution (no. 1–9) and refrigerant/water vapour (no. 10–14), are shown in Fig. 2.14(b) and Fig. 2.14(c).

The hot water from the solar panels enters the STG. Inside the STG, the heat extracted from the solar energy supports the desorption process of the water vapour from the solution, increasing its concentration. The water vapour then enters the SCOND where the heat is released for its condensation. To deliver the refrigerant at low pressure, the latter is expanded through the expansion valve. Once expanded, the two-phase refrigerant (no. 11) is mixed with the mixed refrigerant (nos. 12 and 13) from COND and LTG. The refrigerant (no. 10) is then expanded again to the lowest pressure level before entering the evaporator. Inside the EVA, the evaporation process is completed by extracting heat from the chilled water. Water vapour is then absorbed by

the solution in the absorber in order to be effectively pumped to the higher pressure levels and complete the system's cycle. In the HTG, the vapour is released from the solution receiving heat from the direct-fired gas. Similarly, the water vapour leaves the highly concentrated solution inside the LTG. The vapour generated in the HTG supports the desorption process in the LTG, partly releasing the heat of condensation. The refrigerant is then expanded and mixed with the refrigerant of SCOND and COND. The highly concentrated solution (no. 6) exits the HTG at a high temperature, and exchanges heat with the mild concentration solution inside the HTHex. Given the different pressure levels of the HTG and the LTG, the highly concentrated solution (no. 7) is expanded and mixed with the mild concentration solution (no. 8) derived from the LTG. This mixed solution is then directed to the LTHex. Inside the LTHex, the mixed solution exchanges heat with the solution derived from the ABS. The highly concentrated solution (no. 9) from the LTHex is then expanded through the expansion valve before it finally enters the ABS. Inside the ABS, the concentrated solutions absorbs water vapour from the EVA. The amount of water content increases, the concentration of the solution decreases, and the heat of absorption is extracted by means of the cooling water. The concentrated solution (no. 1) is then circulated by a pump and conveyed (no. 2) to the STG at an increased pressure. The solution (no. 3) from the STG flows towards the LTG and then through the separator. The solutions from the LTG are mixed again with a highly concentrated solution (no. 8) from HTHex, and some part of the solutions (no. 5) are directed towards the HTHex, and henceforth to HTG, which is then circulated by a pump. The pressure of this mildly concentrated solution is increased again due to the thrust of the pump. In this system, the cooling water flows from SCOND towards COND, and it is then directed to ABS. It subsequently returns to the cooling tower at a constant flow rate. The reason why the cooling water first passes from the SCOND is to maximise the amount of heat obtained from hot water (solar energy). The cooling water is also used to maintain the temperature in the absorber as low as possible.

The corresponding Duhring diagram of this system (plotted in Fig. 2.14(b)) is suitable to illustrate the thermodynamic transformations of the lithium bromide-water inside the single-double-effect cycle. Based on the Duhring diagram it can also be recognised that the system works with four different pressure levels and five solutions with different concentration values.

Chapter 3
Current operation strategy

The solar cooling system includes three water flow loop system: hot water flow loop, cooling water flow loop, and chilled water flow loop. All the water flow loops support the absorption chiller machine to create and then deliver the cooling capacity to the building. Each water flow loop is controlled according to the cooling load of the building and the weather conditions. The hot water flow loop delivers the heat input from solar energy to the absorption chiller. The cooling water flow loop absorbs the heat from the absorption chiller to the cooling tower. The chilled water flow loop extracts heat from the building to the absorption chiller. In this chapter, the current operation strategy of the absorption chiller and each water flow loop is explained.

3.1 Control operation of solar cooling system

3.1.1 Hot water flow loop

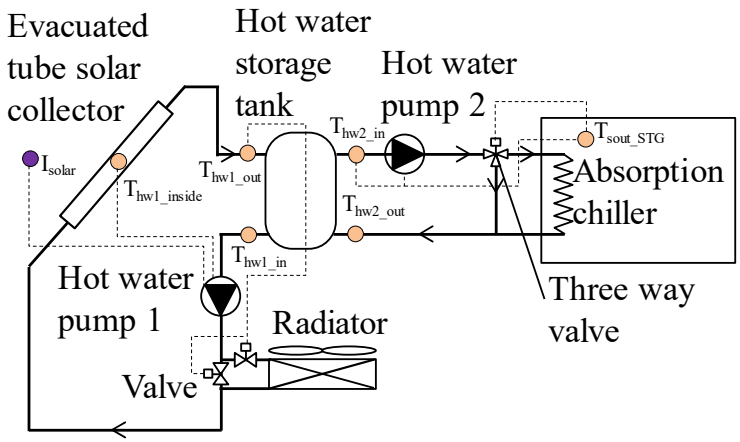

Fig. 3.1 Schematic diagram of the hot water flow loop

For the system off, the hot water in the pipe between the hot water storage tank and the evacuated tube solar collectors is circulated by hot water pump 1 (Fig. 3.1) when solar radiation is higher than 400 W/m^2 or the hot water inside collector temperature T_{hw1_inside} is 90 °C; the hot water pump 1 stops working when solar radiation is lower than 400 W/m^2, or the hot water inside collector temperature is lower than 65 °C. For the system on, hot water pump 1 works when the hot water inside collector temperature T_{hw1_inside} is 60 °C and the hot water inside collector temperature is lower than 55 °C. The hot water from the solar collectors enters the hot water storage tank. Inside the tank, the hot water from the evacuated tube solar collectors is then mixed with the hot water from the absorption chiller. The mixed hot water inside the storage tank is circulated to the absorption chiller by the hot water pump 2. The hot water inlet to the absorption

chiller can be used by the absorption chiller when the chiller hot water inlet temperature T_{hw2_in} is at least 3 K higher than the solution outlet temperature from the special temperature generator T_{sout_STG}.

The temperature difference between the chiller hot water inlet temperature and the solution outlet temperature of the special temperature generator is used to control with an on/off strategy the hot water pump 2 and the adjustment of the three-way valve. The latter closes as the hot water pump 2 stops circulating when the temperature difference is lower than 3 K. Otherwise, the hot water pump 2 circulates continuously the mixed hot water from the hot water storage tank to the absorption chiller and the three-way valve opens the flow path from the tank to the absorption chiller.

For safety operation, when the hot water collector outlet temperature is higher than 95 °C, two motorised ball valves adjust the flow path of hot water from the hot water storage tank through the radiator to release the excess heat, and then goes back to the evacuated solar collectors. The heat is directly released to the environment by the radiator even though the absorption chiller stops, but the radiator stands by in order to prevent anexcessive hot water temperature in the evacuated tube solar collector.

All the control operations of the hot water flow loop equipment are represented in Fig. 3.2. The control operation of the hot water collector pump and the radiator is not depended on the chiller system. Therefore, they continuously work even when the chiller system does not work. The hot water chiller pump and the three-way valve are depended on the operation of the chiller system; they only work when the chiller system is switched on, and they stop working when the chiller system stops.

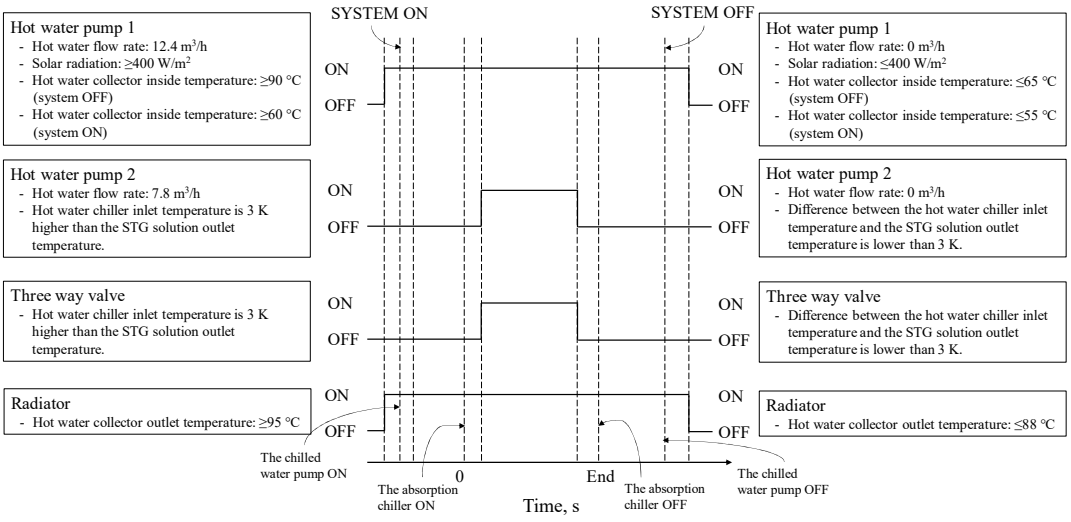

Fig. 3.2 Control operation for the hot water collector pump, the hot water chiller pump, the three-way valve, and the radiator

3.1.2 Cooling water flow loop

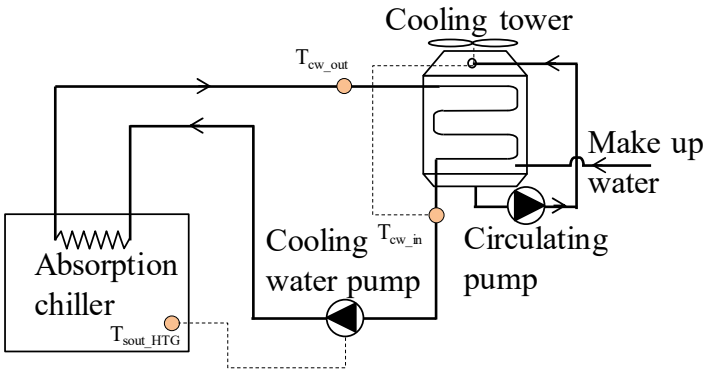

Fig. 3.3 Schematic diagram of the cooling water flow loop

In this flow loop, the cooling water pump circulates the cooling water continuously from the absorption chiller to the cooling tower (Fig. 3.3). This flow loop works to absorb the heat from the absorption chiller, and then, release it to the environment in the cooling tower. The operation of the cooling water pump depends on the absorption chiller machine.

The cooling water pump starts circulating the cooling water after the chilled water pump starts in order to avoid the rush or over current. The cooling water is not allowed to circulate before the chilled water because it can lower the refrigerant temperature, then, when the system starts the refrigerant could freeze.

The temperature of the cooling water from the cooling tower or the cooling water inlet temperature of the special condenser T_{cw_in} is maintained around 32 °C for full load operation (Fig. 3.4). In order to keep the cooling water inlet temperature at 32 °C, the cooling tower fan is set to be on when the temperature is over than 30 °C and off when the temperature is below 26 °C. The lowest allowable cooling water inlet temperature is kept at 26 °C in order to void flooding of the refrigerant storage in the evaporator because of the minimum storage capacity. After the system is switched off, the cooling water pump stops working when the solution outlet of the high temperature generator is lower than 100 °C. The make-up water is needed to replace the lost share due to the open configuration of the cooling tower.

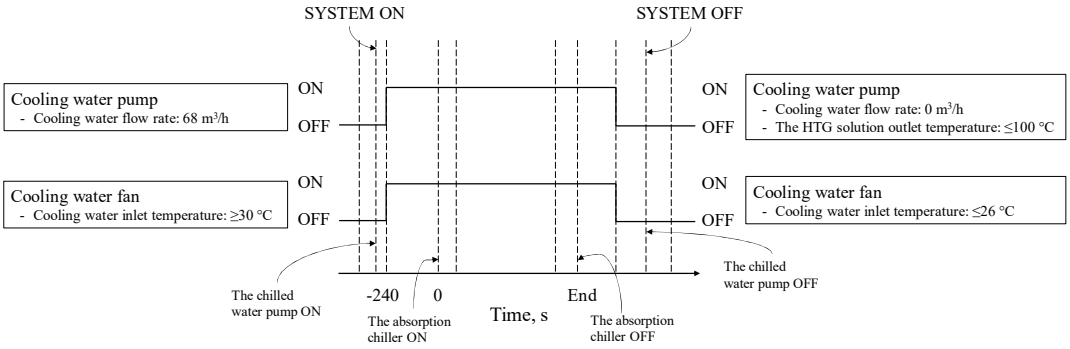

Fig. 3.4 Control operation for the cooling water pump, and the cooling tower fan

3.1.3 Chilled water flow loop

The chilled water pump circulates the chilled water from the evaporator of the absorption chiller machine to all the fan coil unit (FCU) in the MRC building. All the chilled water is distributed in parallel to the five stories building (Fig. 3.5). The chilled water temperature sent to all the FCU is kept at 7 ºC. The chilled water outlet temperature T_{chw_out} is maintained by the gas burner. To control the heat amount at the high temperature generator of the absorption chiller machine in the gas burner, the gas flow rate is adjusted by using the valve where the chilled water outlet temperature is used as the feedback. The gas burner or the gas flow rate is controlled using a PI controller. The rules of this control operation are written as follows:

1. The gas burner is automatically switched on when the chilled water outlet temperature is higher than 7.5 °C. The gas burner is automatically switched off when the chilled water outlet temperature under 6 °C.
2. The chilled water pump starts circulating the chilled water before the gas burner is switched on and the chilled water pump stops working when the absorption chiller machine stops.

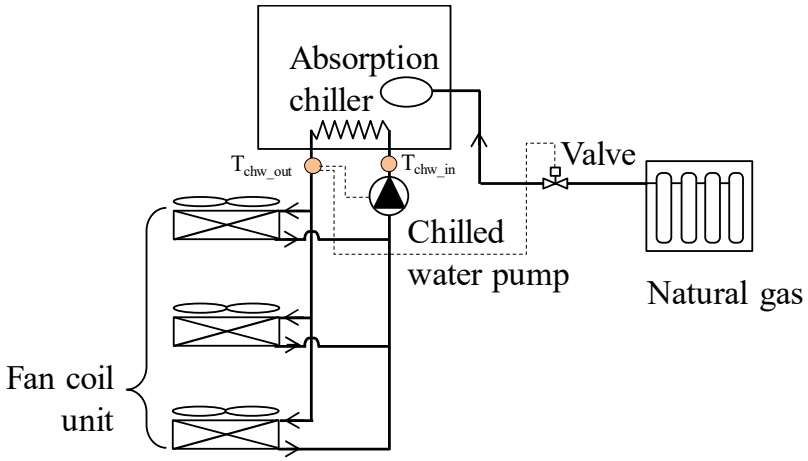

Fig. 3.5 Schematic diagram of the chilled water flow loop

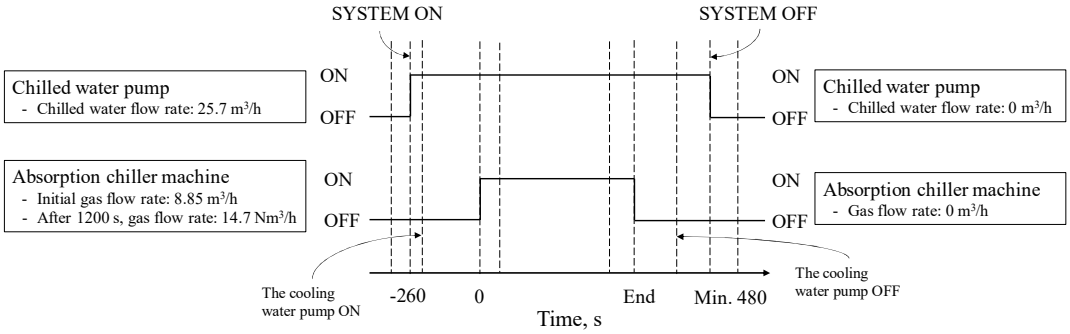

Fig. 3.6 Control operation for the absorption chiller machine and the chilled water pump

The control operation of the gas flow rate and the chilled water pump is shown in Fig. 3.6. The chilled water pump starts at the same time the absorption chiller is switched on. Then after 260 s the chilled water pump starts, the gas burner of the absorption chiller starts automatically. The gas burner maintains the chilled water outlet temperature around 7 °C. When the absorption chiller machine is switched off, the chilled water pump has to circulate around 480 s before it stops.

3.1.4 Single-double-effect absorption chiller

The current operation strategy of the single-double-effect absorption chiller is shown by Fig. 3.7. From Fig. 3.7, the rotational speed of the solution pumps are adjusted according to the cooling capacity, solution pump 1 manages the total solution flow rate of the outlet absorber and the solution pump 2 keeps the solution distribution. On the other hand, the gas burner works to keep the targeted chilled water outlet temperature by using PI controller.

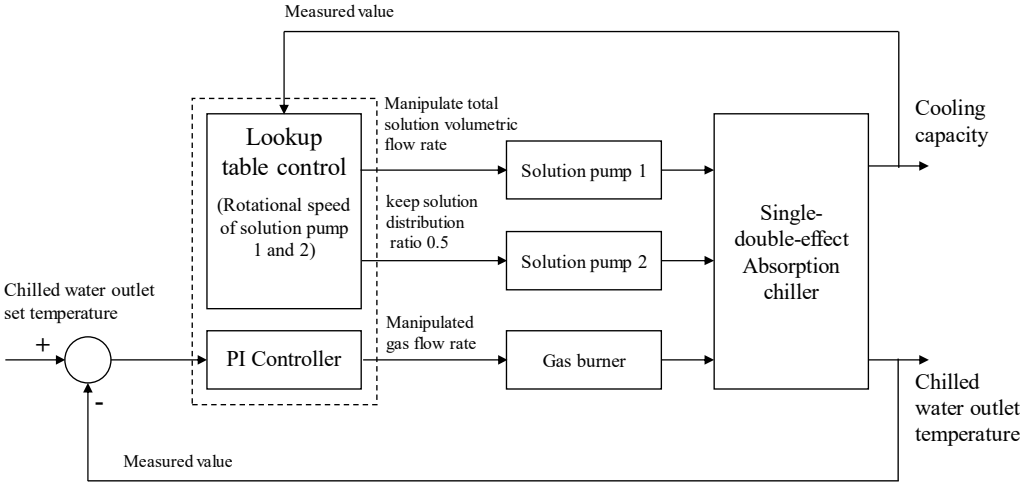

Fig. 3.7 Current operation strategy of the single-double-effect absorption chiller

3.2 Control operation results

The field test of the solar cooling system using the single-double-effect absorption chiller based on the Asian tropical climates is presented. The solar cooling system field test uses the real cooling load from the mechanical research center (MRC) building of the Universitas Indonesia. The supply hot water to the absorption chiller machine is obtained from the solar collector heated by solar radiation, while the cooling tower releases the heat from the absorption chiller machine to the real environment conditions. Therefore, the experimental data collected are affected by the real behaviour of the systems exposed to the transient external disturbances and dynamic operation strategy (Figs. 3.2, 3.4, 3.6, and 3.7).

The control operation results of the water flow loop system are shown in this chapter. The operation performance and characteristics of this solar cooling system according to the adopted control operation can be analysed on the basis of these data.

3.2.1 Control operation of hot water flow loop

Figs. 3.8–3.10 show the actual operation of the hot water collector pump on September 22nd, 2014 based on the control operation from Fig. 3.2. From Figs. 3.8, 3.9, and 3.10 it can be seen that the hot water collector pump working before the absorption chiller is operative.

From Figs. 3.9 and 3.10 it can be observed that the hot water pump 1 starts in the morning because the hot water inside collector temperature is over than 90 °C, and it circulates continuously when solar radiation is higher than 400 W/m^2; this can be seen in Fig. 3.8; but when solar radiation is lower than 400 W/m^2, the temperature of the hot water inside collector decreases gradually until the temperature is below 55 °C and this causes the hot water pump 1 to stop working (Fig. 3.9). The operation of the hot water pump 1 is strongly influenced by solar radiation compared to the hot water inside collector temperature during the operation.

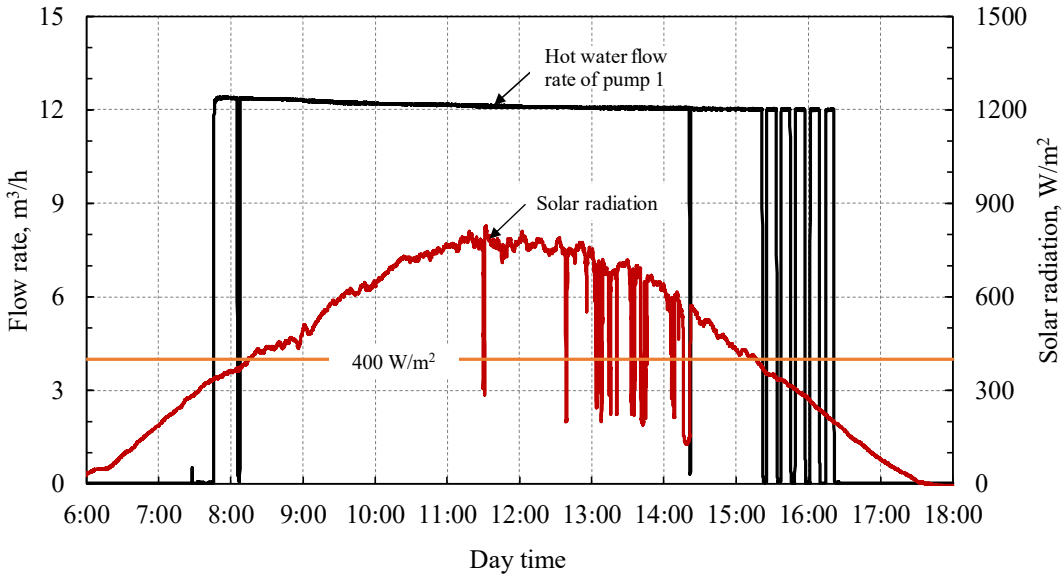

Fig. 3.8 Hot water pump 1 is controlled based on solar radiation

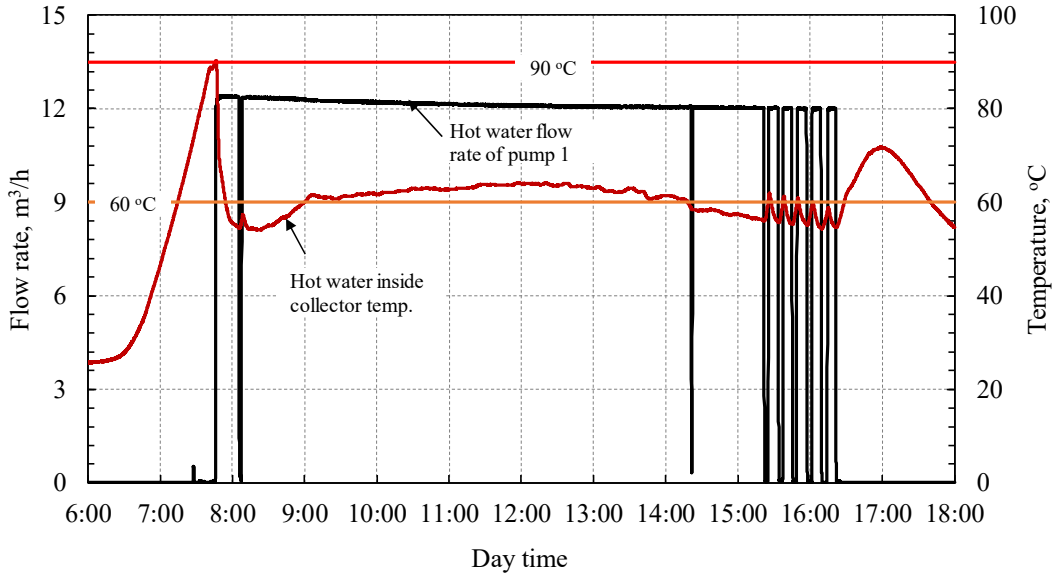

Fig. 3.9 Hot water pump 1 is controlled based on hot water inside solar collector temperature

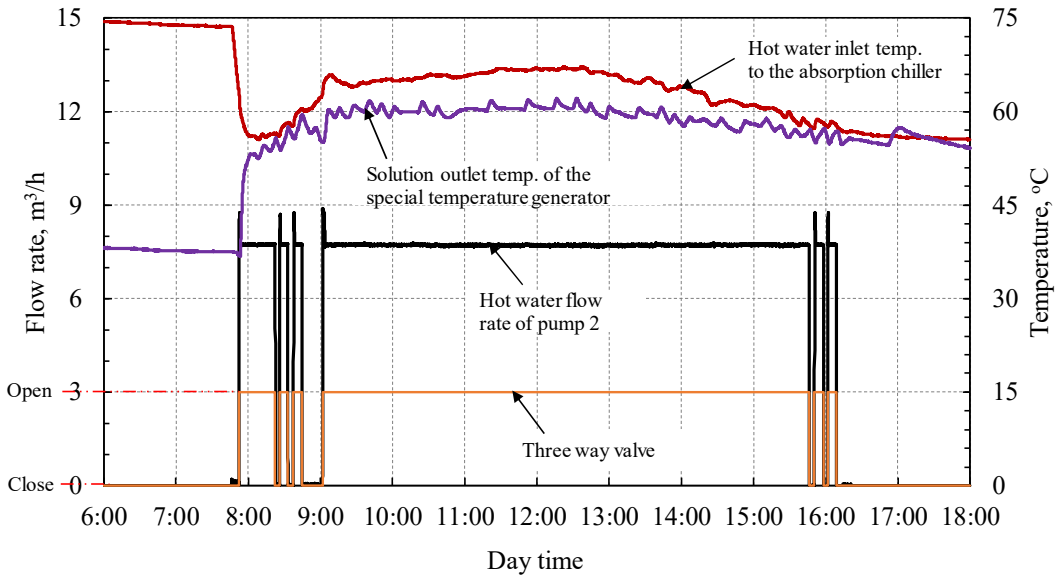

Fig. 3.10 Hot water pump 2 and three-way valve are controlled based on the temperature of the hot water inlet to the absorption chiller, the solution outlet temperature of the special temperature generator, and the vapour temperature of the high generator temperature

The functioning of the hot water pump 2 and the three-way valve based on the control operation in Fig. 3.2 can be seen in Fig. 3.10. The field results from the hot water pump 2 and the three-way valve are plotted in the same graph. Therefore, they have been placed on the same Y axis (left side). Y axis of the hot water pump 2 is flow rate, and Y axis of the three-way valve is open and close. During the operations, the operation of the hot water pump 2 and the three-way valve have the same trend: when the hot water pump 2 starts circulating the hot water the three way valve also start to open the flow rate, and when the hot water pump 2 stops, the three way valve also closes the flow rate. From Fig. 3.10 it can be highlighted that the operation of these components is closely related to the absorption chiller system.

3.2.2 Control operation of cooling water flow loop

Fig. 3.11 shows the working of the cooling water pump and the cooling tower fan based on the control operation of Fig. 3.4. The cooling water pump works continuously during the operation of the absorption chiller. The operation of the cooling tower fan can be seen in relation to the cooling water inlet temperature of the special condenser. The fan starts working when the cooling water inlet temperature is over than 30 °C, and it stops when the temperature is lower than 26 °C.

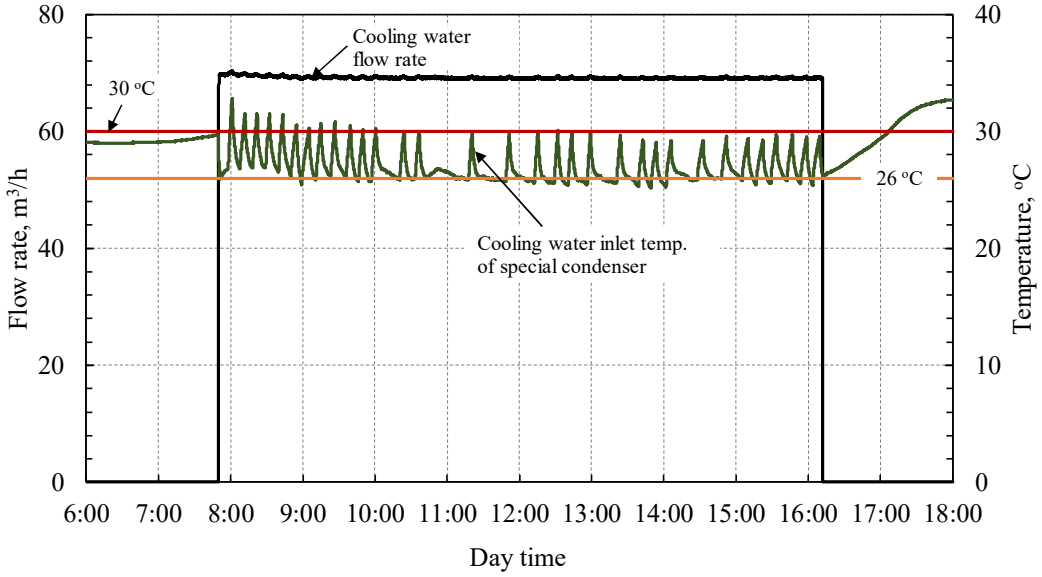

Fig. 3.11 Cooling water flow rate

3.2.3 Control operation of chilled water flow loop

The operation of a gas burner and the chilled water pump shown in Fig. 3.12 is based on the control operation in Fig. 3.6. By looking at Fig. 3.12, the control operation works properly to keep the chilled water outlet temperature in proximity of 7 °C. Based on the control operation in Fig. 3.6, the chilled water pump circulates the chilled water continuously. From the field test results,

the chilled water flow rate is not exactly stable because it is affected by the piping and the active number of the FCU in the building; however, during operation this flow rate is kept approximately at 25 m^3/h.

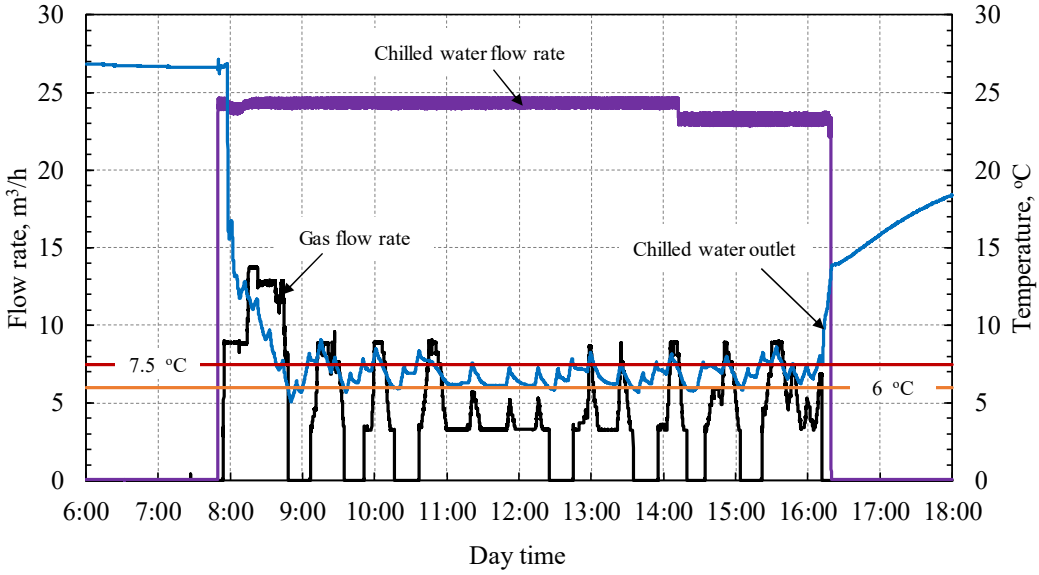

Fig. 3.12 Gas and chilled water flow rate

3.3 Typical field test results

Typical experimental data collected based on the field test in Indonesia is shown in this section. The experimental data collected on September 22nd, 2014 is used to describe the operation of this system when working in tropical climates.

Fig. 3.13 shows the data of solar radiation and ambient temperature from 7:00 until 17:00. Solar radiation attained a maximum value of approximately 800 W/m^2 during the middle hours of the day (11:00 – 12:00). The average solar radiation during the system operation period of 8:00 until 16:00 was 581 W/m^2. In certain instances, the solar radiation suddenly decreased because at that time the sky became partially cloudy. The other data, namely the ambient temperature, increased until the maximum temperature of approximately 37.2 °C was reached and yielded an average temperature of approximately 35 °C when the system was functional.

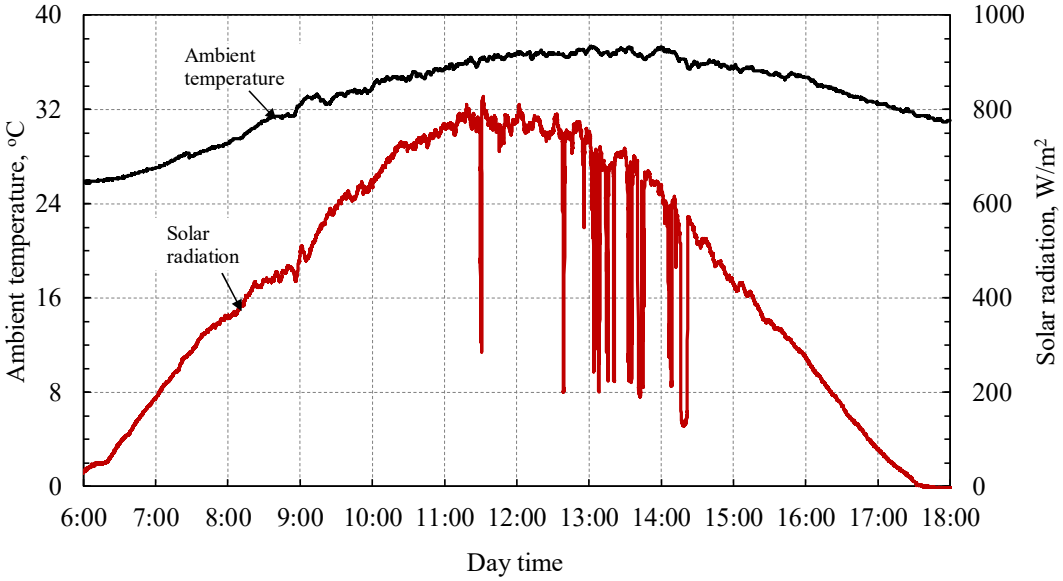

Fig. 3.13 Solar radiation and ambient temperature variation during daytime hours

In order to show the field test results at the University of Indonesia based on the control operation of Figs. 3.2, 3.4, 3.6, and 3.7 and the Indonesian weather (Fig. 3.13), all the temperature measurement points in Fig. 2.10 are plotted in Figs. 3.14–3.16.

Fig. 3.14 shows the inlet and outlet of the hot water, cooling water and chiller water temperatures. The hot water collector outlet temperature is highly influenced by the amount of solar radiation. Therefore, its tendency is almost the same with the solar radiation tendency. Around 7:45 am, the hot water pump 1 starts circulating the hot water between the hot water storage tank and the solar collectors, thus the hot water collector decrease sharply and the hot water chiller inlet increase suddenly. After they reach the temporary equilibrium, then they increase gradually (Fig. 3.14) when solar radiation increases (Fig. 3.13).

In Fig. 3.14, before the hot water pump 2 starts working, the hot water chiller inlet temperature is higher than the hot water chiller inlet temperature. But when the hot water pump 2 starts circulating the hot water between the hot water storage tank and the chiller, then the hot water from the chiller mixes with the hot water from the collector at the hot water storage tank. Eventually, the hot water chiller inlet temperature becomes higher than the hot water collector inlet temperature. Between 8:00 am to 9:00 am, the hot water chiller temperature is moderately fluctuating because the amount of solar energy is insufficient to generate hot water chiller temperature 3 °C higher than the solution outlet temperature of the special temperature generator (the dark green line, Fig. 3.15).

The tendency of the cooling water temperature in Fig. 3.14 is affected by the control operation in Fig. 3.4. The cooling water inlet temperature is kept with minimum value is 26 °C and maximum is 32 °C by the fan of cooling tower, therefore, its temperature fluctuates according to the ambient temperature and the cooling capacity. On the other hand, the control operation results

of the chilled water temperature by Fig. 3.6 are shown in Fig. 3.14. The chilled water inlet and outlet temperature are mostly influenced by the cooling load and gas combustion.

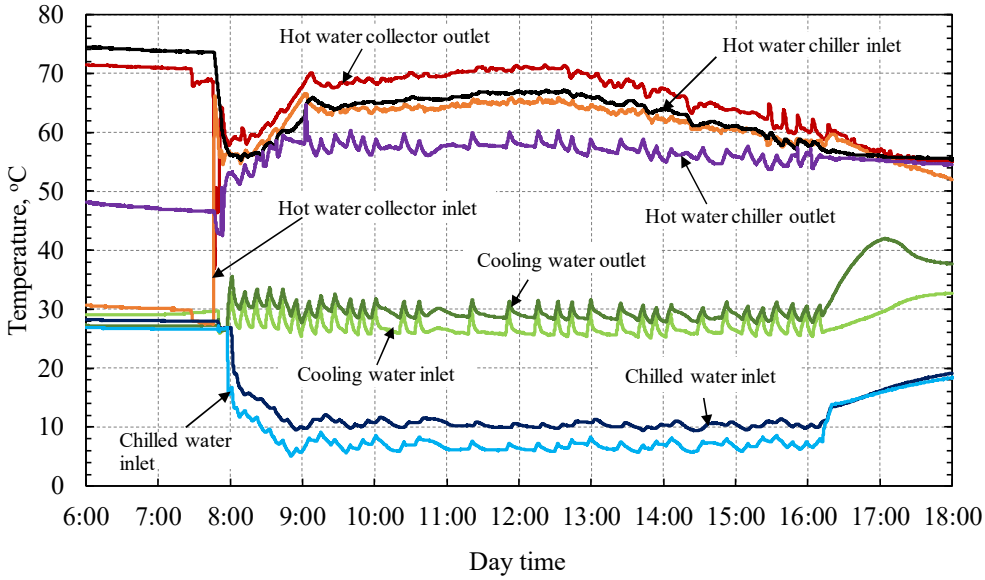

Fig. 3.14 Hot water, cooling water, and chilled water temperatures variation during daytime hours

Fig. 3.15 shows the solution outlet temperature of the special temperature generator, low temperature generator, and high temperature generator, and the solution inlet and outlet temperature of the absorber. The solution outlet temperature of the high temperature generator is highly influenced by the gas combustion (gas consumption in Fig. 3.12). Therefore, the solution outlet temperature of the high temperature generator and the gas flow rate have the same tendency during the chiller operation. Vapour generation in the low temperature generator is heated by the refrigerant vapour coming from the high temperature generator (this can be seen in Fig. 3.16, purple line), thus, each step between the solution outlet temperature of the high and low temperature generator has almost the same trend.

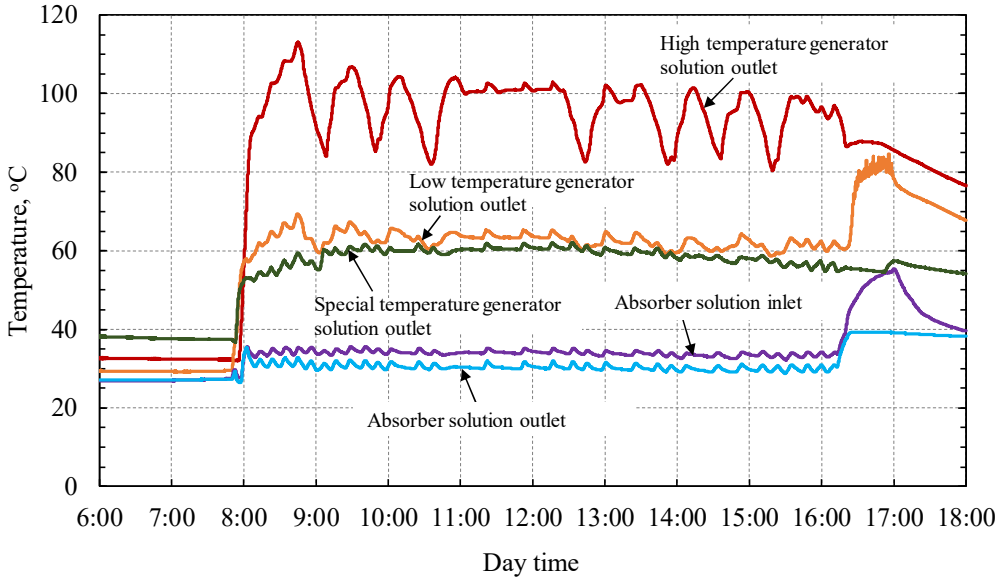

Fig. 3.15 Solution temperatures variation during daytime hours

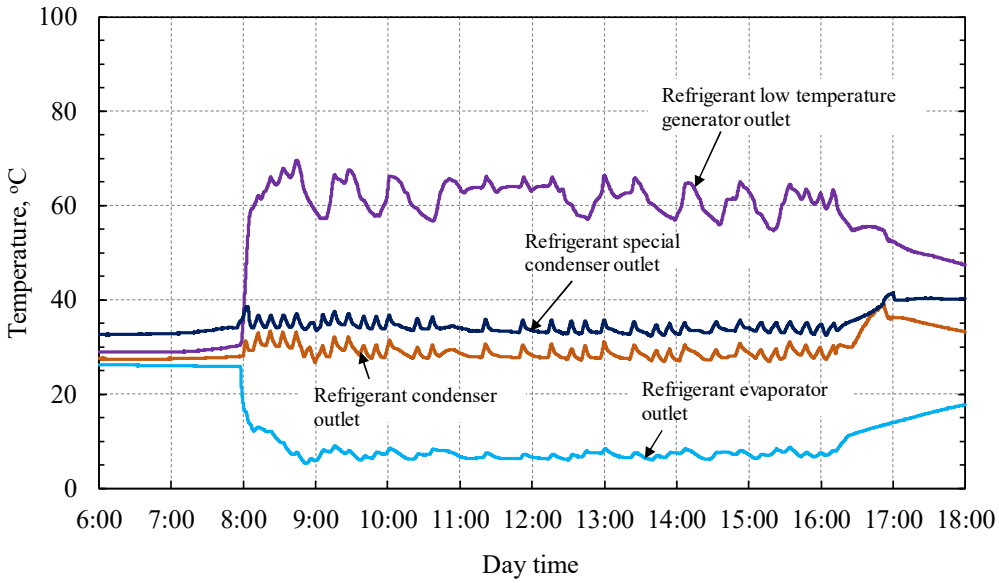

Fig. 3.16 Refrigerant (liquid) temperatures variation during daytime hours

The average cooling capacity is approximately 102 kW (Fig. 3.17). The cooling capacity when the chiller first started at 8:00 is really high because the chilled water inlet and outlet had significant temperature difference. However, this only occurs within several minutes before the capacity drops back to the constant value of approximately 102 kW. The solar energy was fully used together with gas from 09:00 until 16:00. The utilisation of solar energy is affected by solar radiation, ambient temperature, and the cooling water's inlet temperature into the special condenser. The utilisation of the solar energy increases from 08:00 until 13:00, and then decreases until the evening hours. Fig. 3.17 confirms that the solar energy could be extensively utilised. The

global performance of this system during daytime hours is summarised in Fig. 3.18, where COP_{el} accounts for the electricity consumption of the whole system (cooling water pump, chilled water pump, hot water pumps, solution pumps, and cooling tower fan).

This system can be compared with an equivalent vapour compression chiller in terms of primary energy consumption. Provided a reference value of 3.1 (excluding fan's electrical consumption) for the COP of this conventional system [49–51], the primary energy consumption can be calculated, for the same operative cooling load, by assuming a total conversion efficiency of 0.4. When compared with the primary energy consumption experimentally measured during the daytime hours operability of the single-double effect absorption chiller hereby discussed (gas and converted electricity consumption), the use of this latter system gives reductions between 11 and 48%.

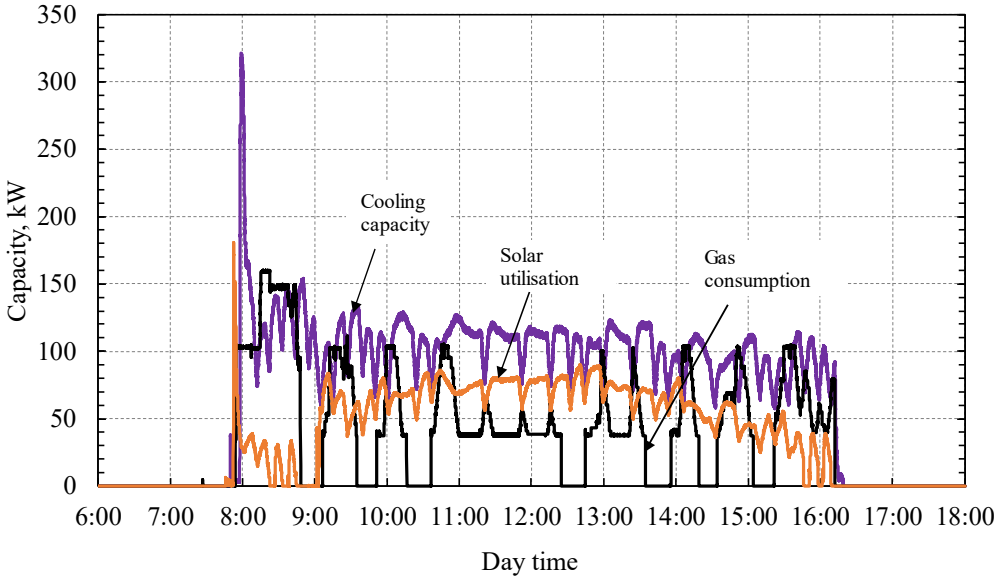

Fig. 3.17 Capacity of cooling, solar utilisation and gas consumption variation during daytime hours, September 22nd, 2014

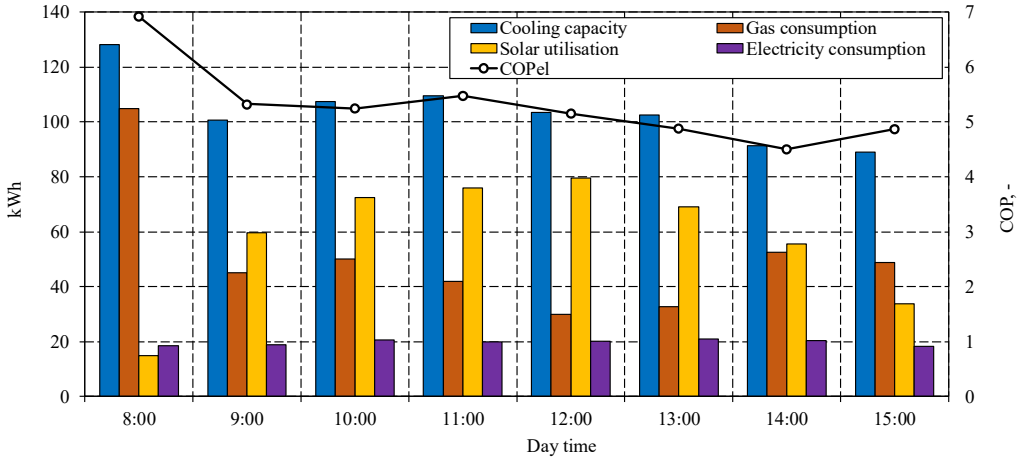

Fig. 3.18 Performance of single-double-effect absorption chiller during daytime hours, September 22nd, 2014

Chapter 4
Simulation Model

Many studies regarding absorption chillers are directed towards the improvement of the system operation performance. To achieve high and safe operation, there are many parameters that must be taken under consideration. As known, a deep understanding of the steady-state and dynamic behaviour of an absorption chiller can be achieved by experimental investigations or numerical simulations.

Conducting an experimental investigation is of the most reliable method to quantify the behaviour of the system. The analysis of the measured data contributes to the physical understanding of the system and can be used to build or validate empirical and theoretical model. Being this an expensive and time consuming approach, after several data from the experimental are obtained, simulation constitutes a suitable method to continue exploring the behaviour of the system beyond the range of the experimental conditions or with a different design. This can save time and money, besides improving the system performance or performing plant diagnostics. The improvement of the level of confidence of the simulations opens up to new operative possibilities, performance maximisation and higher operation safety.

The single-double-effect absorption chiller is a combined cycle from single-effect and double-effect absorption chiller. Featuring additional components, this system is more complex than a standard single- or double-effect absorption chiller in its structure and operation. Therefore, the understanding of this system behaviour becomes of critical importance and the combination of simulation and experimental data represents a proper approach.

In general, there are two kinds of simulation that can be used to understand the characteristics and the performance of the absorption chiller:

1) Steady-state simulations for calculating the absorption chiller performance at time-invariant operation conditions (both on-design and off-design). Under this point of view, the steady-state values of external and internal parameters such as temperature, concentration, pressure, and flow rate of the working fluids are calculated. Moreover, the size of heat exchangers can also be estimated. However, the time-dependency of the thermal behaviour of the absorption chiller cannot be characterised by using steady-state simulations (the output values from the calculation are not time-dependent and are obtained in relation to the given input values). Accordingly, this is not the right method for investigating the control parameters. For the control parameters investigation, the model should be time-dependent.
2) Dynamic models can be used to calculate the transient behaviour of the absorption chiller. In a dynamic model, after the step change of the input parameters, the output results do not change immediately, and it needs a certain time to reach the steady-state. However, for constructing a reliable dynamic model of the system, detailed information on the characteristics that affect the time-response of the system must be considered.

In this chapter, the simulation model of the single-double-effect absorption chiller is constructed for simulating the steady-state and the transient or dynamic conditions in order to confidently obtain the best performance operation with high reliability. Firstly, the understanding of the characteristics and performance of the single-double-effect absorption chiller according to the environment and disturbances through steady-state simulations is necessary. Further, to reach the efficient and stable operation of the single-double-effect absorption chiller, it is indispensable to grasp the detailed behaviour of thermal systems and investigate the optimisation from the design to the operation.

The steady-state and dynamic model of the single-double-effect absorption chiller are presented. This system is driven by dual-heat sources (solar energy and gas) at the same time during most of its operation. As known, the availability of solar energy is influenced by the weather conditions so that the dynamic analysis plays an important role to predict the real characteristics and performance of the system. However, in order to find the optimum condition of this system, the steady-state simulation is needed. For the steady-state and dynamic simulation, the model is based on mass and energy balances, but for dynamic simulation also considers the mass and thermal storage in the evaporator, absorber, and three generators (special, low, and high temperature generator). The Newton-Raphson method with finite-difference Jacobian is applied in MATLAB to solve the approximated differential equations. The steady-state and dynamic simulation results are compared to the experimental data. Furthermore, the model is used to find an appropriate control strategy that can minimise the primary energy consumption, and increase the performance without affecting the stability of the cooling capacity.

Because of the differences between the steady and dynamic models, in this chapter, these are explained in different sub-chapters as follows:

4.1 Steady-state model

Steady-state model and dynamic model are conceptually consistent, but in the first, the time-dependency, the mass storage, and the heat storage are not considered.

The fundamental heat and mass transfer processes are based on the mass and energy balance equations. The energy balance and mass balance are used to evaluate the entire system performance through the performance of each component.

Basically the simulation model between steady-state and dynamic is the same, therefore the explanation of the steady-state is used as a representative to understand the different location of variable between steady-state and dynamic model. Where the description of model of absorber, condenser, and heat exchanger are used for example.

4.1.1 Model assumptions

The simulation model adopted and validated with experimental data is used to investigate the performance of the system in a wider range of conditions. Simulations are carried out considering the following assumptions:

- temperature, pressure, and concentration are homogeneous inside each component;
- there is no heat loss to or gain from the ambient;
- the piping pressure drop is disregarded;
- the water vapour inside the evaporator and condenser is saturated;
- the LiBr/water solution leaves the generator and absorber at saturation point;
- all throttling valves are isenthalpic;

4.1.2 Description of the model

Absorber and Generators

The mass balance of the solution in the absorber can be written as follows:

$$\dot{m}_{v,A} + \dot{m}_{s,out,M} - \dot{m}_{s,out,A} = 0 \tag{4.1}$$

$$\dot{m}_{s,out,M} X_{s,out,M} - \dot{m}_{s,out,A} X_{s,out,A} = 0 \tag{4.2}$$

Where X is the mass fraction of LiBr in the solution, which is a function of the solution temperature and saturation pressure/temperature of the water refrigerant.

$$X_{s,out,A} = f(T_{s,out,A}, T_{sat,E}) \tag{4.3}$$

Furthermore, the internal (solution side) and external (water side) energy balances are respectively expressed as follows:

$$\dot{m}_{s,out,M} h_{ss,out,LHX} + \dot{m}_{v,A} h_{v,A} - \dot{m}_{s,out,A} h_{s,out,A} - UA_A \Delta T_{LMTD,A} = 0 \tag{4.4}$$

$$\dot{m}_{cw} C_{p,cw} \left(T_{cw,C} - T_{cw,A}\right) + UA_A \Delta T_{LMTD,A} = 0 \tag{4.5}$$

The logarithmic mean temperature difference (LMTD) at the absorber is expressed by Eq. 4.6. To calculate the LMTD, the inside temperature of the absorber is used instead of the inlet temperature because the small influence of the sensible [52].

$$\Delta T_{LMTD,A} = \frac{\left(T_{s,inside,A} - T_{cw,C}\right) - \left(T_{s,out,A} - T_{cw,A}\right)}{ln \frac{\left(T_{s,inside,A} - T_{cw,C}\right)}{\left(T_{s,out,A} - T_{cw,A}\right)}} \tag{4.6}$$

The governing equations for STG and HTG are equivalent to Eqs. 4.1−4.6, whereas, the LTG,

being driven by the vapour generated in the HTG, uses Eq. 4.7 for the water side energy balance.

$$\dot{m}_{r,out,HTG}\left(h_{sh,HTG} - h_{r,HTG}\right) + UA_{LTG}\,\Delta T_{LMTD,LTG}=0 \tag{4.7}$$

Evaporator and condensers

The condenser (C) is assumed able to liquefy the whole vapour flow rate derived from the low-temperature generator. Therefore, the mass balance of the refrigerant is written as follows:

$$\dot{m}_{v,out,LTG} - \dot{m}_{r,out,LTG} = 0 \tag{4.8}$$

The energy balance of the condenser is shown in Eq. 4.9 and 4.10, where the related logarithmic mean temperature difference is defined by Eq. 4.11.

$$\dot{m}_{r,out,LTG}\left(h_{sh,LTG} - h_{r,C}\right) - UA_C\,\Delta T_{LMTD,C}=0 \tag{4.9}$$

$$\dot{m}_{cw}C_{p,cw,C}\left(T_{cw,SC} - T_{cw,C}\right)+UA_C\,\Delta T_{LMTD,C}=0 \tag{4.10}$$

$$\Delta T_{LMTD,C} = \frac{\left(T_{sat,C} - T_{cw,SC}\right) - \left(T_{sat,C} - T_{cw,C}\right)}{ln\dfrac{\left(T_{sat,C} - T_{cw,SC}\right)}{\left(T_{sat,C} - T_{cw,C}\right)}} \tag{4.11}$$

The heat and mass balances for the evaporator and special condenser are equivalent to Eqs. 4.8–4.11.

Low- and high-temperature heat exchangers

The mass balance of the low-temperature heat exchanger can be written as follows:

$$\dot{m}_{s,out,M}\left(X_{s,out,M} - X_{s,out,M}\right)=0 \tag{4.12}$$

$$\dot{m}_{s,out,A}\left(X_{s,out,A} - X_{s,out,A}\right)=0 \tag{4.13}$$

The strong solution concentration side and weak solution concentration side energy balances are respectively calculated as follows:

$$\dot{m}_{s,out,M}\left(h_{s,out,M} - h_{ss,out,LHX}\right) - UA_{LHX}\,\Delta T_{LMTD,LHX}=0 \tag{4.14}$$

$$\dot{m}_{s,out,A}\left(h_{s,out,A} - h_{ws,out,LHX}\right) + UA_{LHX}\,\Delta T_{LMTD,LHX}=0 \tag{4.15}$$

The logarithmic mean temperature difference at the LHX is written as follows:

$$\Delta T_{LMTD,LHX} = \frac{\left(T_{s,out,M} - T_{ws,out,LHX}\right) - \left(T_{ss,in,LHX} - T_{s,out,A}\right)}{ln\frac{\left(T_{s,out,M} - T_{ws,out,LHX}\right)}{\left(T_{ss,in,LHX} - T_{s,out,A}\right)}} \quad (4.16)$$

The heat and mass balances for the high-temperature heat exchanger is equivalent to Eqs. 4.12–4.16.

4.2 Dynamic modelling

4.2.1 Model assumption

In order to simplify the mathematical model of the single-double-effect absorption chiller, some assumptions are made as follows:

- The thermal capacity of vessel and tube are calculated from the full load experimental condition.
- The mass and the specific heat of the vessel and tube are constant.
- There is no solution transport delay.
- There is no heat loss to the environment.
- The solution pump work is ignored.
- The LiBr/water solution is saturated at the outlet tube bundle and the outlet of absorber and generators.
- The refrigerant is saturated at the outlet of evaporator and condensers.

4.2.2 Description of the model

The mathematical equations of each component are described as follows:

Absorber and Evaporator

Absorber and evaporator are in the same vessel (Fig. 4.1). The heat from the chilled water is released into the liquid refrigerant, which evaporates the liquid refrigerant. The vapour refrigerant is then absorbed by the LiBr-H_2O solution in the absorber. Thus the mathematical model of the absorber and the evaporator are related especially for the mass balance. For the sake of ease of understanding, the mathematical model is written in relation to each component.

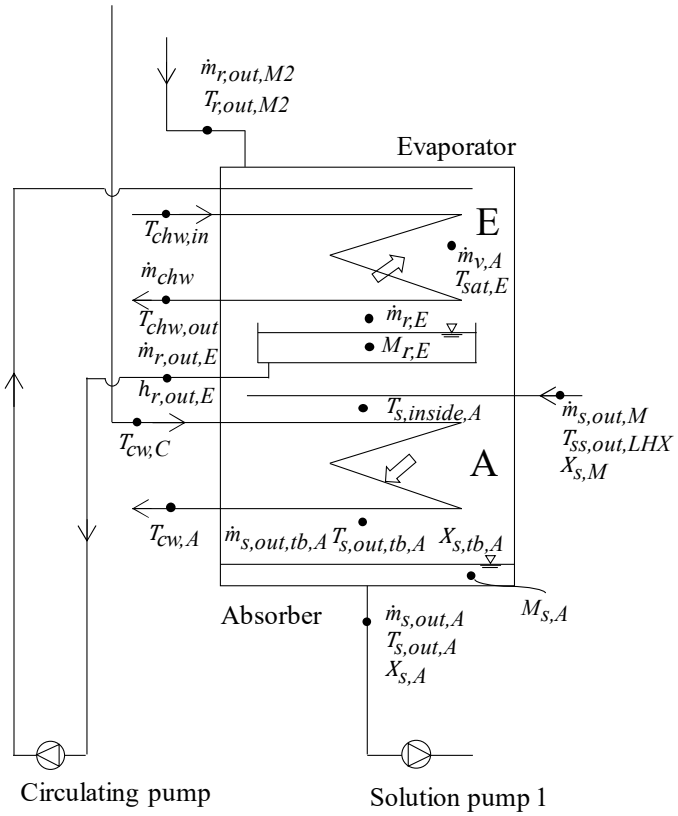

Fig. 4.1 Absorber and evaporator

Absorber

The mass balance between the absorber and the evaporator is modelled in Eq. 4.17. The vapour refrigerant $\dot{m}_{v,A}$ is absorbed by the solution from the mixer $\dot{m}_{s,out,M}$, hence moving from the absorber tube bundle to the solution sump at the absorber. The solution mass balance between the inlet and outlet of the absorber tube bundle is represented by Eq. 4.18. The solution amassed on the tube bundle can be neglected because it is very small if compared the solution sump at the absorber P. Kohlenbach and F. Ziegler (2008) [53, 54].

$$\dot{m}_{s,out,M}+\dot{m}_{v,A}-\dot{m}_{s,out,tb,A}=0 \tag{4.17}$$

$$\dot{m}_{s,out,M}X_{s,M}-\dot{m}_{s,out,tb,A}X_{s,tb,A}=0 \tag{4.18}$$

For the mass storage, the solution sump amount and the mass fraction of the solution at the absorber outlet are time-dependent, and these depend on the solution mass flow rates from the tube bundle and at the absorber outlet (total solution mass flow rate) (Eq. 4.19 and Eq. 4.20).

$$\dot{m}_{s,out,tb,A}X_{s,tb,A}-\dot{m}_{s,out,A}X_{s,A}-\frac{dM_{s,A}X_{s,A}}{dt}=0 \tag{4.19}$$

$$\dot{m}_{s,out,tb,A} - \dot{m}_{s,out,A} - \frac{dM_{s,A}}{dt} = 0 \tag{4.20}$$

The energy balance and the heat capacity storage of the absorber between the solution and the cooling water are written in the Eqs. 4.21, 4.22, and 4.24. The heat transfers between the cooling water and the LiBr/water solution at the absorber occurs in the tube bundle. The heat capacity of the solution amassed on the tube bundle is neglected; therefore, the heat capacity storage is related only to the cooling water, vessel, and tube (Eq. 4.22). The mass and the specific heat of the tube and vessel are assumed constant (shell, tube, tube plate, water box, and water box cover), and only the temperature of cooling water changes according to the time. Equation 4.23 shows the heat capacity storage in the solution sump at the absorber vessel.

$$\dot{m}_{s,out,M} h_{ss,out,LHX} + \dot{m}_{v,A} h_{v,A} - \dot{m}_{s,out,tb,A} h_{s,tb,A} - UA_A \, \Delta T_{LMTD,A} = 0 \tag{4.21}$$

$$\dot{m}_{cw} C_{p,cw,A} \left(T_{cw,C} - T_{cw,A} \right) + UA_A \, \Delta T_{LMTD,A} - \left(MC_{p,cw,A} \frac{dT_{cw,avg,A}}{dt} + \frac{dM_{cw,A} h_{cw,avg,A}}{dt} \right) = 0 \tag{4.22}$$

$$\dot{m}_{s,out,tb,A} h_{s,tb,A} - \dot{m}_{s,out,A} h_{s,A} - \left(MC_{p,s,A} \frac{dT_{s,out,A}}{dt} + \frac{dM_{s,A} h_{s,A}}{dt} \right) = 0 \tag{4.23}$$

The logarithmic mean temperature difference at the absorber (Eq. 4.24) is written as follows:

$$\Delta T_{LMTD,A} = \frac{\left(T_{s,inside,A} - T_{cw,C} \right) - \left(T_{s,out,tb,A} - T_{cw,A} \right)}{ln \frac{\left(T_{s,inside,A} - T_{cw,C} \right)}{\left(T_{s,out,tb,A} - T_{cw,A} \right)}} \tag{4.24}$$

The absorber solution outlet and inside temperatures are defined by Eqs. 4.25 and 4.26, respectively.

$$T_{s,out,tb,A} = f\left(X_{s,tb,A}, T_{sat,E} \right) \tag{4.25}$$

$$T_{s,inside,A} = f\left(X_{s,M}, T_{sat,E} \right) \tag{4.26}$$

The solution mass storage of the absorber $M_{s,A}$ is calculated from the volume and the solution density of the absorber outlet $\rho_{s,out,A}$ (Eq. 4.27). While the volume is obtained by multiplying the constant bottom area of the solution storage $A_{btm,A}$ and the level of the solution $l_{s,A}$. Therefore, the mass storage amount can be expressed by Eq. 4.28.

$$\rho_{s,out,A} = f\left(X_{s,A}, T_{s,out,A} \right) \tag{4.27}$$

$$M_{s,A}=A_{btm,A}l_{s,A}\rho_{s,out,A} \tag{4.28}$$

In addition, the above mentioned enthalpy values, the average temperature, and the specific heat are obtained from the equations (4.29–4.35), referring to the thermos-physical properties of [ASHRAE and 1980 SI the Japan Society of Mechanical Engineers Steam Table], as follows:

$$h_{ss,out,LHX}=f\left(X_{s,out,M},T_{ss,out,LHX}\right) \tag{4.29}$$

$$h_{s,tb,A}=f\left(X_{s,tb,A},T_{s,tb,A}\right) \tag{4.30}$$

$$h_{v,A}=f\left(T_{sat,E}\right) \tag{4.31}$$

$$h_{cw,avg,A}=f\left(P_{cw},T_{cw,avg,A}\right) \tag{4.32}$$

$$h_{s,out,A}=f\left(X_{s,out,A},T_{ss,out,A}\right) \tag{4.33}$$

$$T_{cw,avg,A}=\frac{T_{cw,A}+T_{cw,C}}{2} \tag{4.34}$$

$$C_{p,cw,A}=f\left(P_{cw},T_{cw,A}\right) \tag{4.35}$$

Evaporator

The mass balance between the evaporator and the absorber is written in Eq. 4.36. The mass balance includes the liquid refrigerant from mixer 2 $\dot{m}_{r,out,M2}$ mixed with the liquid refrigerant from the bottom of the evaporator $\dot{m}_{r,out,E}$, where the liquid refrigerant is circulated by circulating pump from the refrigerant sump. The total liquid refrigerant is then reduced by the evaporating proses in the tube bundle. The evaporated refrigerant $\dot{m}_{v,A}$ goes to the absorber, and part of the liquid refrigerant on the evaporator tube bundle returns to the refrigerant sump $\dot{m}_{r,E}$. Accordingly, the refrigerant storage at the evaporator is calculated by Eq. 4.37.

$$\dot{m}_{r,out,M2}+\dot{m}_{r,out,E}-\dot{m}_{v,A}-\dot{m}_{r,E}=0 \tag{4.36}$$

$$\dot{m}_{r,E}-\dot{m}_{r,out,E}-\frac{dM_{r,E}}{dt}=0 \tag{4.37}$$

The energy balance and the heat transfer between the refrigerant and the chilled water are expressed by Eqs. 4.38 and 4.39. In a corresponding manner to the absorber, the heat capacity storage only exists at the chilled water inside the tube bundle (Eq. 4.39) and the refrigerant sump (Eq. 4.40). Specifically, the enthalpy at the state between the liquid refrigerant from the tube bundle $h_{r,E}$ and the liquid refrigerant outlet the sump $h_{r,out,E}$ differs from each other because of

the pressure difference. The vapour refrigerant from the evaporator to the absorber $h_{v,A}$ is assumed at saturation. As the liquid refrigerant enthalpy of the mixer 2 is at saturation condition, therefore, it is influenced by the evaporator and the mixer 2 calculation.

$$\dot{m}_{r,out,M2}h_{r,out,M2} + \dot{m}_{r,out,E}h_{r,out,E} - \dot{m}_{v,A}h_{v,A} - \dot{m}_{r,E}h_{r,E} + UA_E\,\Delta T_{LMTD,E}=0 \tag{4.38}$$

$$\dot{m}_{chw}C_{p,chw}\left(T_{chw,in} - T_{cw,out}\right) - UA_E\,\Delta T_{LMTD,E} - \left(MC_{p,cw,E}\frac{dT_{chw,avg,E}}{dt} + \frac{dM_{chw,E}h_{chw,avg,E}}{dt}\right)=0 \tag{4.39}$$

$$\dot{m}_{r,E}h_{r,E} - \dot{m}_{r,out,E}h_{r,out,E} - \left(MC_{p,r,E}\frac{dT_{r,E}}{dt} + \frac{dM_{r,E}h_{r,out,E}}{dt}\right)=0 \tag{4.40}$$

The logarithmic mean temperature difference at the evaporator is expressed in Eq. 4.41. The saturation temperature in the evaporator is obtained from the water properties [1980 SI the Japan Society of Mechanical Engineers Steam Table].

$$\Delta T_{LMTD,E} = \frac{\left(T_{chw,in} - T_{sat,E}\right) - \left(T_{chw,out} - T_{sat,E}\right)}{ln\frac{\left(T_{chw,in} - T_{sat,E}\right)}{\left(T_{chw,out} - T_{sat,E}\right)}} \tag{4.41}$$

Where,

$$h_{r,E}=f\left(T_{sat,E}\right) \tag{4.42}$$

$$h_{chw,avg,E}=f\left(P_{chw}, T_{chw,avg,E}\right) \tag{4.43}$$

$$T_{chw,avg,E}=\frac{T_{chw,in}+T_{cw,out}}{2} \tag{4.44}$$

$$C_{p,chw}=f\left(P_{chw}, T_{chw,out}\right) \tag{4.45}$$

The liquid refrigerant mass storage of the evaporator $M_{s,E}$ is calculated by multiplying the area, the level, and the density of the liquid refrigerant outlet from the storage $\rho_{r,out,E}$ (Eq. 4.46). The density can be obtained by knowing the pressure (this pressure is obviously higher than the evaporation pressure, but since, the effect of the level on pressure is not considered, then this value is assumed to be constant 100 kPa since the density from this enthalpy between 10 to 100 kPa does not change significantly) and the enthalpy of the liquid refrigerant outlet. The volume is obtained by multiplying the constant area $A_{btm,E}$ and the level of the solution $l_{r,E}$. Therefore, the mass storage amount can be expressed in Eq. 4.47.

$$\rho_{r,out,E}=f\left(P_{r,out,E},h_{r,out,E}\right) \tag{4.46}$$

$$M_{r,E}=A_{btm,E}l_{r,E}\rho_{r,out,E} \tag{4.47}$$

The chilled water mass storage (Eq. 48) in the evaporator is calculated by the total volume $V_{chw,E}$ of the water box and the tube bundle, times the chilled water density (Eq. 4.49).

$$M_{chw,E}=Vl_{chw,E}\rho_{chw,out} \tag{4.48}$$

$$\rho_{chw,out}=f\left(P_{chw},T_{chw,out}\right) \tag{4.49}$$

Low temperature heat exchanger

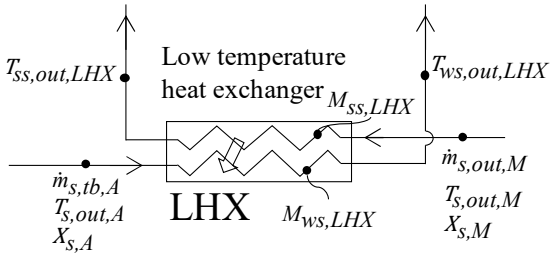

Fig. 4.2 Low temperature heat exchanger

Fig. 4.2 illustrates the mass flow rate, concentration, and temperature of the strong and weak solution within the low temperature heat exchanger. Inlet and outlet energy fluxes, heat transfer, and heat capacity storage at the solution and the plate are considered when writing the energy balance on both side of the heat exchanger (Eqs. 4.50 and 4.51). The solution mass flow rate and the concentration remain constant.

$$\begin{aligned}\dot{m}_{s,out,M}\left(h_{s,out,M}-h_{ss,out,LHX}\right)-UA_{LHX}\Delta T_{LMTD,LHX}\\ -\left(MC_{p,ss,LHX}\frac{dT_{ss,avg,LHX}}{dt}+\frac{dM_{ss,LHX}h_{ss,avg,LHX}}{dt}\right)=0\end{aligned} \tag{4.50}$$

$$\begin{aligned}\dot{m}_{s,out,A}\left(h_{s,out,A}-h_{ws,out,LHX}\right)+UA_{LHX}\Delta T_{LMTD,LHX}\\ -\left(MC_{p,ws,LHX}\frac{dT_{ws,avg,LHX}}{dt}+\frac{dM_{ws,LHX}h_{ws,avg,LHX}}{dt}\right)=0\end{aligned} \tag{4.51}$$

where,

$$h_{s,out,M}=f\left(X_{s,out,M},T_{s,out,M}\right) \tag{4.52}$$

$$h_{ws,out,LHX}=f\left(X_{s,out,A},T_{ws,out,LHX}\right) \tag{4.53}$$

$$h_{ws,avg,LHX}=f\left(X_{s,out,A},T_{ws,avg,LHX}\right) \tag{4.54}$$

$$h_{ss,avg,LHX}=f\left(X_{s,out,M},T_{ss,avg,LHX}\right) \tag{4.55}$$

The logarithmic mean temperature difference at the low temperature heat exchanger is defined in Eq. 4.56.

$$\Delta T_{LMTD,LHX}=\frac{\left(T_{s,out,M}-T_{ws,out,LHX}\right)-\left(T_{ss,in,LHX}-T_{s,out,A}\right)}{ln\frac{\left(T_{s,out,M}-T_{ws,out,LHX}\right)}{\left(T_{ss,in,LHX}-T_{s,out,A}\right)}} \tag{4.56}$$

The strong and the weak solution storage volume at the low temperature heat exchanger are calculated from the total volume of the tube shell. The two sides are assumed to have the same volume, therefore, the strong and the weak solution occupies the half of the total volume storage each (Eqs. 4.55–4.56)

$$\rho_{ws,avg,LHX}=f\left(X_{s,A},T_{ws,avg,LHX}\right) \tag{4.57}$$

$$\rho_{ss,avg,LHX}=f\left(X_{s,M},T_{ss,avg,LHX}\right) \tag{4.58}$$

$$M_{ws,LHX}=\frac{Vl_{LHX}}{2}\rho_{ws,avg,LHX} \tag{4.59}$$

$$M_{ss,LHX}=\frac{Vl_{LHX}}{2}\rho_{ss,avg,LHX} \tag{4.60}$$

$$T_{ws,avg,LHX}=\frac{T_{s,out,A}+T_{ws,in,LHX}}{2} \tag{4.61}$$

$$T_{ss,avg,LHX}=\frac{T_{s,out,M}-T_{ss,out,LHX}}{2} \tag{4.62}$$

Mixer 1 and mixer 2

Fig. 4.3 shows the mixer for the liquid refrigerant from the low temperature generator, condenser, and special condenser. In these mixers, the mass balance and energy balance are used to calculate the outlet mass flow rate and temperature.

Mixer 1

Assuming a perfect mixing process, the mixer 1 combines the liquid refrigerant from the low temperature generator $\dot{m}_{r,out,HTG}$ and condenser $\dot{m}_{r,out,LTG}$ into $\dot{m}_{r,out,M1}$. This is calculated from Eq. 4.64. Since the pressure of the mixer 1 is not well known; it is difficult to define the right temperature. Therefore, the enthalpy liquid refrigerant temperature of the mixer 1 is obtained directly from Eq. 4.64.

$$\dot{m}_{r,out,LTG}+\dot{m}_{r,out,HTG}-\dot{m}_{r,out,M1}=0 \tag{4.63}$$

$$\dot{m}_{r,out,LTG}h_{r,C}+\dot{m}_{r,out,HTG}h_{r,out,HTG}-\dot{m}_{r,out,M1}h_{r,out,M1}=0 \tag{4.64}$$

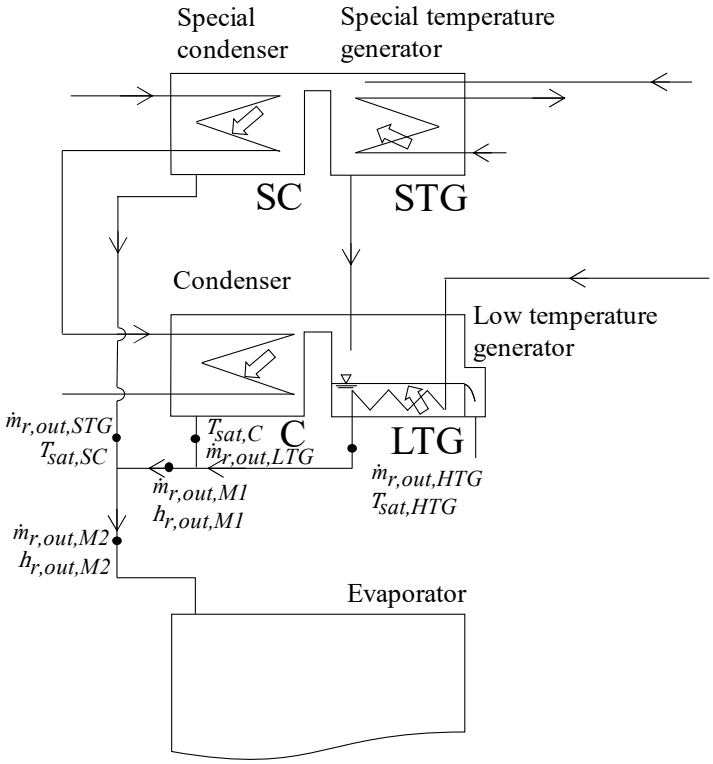

Fig. 4.3 Mixer 1 and mixer 2

Mixer 2

For the mixer 2, the total mass balance (Eq. 4.65) and the energy balance (Eq. 4.66) are used to obtain the mass flow rate and the enthalpy of the liquid refrigerant of the mixer 2.

$$\dot{m}_{r,out,STG}+\dot{m}_{r,out,M1}-\dot{m}_{r,out,M2}=0 \tag{4.65}$$

$$\dot{m}_{r,out,STG}h_{r,SC}+\dot{m}_{r,out,M1}h_{r,out,M1}-\dot{m}_{r,out,M2}h_{r,out,M2}=0 \tag{4.66}$$

where,

$$h_{r,C}=f\left(T_{sat,C}\right) \tag{4.67}$$

$$h_{r,out,HTG}=f\left(T_{sat,HTG}\right) \tag{4.68}$$

$$h_{r,SC}=f\left(T_{sat,SC}\right) \tag{4.69}$$

Low temperature generator and condenser

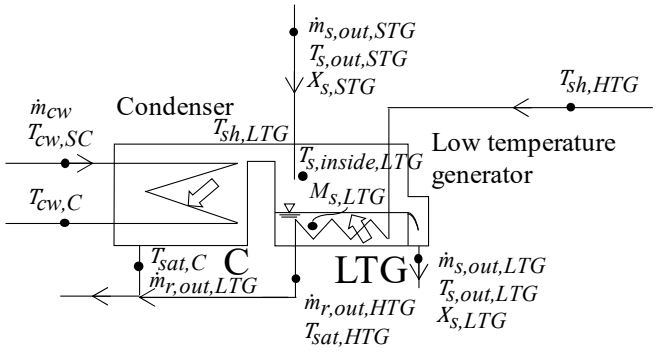

Fig. 4.4 Low temperature generator and condenser

The schematic diagram of the low temperature generator and the condenser are shown in Fig. 4.4. The low temperature generator does not only work for generating the vapour, but it also works as a condenser for the vapour refrigerant from the high temperature generator. Therefore, the pool boiling type of heat exchanger is applied to the low temperature generator. Meanwhile, the vapour refrigerant generated by the low temperature generator is condensed by the condenser. Finally, both liquid refrigerant from the low temperature generator and the condenser are mixed by the mixer 1.

Low temperature generator

The low temperature generator features a pool boiling configuration, therefore, the volume of the solution is kept constant to guarantee the condensation inside the tube bundle. The total mass storage and the LiBr storage are calculated as in Eqs. 4.70 and 4.71, respectively. The energy fluxes, heat transfer, and heat storage of the solution are included when calculating the energy balance (Eq. 4.72).

$$\dot{m}_{s,out,STG} - \dot{m}_{s,out,LTG} - \dot{m}_{r,out,LTG} - \frac{dM_{s,LTG}}{dt} = 0 \tag{4.70}$$

$$\dot{m}_{s,out,STG} X_{s,STG} - \dot{m}_{s,out,LTG} X_{s,LTG} - \frac{dM_{s,LTG} X_{s,LTG}}{dt} = 0 \tag{4.71}$$

$$\begin{aligned} \dot{m}_{s,out,STG} h_{s,out,STG} - \dot{m}_{s,out,LTG} h_{s,out,LTG} - \dot{m}_{r,out,LTG} h_{sh,LTG} \\ + UA_{LTG}\, \Delta T_{LMTD,LTG} \\ - \left(MC_{p,s,LTG} \frac{dT_{s,out,LTG}}{dt} + \frac{dM_{s,LTG} h_{s,out,LTG}}{dt} \right) = 0 \end{aligned} \tag{4.72}$$

On the refrigerant side, inside the tube bundle, it is assumed that there is no heat and mass storage. Therefore, the energy balance is calculated by using Eq. 4.73.

$$\dot{m}_{r,out,HTG} \left(h_{sh,HTG} - h_{r,HTG} \right) + UA_{LTG}\, \Delta T_{LMTD,LTG} = 0 \tag{4.73}$$

where,

$$h_{s,out,STG} = f\left(X_{s,out,STG}, T_{s,out,STG} \right) \tag{4.74}$$

$$h_{s,out,LTG} = f\left(X_{s,out,LTG}, T_{s,out,LTG} \right) \tag{4.75}$$

$$h_{sh,LTG} = f\left(P_{sat,C}, T_{sh,LTG} \right) \tag{4.76}$$

$$h_{r,HTG} = f\left(T_{sat,HTG} \right) \tag{4.77}$$

The logarithmic mean temperature difference at the low temperature generator is calculated by using Eq. 4.78.

$$\Delta T_{LMTD,LTG} = \frac{\left(T_{sat,HTG} - T_{s,inside,LTG} \right) - \left(T_{sat,HTG} - T_{s,out,LTG} \right)}{ln \frac{\left(T_{sat,HTG} - T_{s,inside,LTG} \right)}{\left(T_{sat,HTG} - T_{s,out,LTG} \right)}} \tag{4.78}$$

The outlet (Eq. 4.79) and inside (Eq. 4.80) temperature of the solution are obtained by the properties of the solution [ASHRAE] the superheated temperature of the vapour is calculated from the average between the inside and the outlet temperature of the solution (Eq. 4.81). The saturation temperature of the refrigerant from the high temperature generator is obtained from the energy balance equations between the low temperature generator and the high temperature generator (Eq. 4.73).

$$T_{s,out,LTG} = f\left(X_{s,LTG}, T_{sat,C}\right) \tag{4.79}$$

$$T_{s,inside,LTG} = f\left(X_{s,STG}, T_{sat,C}\right) \tag{4.80}$$

$$T_{sh,LTG} = \frac{T_{s,out,LTG} + T_{s,inside,LTG}}{2} \tag{4.81}$$

The solution sump of the low temperature generator is assumed to be constant in its volume. Therefore, the solution mass storage can be calculated by Eqs. 4.78 and 4.79.

$$M_{s,LTG} = Vl_{LTG}\rho_{s,out,LTG} \tag{4.82}$$

$$\rho_{s,out,LTG} = f\left(X_{s,out,LTG}, T_{s,out,LTG}\right) \tag{4.83}$$

Condenser

In the condenser, the condensed vapour refrigerant flows to the mixer 2 and there is no refrigerant storage. The energy balance of the refrigerant is calculated as in Eq. 4.84. At the cooling water side, the energy fluxes, heat transfer, and the heat and mass storage are included in the energy balance (Eq. 4.85). The logarithmic mean temperature difference at the condenser is obtained by Eq. 4.86.

$$\dot{m}_{r,out,LTG}\left(h_{sh,LTG} - h_{r,C}\right) - UA_C\,\Delta T_{LMTD,C} = 0 \tag{4.84}$$

$$\dot{m}_{cw}C_{p,cw,C}\left(T_{cw,SC} - T_{cw,C}\right) + UA_C\,\Delta T_{LMTD,C} - \left(MC_{p,cw,C}\frac{dT_{cw,avg,C}}{dt} + \frac{dM_{cw,C}h_{cw,avg,C}}{dt}\right) = 0 \tag{4.85}$$

$$\Delta T_{LMTD,C} = \frac{\left(T_{sat,C} - T_{cw,SC}\right) - \left(T_{sat,C} - T_{cw,C}\right)}{ln\frac{\left(T_{sat,C} - T_{cw,SC}\right)}{\left(T_{sat,C} - T_{cw,C}\right)}} \tag{4.86}$$

where,

$$C_{p,cw,C}=f(P_{cw}, T_{cw,C}) \tag{4.87}$$

$$h_{cw,avg,C}=f(P_{cw}, T_{cw,avg,C}) \tag{4.88}$$

$$T_{cw,avg,C}=\frac{T_{cw,SC}+T_{cw,C}}{2} \tag{4.89}$$

The tube bundle and water box volume at the condenser are constant. Therefore, the cooling water mass storage can be calculated by Eqs. 4.90 and 4.91.

$$M_{cw,C}=Vl_{cw,C}\rho_{cw,C} \tag{4.90}$$

$$\rho_{cw,C}=f(P_{cw}, T_{cw,C}) \tag{4.91}$$

Special temperature generator and special condenser

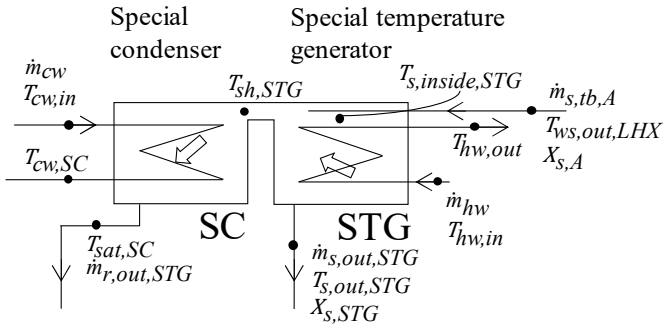

Fig. 4.5 Special temperature generator and special condenser

The special temperature generator and the special condenser utilise the solar energy to generate the vapour refrigerant from the solution and then, condense the vapour refrigerant phase. Therefore, the cooling water flow starts from the special condenser in order to maximise the use of solar energy.

Special temperature generator

This component uses the falling film type of heat exchanger. The vapour refrigerant at the special temperature generator is generated by using the heat from the solar energy. This heat is delivered by the circulation of the hot water. The total mass balance of the solution and the LiBr can be seen in Eqs. 4.92 and 4.93. Based on the actual system, the mass balance equations ignore the solution storage in order to keep constant the solution level at the low temperature generator.

$$\dot{m}_{s,out,A} - \dot{m}_{s,out,STG} - \dot{m}_{r,out,STG} = 0 \tag{4.92}$$

$$\dot{m}_{s,out,A} X_{s,A} - \dot{m}_{s,out,STG} X_{s,STG} = 0 \tag{4.93}$$

Eqs. 4.94 and 4.95 are written to calculate the energy balance of the internal side (solution) and external side (hot water), respectively. While the logarithmic mean temperature difference at the special temperature generator is calculated by using Eq. 4.96.

$$\begin{aligned} \dot{m}_{s,out,A} h_{ws,out,LHX} - \dot{m}_{s,out,STG} h_{s,out,STG} \\ - \dot{m}_{r,out,STG} h_{r,out,STG} + UA_{STG}\, \Delta T_{LMTD,STG} = 0 \end{aligned} \tag{4.94}$$

$$\begin{aligned} \dot{m}_{hw} C_{p,hw} \left(T_{hw,in} - T_{hw,out} \right) - UA_{STG}\, \Delta T_{LMTD,STG} \\ - \left(MC_{p,hw} \frac{dT_{hw,avg,STG}}{dt} + \frac{dM_{hw} h_{hw,avg,STG}}{dt} \right) = 0 \end{aligned} \tag{4.95}$$

$$\Delta T_{LMTD,STG} = \frac{\left(T_{hw,in} - T_{s,inside,STG} \right) - \left(T_{hw,out} - T_{s,out,STG} \right)}{ln \frac{\left(T_{hw,in} - T_{s,inside,STG} \right)}{\left(T_{hw,out} - T_{s,out,STG} \right)}} \tag{4.96}$$

where,

$$h_{hw,avg,STG} = f\left(P_{hw}, dT_{hw,avg,STG} \right) \tag{4.97}$$

$$T_{hw,avg,STG} = \frac{T_{hw,in} + T_{hw,out}}{2} \tag{4.98}$$

The outlet and inside temperature of the solution are obtained from the Eqs. 4.99 and 4.100. Then the superheated temperature of the vapour refrigerant from the special temperature generator is expressed in Eq. 4.101.

$$T_{s,out,STG} - f\left(X_{s,STG}, T_{sat,SC} \right) = 0 \tag{4.99}$$

$$T_{s,inside,STG} - f\left(X_{s,A}, T_{sat,SC} \right) = 0 \tag{4.100}$$

$$T_{sh,STG} - \left(\frac{T_{s,out,STG} + T_{s,inside,STG}}{2} \right) = 0 \tag{4.101}$$

The tube bundle and water box volume at the special temperature generator are constant. Therefore, the cooling water mass storage can be calculated by Eqs. 4.102 and 4.103.

$$M_{hw} = Vl_{hw} \rho_{hw,out} \tag{4.102}$$

$$\rho_{hw,out}=f\left(P_{hw},T_{hw,out}\right) \tag{4.103}$$

Special condenser

Assuming that there is no liquid refrigerant storage in the vessel, the inlet and outlet mass flow rate of the refrigerant are matching and the energy balance is calculated by Eq. 4.104 neglecting the mass and heat storage. At the cooling water side, mass storage is considered, thus, the energy balance is calculated as in Eq. 4.105. The logarithmic mean temperature difference at the special temperature generator is calculated by using Eq. 4.106.

$$\dot{m}_{r,out,STG}\left(h_{sh,STG}-h_{r,SC}\right)-UA_{SC}\,\Delta T_{LMTD,SC}=0 \tag{4.104}$$

$$\dot{m}_{cw}C_{p,cw,SC}\left(T_{cw,in}-T_{cw,SC}\right)+UA_{SC}\,\Delta T_{LMTD,SC} - \left(MC_{p,cw,SC}\frac{dT_{cw,avg,SC}}{dt}+\frac{dM_{cw,SC}h_{cw,avg,SC}}{dt}\right)=0 \tag{4.105}$$

$$\Delta T_{LMTD,SC}=\frac{\left(T_{sat,SC}-T_{cw,in}\right)-\left(T_{sat,SC}-T_{cw,SC}\right)}{ln\frac{\left(T_{sat,SC}-T_{cw,in}\right)}{\left(T_{sat,SC}-T_{cw,SC}\right)}} \tag{4.106}$$

where,

$$C_{p,cw,SC}=f\left(P_{cw},T_{cw,SC}\right) \tag{4.107}$$

$$h_{cw,avg,SC}=f\left(P_{cw},T_{cw,avg,SC}\right) \tag{4.108}$$

$$T_{cw,avg,SC}=\frac{T_{cw,in}+T_{cw,SC}}{2} \tag{4.109}$$

The tube bundle and water box volume at the special condenser are constant. Therefore, the cooling water mass storage can be calculated by Eqs. 4.110 and 4.111.

$$M_{cw,SC}=Vl_{cw,sc}\rho_{cw,SC} \tag{4.110}$$

$$\rho_{cw,SC}=f\left(P_{cw},T_{cw,SC}\right) \tag{4.111}$$

Mixer and separator

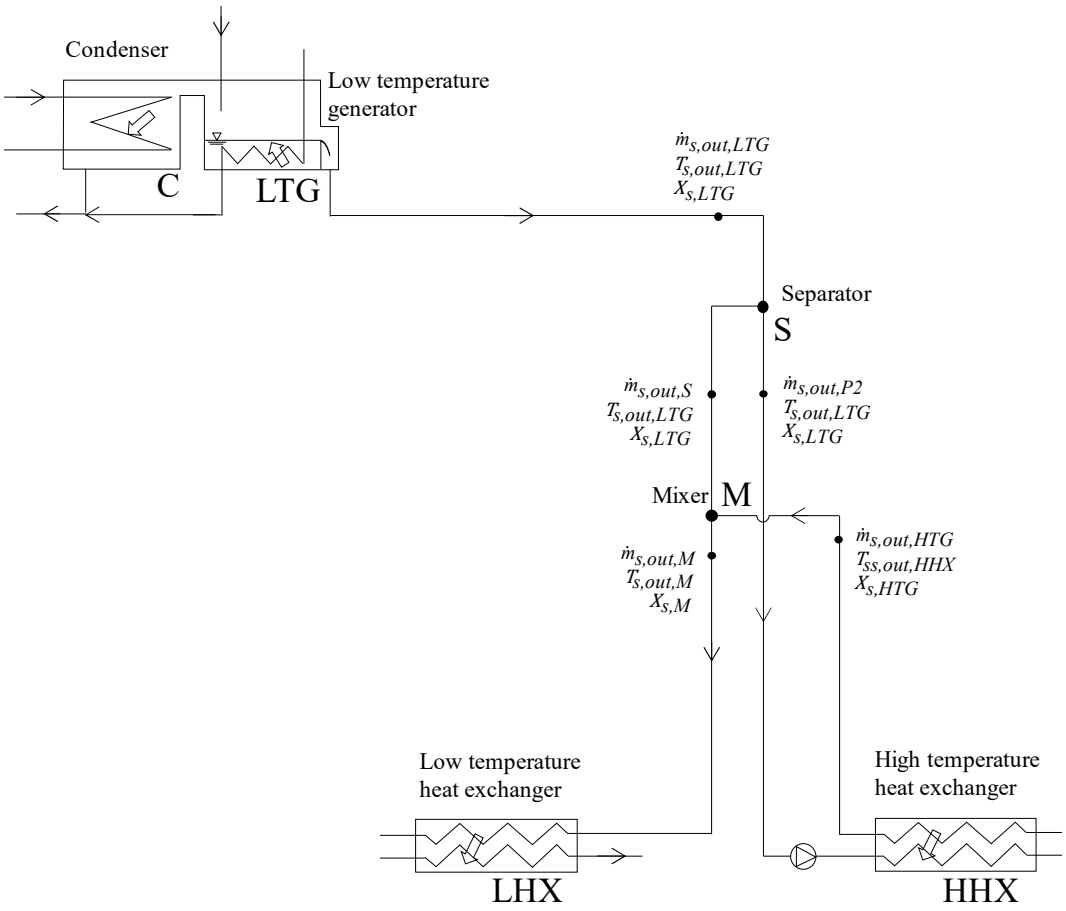

Fig. 4.6 Mixer and separator

The separator and the mixer (Fig. 4.6) are the important components to manage the mass flow rate that goes to and back from the high temperature generator. The separator is a three-way valve that actuates what is referred to as the "solution distribution ratio" γ. The adjustment of the proper distribution ratio gives the proper solution mass flow rate to the high temperature generator that is able to reduce the gas consumption, as described in chapter 5.

Separator

For the mass balance of the separator, the solution distribution ratio γ is given. In the conventional control, the solution distribution ratio is kept at 0.5. By knowing the distribution ratio value, the mass flow rate of pump 2 can be obtained. The mass balance is calculated by using Eq. 4.112. Temperature and the concentration of the solution correspond to those at the outlet of the low temperature generator and stay constant in this component.

$$\dot{m}_{s,out,LTG}+\dot{m}_{s,out,LTG}\gamma - \dot{m}_{s,out,S}=0 \quad (4.112)$$

where,

$$\dot{m}_{s,out,P2} = \dot{m}_{s,out,LTG}\gamma \quad (4.113)$$

Mixer

This mixer combines the solution from the low temperature generator and the high temperature heat exchanger. The total mass balance, LiBr mass balance, and the energy balance are calculated by using Eqs. 4.114, 4.115, and 4.116.

$$\dot{m}_{s,out,S}+\dot{m}_{s,out,HTG} - \dot{m}_{s,out,M}=0 \quad (4.114)$$

$$\dot{m}_{s,out,S}X_{s,out,LTG}+\dot{m}_{s,out,HTG}X_{s,HTG} - \dot{m}_{s,out,M}X_{s,M}=0 \quad (4.115)$$

$$\dot{m}_{s,out,S}h_{s,out,LTG}+\dot{m}_{s,out,HTG}h_{ss,out,HHX} - \dot{m}_{s,out,M}h_{s,out,M}=0 \quad (4.116)$$

where,

$$h_{ss,out,HHX}=f\left(X_{s,out,HTG}, T_{ss,out,HHX}\right) \quad (4.117)$$

High temperature generator

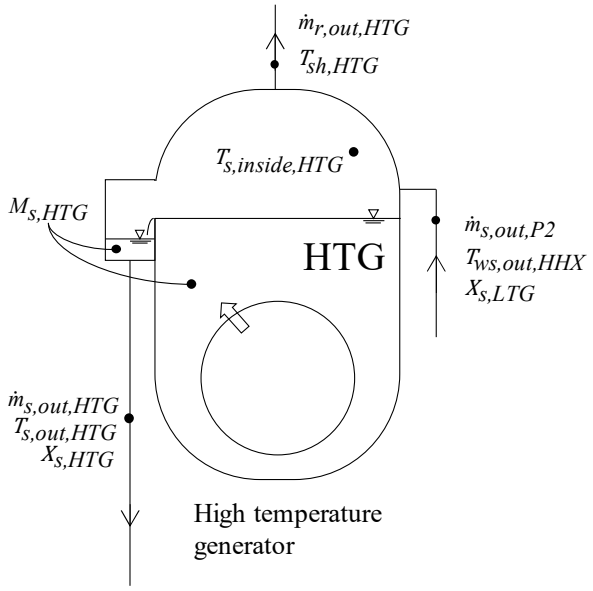

Fig. 4.7 High temperature generator

Gas as the primary energy consumption of this system heats the large solution sump in the high temperature generator (Fig. 4.7). The gas flow rate is adjusted by using the feedback of the

chilled water outlet temperature for keeping it constantly at 7 °C. The solution storage volume at the high temperature generator is assumed to be constant. The total mass balance and the LiBr mass balance are respectively calculated by Eqs. 4.118 and 4.119.

$$\dot{m}_{s,out,P2} - \dot{m}_{s,out,HTG} - \dot{m}_{r,out,HTG} - \frac{dM_{s,HTG}}{dt} = 0 \tag{4.118}$$

$$\dot{m}_{s,out,P2} X_{s,LTG} - \dot{m}_{s,out,HTG} X_{s,HTG} - \frac{dM_{s,HTG} X_{s,HTG}}{dt} = 0 \tag{4.119}$$

Since this component features a direct fire type of combustion, the overall heat transfer between the solution and the combustion is not considered. Therefore, the energy balance at the high temperature generator can be calculated directly by using the internal solution energy, the gas consumption energy (gas flow rate is multiplied by low heating value of gas), and the heat capacity storage from the vessel and the solution sump (Eq. 4.120).

$$\begin{aligned} \dot{m}_{s,out,P2} h_{ws,out,HHX} - \dot{m}_{s,out,HTG} h_{s,out,HTG} - \dot{m}_{r,out,HTG} h_{sh,HTG} - V_{gas} LHV \\ - \left(MC_{p,s,HTG} \frac{dT_{s,out,HTG}}{dt} + \frac{dM_{s,HTG} h_{s,out,HTG}}{dt} \right) = 0 \end{aligned} \tag{120}$$

where,

$$h_{ws,out,HHX} = f\left(X_{s,out,LTG}, T_{ws,out,HHX}\right) \tag{4.121}$$

$$h_{s,out,HTG} = f\left(X_{s,out,HTG}, T_{s,out,HTG}\right) \tag{4.122}$$

$$h_{sh,HTG} = f\left(P_{sat,HTG}, T_{sh,HTG}\right) \tag{4.123}$$

The outlet and inside temperature of the solution are calculated by Eqs. 4.124 and 4.125. The superheated temperature of the generated vapour refrigerant is obtained by Eq. 4.126.

$$T_{s,out,HTG} = f\left(X_{s,HTG}, T_{sat,HTG}\right) \tag{4.124}$$

$$T_{s,inside,HTG} = f\left(X_{s,LTG}, T_{sat,HTG}\right) \tag{4.125}$$

$$T_{sh,HTG} = \left(\frac{T_{s,out,HTG} + T_{s,inside,HTG}}{2} \right) \tag{4.126}$$

The small and big sumps of the solution in the high temperature generator are assumed to be constant to ease the calculation. In actual condition, the small sump solution level can be controlled by an automatic valve with the feedback from the level sensor. The total mass storage of the solution in the high temperature generator is calculated by using Eqs. 4.127 and 4.128.

$$M_{s,HTG}=Vl_{HTG}\rho_{s,out,HTG} \tag{4.127}$$

$$\rho_{s,out,HTG}=f\left(X_{s,out,HTG},T_{s,out,HTG}\right) \tag{4.128}$$

High temperature heat exchanger

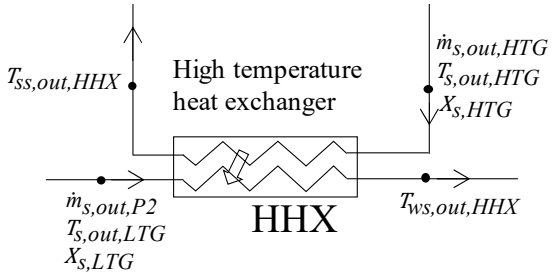

Fig. 4.8 High temperature generator

The high temperature heat exchanger schematic is represented in Fig. 4.8. The simulation model of the high temperature heat exchanger is the same, in principle, as the model of the low temperature heat exchanger. The energy balance equations for both sides are shown by Eqs. 4.129 and 4.130.

$$\dot{m}_{s,out,HTG}\left(h_{s,out,HTG}-h_{ss,out,HHX}\right)-UA_{HHX}\Delta T_{LMTD,HHX} -\left(MC_{p,ss,HHX}\frac{dT_{ss,avg,HHX}}{dt}+\frac{dM_{ss,HHX}h_{ss,avg,HHX}}{dt}\right)=0 \tag{4.129}$$

$$\dot{m}_{s,out,P2}\left(h_{s,out,LTG}-h_{ws,out,HHX}\right)+UA_{HHX}\Delta T_{LMTD,HHX} -\left(MC_{p,ws,HHX}\frac{dT_{ws,avg,HHX}}{dt}+\frac{dM_{ws,HHX}h_{ws,avg,HHX}}{dt}\right)=0 \tag{4.130}$$

where,

$$h_{ws,avg,HHX}=f\left(X_{s,out,LTG},T_{ws,avg,HHX}\right) \tag{4.131}$$

$$h_{ss,avg,HHX}=f\left(X_{s,out,HTG},T_{ss,avg,HHX}\right) \tag{4.132}$$

$$T_{ws,avg,HHX}=\frac{T_{s,out,LTG}+T_{ws,in,HHX}}{2} \tag{4.133}$$

$$T_{ss,avg,HHX} = \frac{T_{s,out,HTG} - T_{ss,out,HHX}}{2} \tag{4.134}$$

The logarithmic mean temperature difference at the low temperature heat exchanger is defined in Eq. 4.135.

$$\Delta T_{LMTD,HHX} = \frac{\left(T_{s,out,HTG} - T_{ws,out,HHX}\right) - \left(T_{ss,in,HHX} - T_{s,out,LTG}\right)}{ln\frac{\left(T_{s,out,HTG} - T_{ws,out,HHX}\right)}{\left(T_{ss,in,HHX} - T_{s,out,LTG}\right)}} \tag{4.135}$$

The strong and the weak solution storage volumes at the low temperature heat exchanger are calculated from the total volume of the tube shell. Each is assumed to have occupy half of the total volume storage (Eqs. 4.136–4.139)

$$\rho_{ws,avg,HHX} = f\left(X_{s,LTG}, T_{ws,avg,HHX}\right) \tag{4.136}$$

$$\rho_{ss,avg,HHX} = f\left(X_{s,HTG}, T_{ss,avg,HHX}\right) \tag{4.137}$$

$$M_{ws,HHX} = \frac{VI_{HHX}}{2}\rho_{ws,avg,HHX} \tag{4.138}$$

$$M_{ss,HHX} = \frac{VI_{LHX}}{2}\rho_{ss,avg,HHX} \tag{4.139}$$

4.3 Resistance ratio method

Many studies on simulation of absorption chillers present the thermal conductance values at the rated point or full load and use the same thermal conductance values for calculating the partial load condition. In the operation of recent absorption chillers, the solution flow rate changes along with the cooling capacity to maintain the partial load performance, therefore, the thermal conductance values change at the partial load. In every component of absorption chiller, two fluids exchange heat and constitute heat resistance. When the detailed information about the structure and dimension of the component is not available, by knowing the resistance ratio at the rated point, the thermal conductance value of partial load can be estimated from thermal conductance at the rated point with a power function of the parameter ratios. By using this resistance-ratio method, the partial load performance of the single-double-effect absorption chiller in any condition can be easily analysed.

4.3.1 Overall heat resistance (reciprocal of thermal conductance)

The overall heat resistance of each heat exchanger is calculated by Eq. 4.140. Where the heat transfer coefficients of internal α_1 and external α_2 are defined by the same area of the tube bundle (from inner or outer diameter).

$$\frac{1}{U} = \frac{1}{\alpha_1} + R_s + R_m + \frac{1}{\alpha_2} \tag{4.140}$$

The water flow loops (chilled water, cooling water, and hot water) of this system are a closed system, therefore there is no accumulation of fouling and scaling, then the fouling or scaling factor can be neglected.

$$R_s \fallingdotseq 0 \tag{4.141}$$

Metal resistances of the heat exchanger (absorber, evaporator, condensers, generators, and solution heat exchangers) are smaller than the overall heat resistance, hence those values can be ignored.

$$R_m \fallingdotseq 0 \tag{4.142}$$

Based on the Eqs. 4.141 and 4.142, the overall heat resistance then can be approximated by Eq. 4.143.

$$\frac{1}{U} \doteqdot \frac{1}{\alpha_1} + \frac{1}{\alpha_2} \tag{4.143}$$

4.3.2 Resistance ratio

The thermal conductance *UA* values of each component can be estimated by using the steady experimental temperature data at full load (full load test was steady), Table 2.7. The mass flow rates of solution and refrigerant are also estimated from the full load experimental data. The partial solution flow rates are affected by the control system, therefore it is difficult to decide the flow rates. The detail dimensions of the machine are not available, thus overall heat transfer coefficient *U* values cannot be separated from the thermal conductance. Also, internal and external heat transfer coefficients cannot be individually calculated because of the unknown detailed dimensions.

The thermal conductance of each element can be assumed constant for any condition. However, in this study, due to the solution mass flow rates of this system change according to the cooling capacity, the thermal conductance is then considered not constant.

In order to express the change of the partial *UA* values, the resistance ratio *RR* is newly introduced. The resistance ratio is defined at full load. Then the resistance ratio at full load is used

in order to simplify the thermal conductance calculation. The resistance ratio of the internal and external or fluid 1 and 2 are assumed to be the same for any condition. Therefore, the overall or total thermal conductance of the partial load can be known from the fixed resistance ratio of fluid 1 and 2. Where the resistance ratio is approximately equal to the heat resistance of fluid 1 or 2 over the overall heat resistance from fluid 1 and 2. The resistance ratio of the fluid 1 and 2 is expressed in the Eqs. 4.144 and 4.145 respectively.

Resistance ratio for fluid 1

$$RR_1 = \frac{\frac{1}{\alpha_{full1}}}{\frac{1}{U_{full}}} \doteqdot \frac{\frac{1}{\alpha_{full1}}}{\frac{1}{\alpha_{full1}} + \frac{1}{\alpha_{full2}}} \tag{4.144}$$

Resistance ratio for fluid 2

$$RR_2 = \frac{\frac{1}{\alpha_{full2}}}{\frac{1}{U_{full}}} \doteqdot \frac{\frac{1}{\alpha_{full2}}}{\frac{1}{\alpha_{full1}} + \frac{1}{\alpha_{full2}}} \tag{4.145}$$

According to the Eqs. 4.141 and 4.142, the total resistance ratio between fluid 1 and 2 is approximately equal to 1 (Eq. 4.146).

$$RR_1 + RR_2 \doteqdot 1 \tag{4.146}$$

As known, heat transfer area A is constant. Therefore, in general, the resistance ratio can be expressed as follows:

$$RR = \frac{U_{full}}{\alpha_{full}} = \frac{U_{full}\, A}{\alpha_{full}\, A} \tag{4.147}$$

In this case, especially for calculating the thermal conductance at partial load, the change of the physical properties of fluids (solution, refrigerant, and water) is not considered. Therefore, the heat transfer coefficient is strongly influenced by the volumetric flow rate, which Reynold number trend is proportional to the volumetric flow rate trend. Under the above specific assumption, the heat transfer coefficient is proportional to Reynold number with power function and also can be proportional to volumetric flow rate with power function (Eq. 4.148).

$$\alpha \propto Re^m \propto V^m \tag{4.148}$$

The heat transfer coefficient can be calculated by using direct proportion to Eq. 4.148.

$$\frac{\alpha_{full}}{V_{full}^m} = \frac{\alpha}{V^m} \tag{4.149}$$

From Eq. 4.149, the heat resistance can then be rearranged as Eq. 4.150.

$$\frac{1}{\alpha} = \left(\frac{1}{\alpha_{full}}\right)\left(\frac{V_{full}}{V}\right)^{m} \tag{4.150}$$

Substituting Eq. 4.147 to the heat resistance at full load $1/\alpha_{full}$, then the heat resistance for the partial load can be expressed as Eq. 4.151.

$$\frac{1}{\alpha} = \left(\frac{RR}{U_{full}}\right)\left(\frac{V_{full}}{V}\right)^{m} \tag{4.151}$$

As known, overall heat resistance is the combination from the heat resistance of the internal and external fluid (Eq. 4.143). Then, by combining Eq. 4.143 and Eq. 4.151, the general equation of the thermal conductance for the partial load can be calculated by using resistance ratio and power function of internal and external side (Eq. 4.152).

$$\frac{1}{UA} = \left(\frac{RR_1}{UA_{full}}\right)\left(\frac{V_{full1}}{V_1}\right)^{m_1} + \left(\frac{RR_2}{UA_{full}}\right)\left(\frac{V_{full2}}{V_2}\right)^{m_2} \tag{4.152}$$

The detail information of initial, constant, and assumption values for calculating the dynamic condition can be seen in Appendix 1.

The bold text (Table 4.1) identifies the main variable which affects heat transfer rates in the component.

Table 4.1 the main variables

Component	Variables		Simulation given condition
	Fluid 1 (internal)	Fluid 2 (external)	
Absorber	Solution **Flow rate** Temperature Concentration	Cooling water **Flow rate** Temperature	Cooling water flow rate is constant
Evaporator	Refrigerant **Flow rate** Temperature	Chilled water **Flow rate** Temperature	Chilled water flow rate is constant
Special Condenser	Refrigerant **Heat flux (flow rate)** Temperature	Cooling water **Flow rate** Temperature	Cooling water flow rate is constant
Condenser	Refrigerant **Heat flux (flow rate)** Temperature	Cooling water **Flow rate** Temperature	Cooling water flow rate is constant
Special Temperature Generator	Solution **Flow rate** Temperature Concentration	Hot water **Flow rate** Temperature	Hot water flow rate is constant
Low Temperature Generator	Solution **Heat flux** Temperature Concentration	Refrigerant vapour **Heat flux (flow rate)** Temperature/pressure	
Solution Heat Exchanger	Solution **Flow rate** Temperature Concentration	Solution **Flow rate** Temperature Concentration	

Further, the overall thermal conductance of each component is explained in detail based on the above general explanation.

Absorber

According to the method described in the previous section, the heat transfer coefficient values both solution (internal) and cooling water (external) side are strongly affected by the volumetric flow rate. Therefore, the trend of heat transfer coefficient is assumed proportional to the trend of Reynolds number with a power function of parameter ratio. The power function of parameter ratio for the solution side is obtained from Furukawa Sasaki and Kaneko Noseki (1993) [55].

1: Solution; 2: Cooling water; V: Volumetric flow rate; Re: Reynolds number

Solution

$$\alpha_1 \propto Re_1^{m_1} \propto V_1^{m_1} \tag{4.153}$$

$$\frac{1}{\alpha_1} = \left(\frac{1}{\alpha_{full1}}\right)\left(\frac{V_{full1}}{V_1}\right)^{m_1} = \left(\frac{RR_1}{U_{full}}\right)\left(\frac{V_{full1}}{V_1}\right)^{m_1} \tag{4.154}$$

where $m_1 = 0.25$; $RR_1 = 0.84$.

Cooling water

$$\alpha_2 \propto Re_2^{m_2} \propto V_2^{m_2} \tag{4.155}$$

$$\frac{1}{\alpha_2} = \left(\frac{1}{\alpha_{full2}}\right)\left(\frac{V_{full2}}{V_2}\right)^{m_2} = \left(\frac{RR_2}{U_{full}}\right)\left(\frac{V_{full2}}{V_2}\right)^{m_2} \tag{4.156}$$

where $m_2 = 0.25$; $RR_2 = 0.16$.

The cooling water flow rate is kept constant. Therefore, the heat resistance of the cooling water side can be assumed constant.

$$V_2 = V_{full2} = constant \rightarrow \frac{1}{\alpha_2} = \frac{RR_2}{U_{full}} = \frac{1\text{-}RR_1}{U_{full}} \tag{4.157}$$

The overall thermal conductance of the absorber for partial load (Eq. 4.158) is calculated by combining Eq. 4.154 and Eq. 4.156.

$$\frac{1}{UA} = \left(\frac{0.84}{UA_{full}}\right)\left(\frac{V_{full1}}{V_1}\right)^{0.25} + \left(\frac{0.16}{UA_{full}}\right) \tag{4.158}$$

Evaporator

This system uses a falling film type evaporator. The refrigerant is sprayed with constant flow rate. Where the chilled water flow rate inside the tube bundle is kept constant. Takahasi Saeki (2004) has analysed the heat transfer coefficient against the flow rate and the heat transfer coefficient of refrigerant is not much influenced by the volumetric flow rate [56]. Therefore, the heat transfer coefficient of refrigerant is approximately equal constant. In other words, the overall thermal conductance of evaporator can be assumed constant.

1: Refrigerant; 2: Chilled water; V: Volumetric flow rate; Re: Reynolds number

Refrigerant

$$\alpha_1 \doteqdot constant \tag{4.159}$$

where $m_1 = 0$; $RR_1 = 0.50$.

Chilled water

$$\alpha_2 \propto Re_2^{m_2} \propto V_2^{m_2} \tag{4.160}$$

$$\frac{1}{\alpha_2} = \left(\frac{1}{\alpha_{full2}}\right)\left(\frac{V_{full2}}{V_2}\right)^{m_2} = \left(\frac{RR_2}{U_{full}}\right)\left(\frac{V_{full2}}{V_2}\right)^{m_2} \tag{4.161}$$

$$V_2 = V_{full2} = constant \tag{4.162}$$

where $m_2 = 0.8$; $RR_2 = 0.50$.

According to the constant heat transfer coefficient of the refrigerant and chilled water. Therefore, the overall thermal conductance of the evaporator can be assumed constant for the partial load.

$$\frac{1}{UA} = \frac{1}{UA_{full}} = constant \tag{4.163}$$

Condenser

Based on the experimental result from Fujii Oda (1982) [57], the heat transfer coefficient of refrigerant is not strongly influenced by the flow rate. Thus, in this study, the heat transfer coefficient can be assumed constant even though the flow rate changes. The constant of the cooling water flow rate makes the heat transfer coefficient of cooling water can be approximately constant. Therefore, the thermal conductance of the condenser is assumed constant.

1: Refrigerant; 2: Cooling water; V: Volumetric flow rate; Re: Reynolds number

Refrigerant

$$\alpha_1 \doteqdot constant \tag{4.164}$$

where $m_1 = 0$; $RR_1 = 0.50$.

Cooling water

$$\alpha_2 \propto Re_2^{m_2} \propto V_2^{m_2} \tag{4.165}$$

$$\frac{1}{\alpha_2} = \left(\frac{1}{\alpha_{full2}}\right)\left(\frac{V_{full2}}{V_2}\right)^{m_2} = \left(\frac{RR_2}{K_{full}}\right)\left(\frac{V_{full2}}{V_2}\right)^{m_2} \tag{4.166}$$

$$V_2 = V_{full2} = constant \tag{4.167}$$

where $m_2 = 0.8$; $RR_2 = 0.50$.

Based on the explanation of Eqs. 4.164 to 4.167, then the overall thermal conductance of the condenser is assumed to be constant for the partial load (Eq. 4.168).

$$\frac{1}{UA} = \frac{1}{UA_{full}} = constant \tag{4.168}$$

Special condenser

The special condenser and condenser have the same situation. Therefore, the overall thermal conductance of the special condenser is assumed constant according to the explanation of the condenser.

$$\frac{1}{UA} = \frac{1}{UA_{full}} = constant \tag{4.169}$$

Special temperature generator

A falling film type heat exchanger is used in the special temperature generator. The solution flow rate changes according to the cooling capacity and the hot water flow rate is constant. Therefore, the overall thermal conductance for the partial load is strongly influenced by the solution flow rate. The power function of the parameter ratio is conducted from the experimental results of Nishiyama et al. (1974) [58].

1: Solution; 2: Hot water; V: Volumetric flow rate; Re: Reynolds number

Solution

$$\alpha_1 \propto Re_1^{m_1} \propto V_1^{m_1} \tag{4.170}$$

$$\frac{1}{\alpha_1} = \left(\frac{1}{\alpha_{full1}}\right)\left(\frac{V_{full1}}{V_1}\right)^{m_1} = \left(\frac{RR_1}{U_{full}}\right)\left(\frac{V_{full1}}{V_1}\right)^{m_1} \tag{4.171}$$

where $m_1 = 0.36$; $RR_1 = 0.84$.
Hot water

$$\alpha_2 \propto Re_2^{m_2} \propto V_2^{m_2} \tag{4.172}$$

$$\frac{1}{\alpha_2} = \left(\frac{1}{\alpha_{full2}}\right)\left(\frac{V_{full2}}{V_2}\right)^{m_2} = \left(\frac{RR_2}{U_{full}}\right)\left(\frac{V_{full2}}{V_2}\right)^{m_2} \tag{4.173}$$

where $m_2 = 0.8$; $RR_2 = 0.16$.

At the single-double-effect mode, the hot water flow rate is constant. Therefore, the heat resistance of the hot water side can be assumed to be constant. In the other word, the heat resistance of the hot water is also constant. In addition, the hot water flow rate is changeable to control the chilled water outlet temperature at the single-effect mode.

$$V_2 = V_{full2} = constant \rightarrow \frac{1}{\alpha_2} = \frac{RR_2}{U_{full}} = \frac{1\text{-}RR_1}{U_{full}} \tag{4.174}$$

The overall thermal conductance of the special temperature generator (4.175) is then calculated by combining Eq. 4.173 and Eq. 4.174.

$$\frac{1}{UA} = \left(\frac{0.8}{UA_{full}}\right)\left(\frac{V_{full1}}{V_1}\right)^{0.36} + \left(\frac{0.16}{UA_{full}}\right) \tag{4.175}$$

Low temperature generator

The low temperature generator is different from the other two generators. This heat exchanger features a pool boiling configuration: outside of the tube bundle is the sump of the solution, inside of the tube is refrigerant vapour. Both the solution and refrigerant flow rates change according to the required cooling capacity. Therefore, the trend of thermal conductance is assumed to be the same with the trend of heat flux or heat capacity rate from solution and refrigerant. For calculating the thermal conductance of the low temperature generator the power function of parameter ratio from the combination of solution and refrigerant is calculated according to the study of Kajii et al. (2011) [59], Travis et al. (1971) [60], Ueda et al. (1977) [61], and Fuji et al. (1980) [62].

1: Solution; 2: refrigerant vapour; q: heat flux (q1=q2=q); Q=q·A (Q1= Q2=Q)

Solution

$$\alpha_1 \propto q^{m_1} \propto Q^{m_1} \tag{4.176}$$

$$\frac{1}{\alpha_1} = \left(\frac{1}{\alpha_{full1}}\right)\left(\frac{Q_{full1}}{Q_1}\right)^{m_1} = \left(\frac{RR_1}{U_{full}}\right)\left(\frac{Q_{full1}}{Q_1}\right)^{m_1} \tag{4.177}$$

Refrigerant vapour

$$\alpha_2 \propto q^{m_2} \propto Q^{m_2} \tag{4.178}$$

$$\frac{1}{\alpha_2} = \left(\frac{1}{\alpha_{full2}}\right)\left(\frac{Q_{full2}}{Q_2}\right)^{m_2} = \left(\frac{RR_2}{U_{full}}\right)\left(\frac{Q_{full2}}{Q_2}\right)^{m_2} \tag{4.179}$$

After combining the heat capacity of the solution and the refrigerant vapour, the overall thermal conductance of the low temperature generator is calculated by using Eq. 4.180.

$$\frac{1}{UA} \doteqdot \left(\frac{1}{UA_{full}}\right)\left(\frac{Q_{full}}{Q}\right)^{n} \tag{4.180}$$

Where n=0.68.

Solution heat exchangers

There are two solution heat exchangers installed in this system. In these heat exchangers, the strong solution exchanges heat to the weak solution. Both solution flow rates change according to the required cooling capacity. The power function of the parameter ratio is referred from Okada et al. (1971) [63] and Zahid Ayub (2003) [64].

1: Solution (strong); 2: Solution (weak); V: Volumetric flow rate; Re: Reynolds number

Solution

$$\alpha_1 \propto Re_1^{m_1} \propto V_1^{m_1} \tag{4.181}$$

$$\frac{1}{\alpha_1} = \left(\frac{1}{\alpha_{full1}}\right)\left(\frac{V_{full1}}{V_1}\right)^{m_1} = \left(\frac{RR_1}{K_{full}}\right)\left(\frac{V_{full1}}{V_1}\right)^{m_1} \tag{4.182}$$

Cooling water

$$\alpha_2 \propto Re_2^{m_2} \propto V_2^{m_2} \tag{4.183}$$

$$\frac{1}{\alpha_2} = \left(\frac{1}{\alpha_{full2}}\right)\left(\frac{V_{full2}}{V_2}\right)^{m_2} = \left(\frac{RR_2}{K_{full}}\right)\left(\frac{V_{full2}}{V_2}\right)^{m_2} \tag{4.184}$$

m1=m2=m = 0.65

$$\frac{V_{full1}}{V_1} \doteqdot \frac{V_{full2}}{V_2} \tag{4.185}$$

$$\frac{1}{UA} = \left(\frac{RR_1}{UA_{full}}\right)\left(\frac{V_{full1}}{V_1}\right)^{m_1} + \left(\frac{RR_2}{UA_{full}}\right)\left(\frac{V_{full2}}{V_2}\right)^{m_2} = \left(\frac{1}{UA_{full}}\right)\left(\frac{V_{full}}{V}\right)^{m} \tag{4.186}$$

4.4 Validation

4.4.1 Steady state model validation

The experimental data were collected for two different hot water inlet temperatures, namely 75 °C and 90 °C, as a function of the cooling capacity (100% of cooling capacity until the minimum is reached). This model was then validated with the experimental data [65]. The validation data are the fuel gas consumption (expressed in nominal cubic meter per hour, per tons of refrigeration, nm^3/hRT) in Fig. 4.9 and solar energy utilisation (kW/RT) in Fig. 4.10.

Continuous lines in Fig. 4.9(a) and Fig. 4.10(a) represent the simulation results, while the markers represent the experimental results. The simulation results were obtained by adjusting the mass flow rate from the solution pumps, based on the experimental results. Hence, from this calculation, the table with data necessary to control the flow rate of the solution pumps was also obtained. Besides that, the relative errors on the evaluation of the gas consumption and solar energy utilisation are shown in Fig. 4.9(b) and Fig. 4.10(b). Qualitative and quantitative agreement of simulation and experiments can be observed in these figures, showing the model ability to accurately predict gas consumption and solar energy utilization when hot water temperature and cooling capacity are used as parameters.

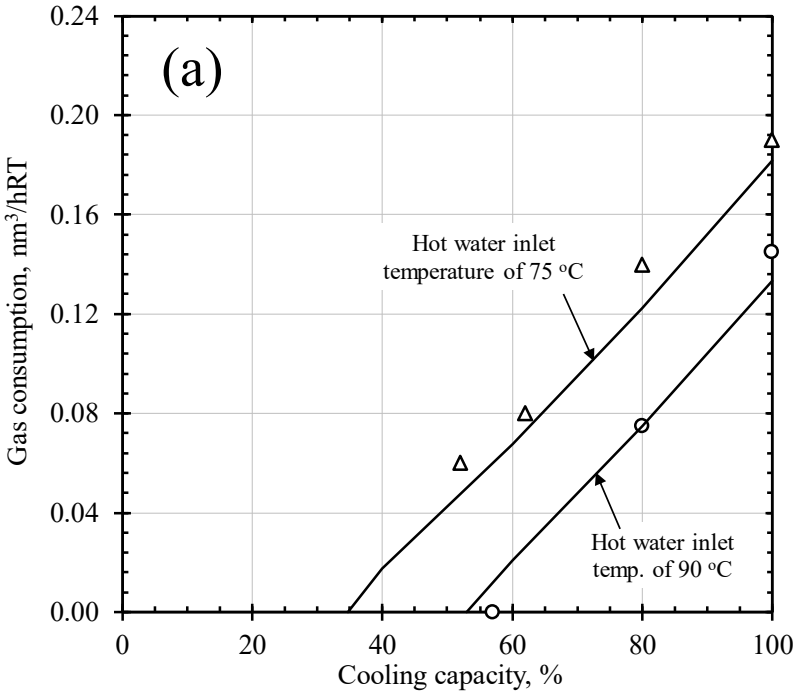

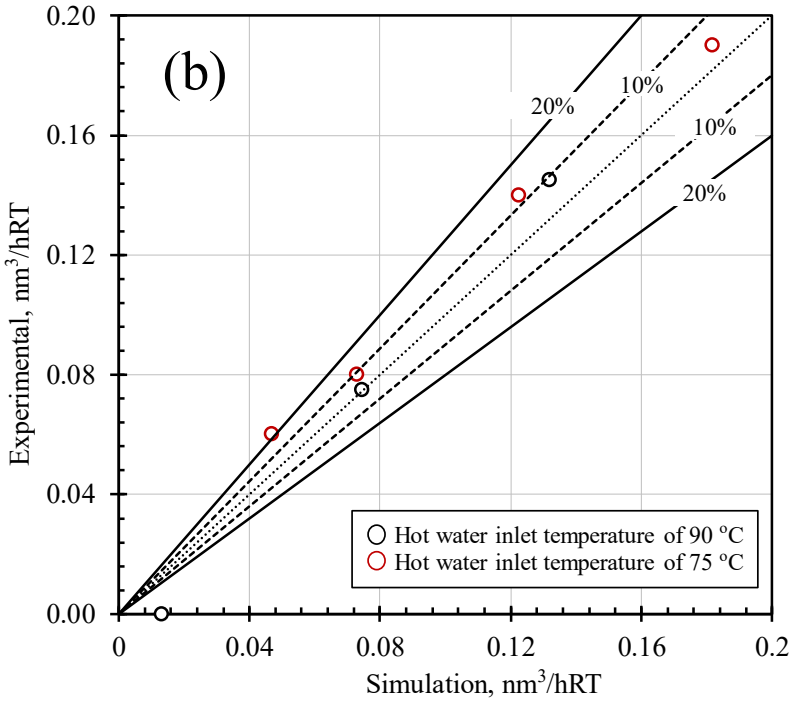

Fig. 4.9 (a) Trend of the gas consumption between simulation and experimental [65], (b) relative error (percentage) of gas consumption from the simulation results. Solid line: 20% error; dotted line: 10%

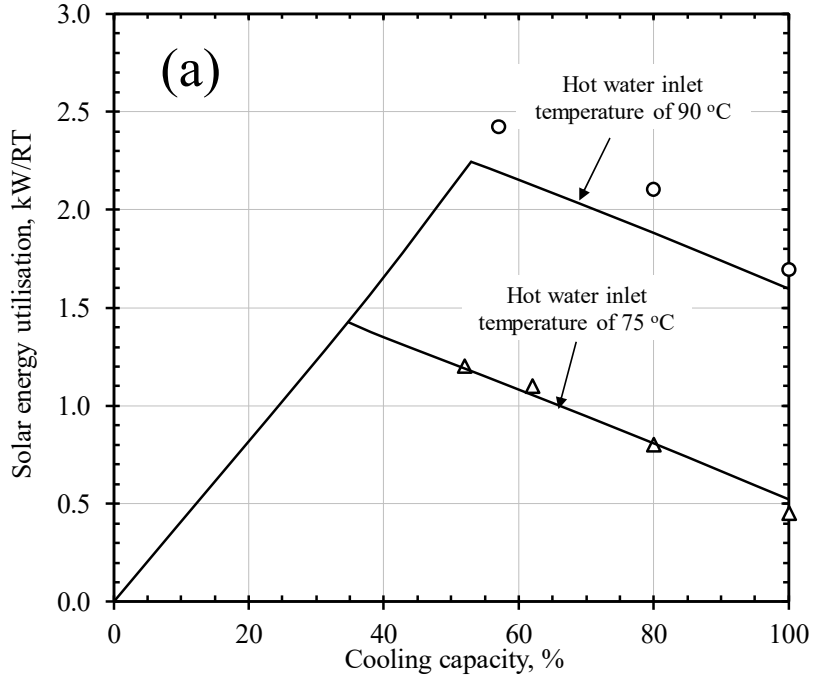

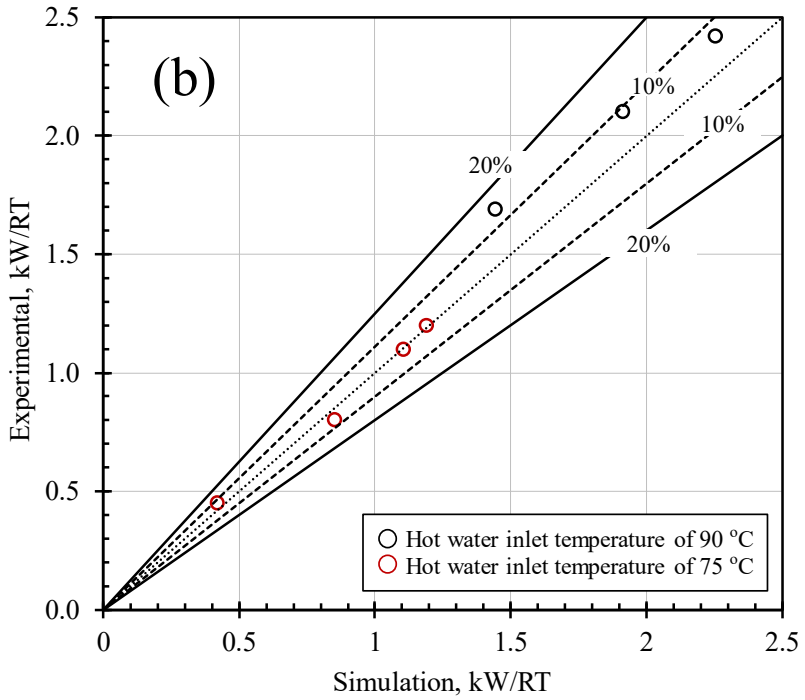

Fig. 4.10 (a) Trend of the solar energy utilisation between simulation and experimental [65], (b) relative error (percentage) of solar energy utilisation from the simulation results. Solid line: 20% error; dotted line: 10% error

4.4.2 Dynamic model validation

The dynamic model is validated by using the field test results in Indonesia. In the field test data, the absorption chiller machine does not include the internal mass flow meter and pressure sensors, therefore the external parameters such as hot, cooling, and chilled water temperature are then used to validate the simulation results.

The field test result on September 22nd, 2014 is taken as a typical case and used to validate the dynamic model. The detailed explanation of this typical data is discussed in chapter 3.

For the dynamic simulation, the data from 11:16 to 12:22 are selected (around 4000 s). The outlet temperatures of hot, cooling, and chilled water are used to compare the simulation results. In the dynamic simulation, the inlet temperatures of hot, cooling, and chilled water, gas volumetric flow rate, solution volumetric flow rate, and distribution ratio are used according to the assumption and the field test data. The simulation time step is 1 second according to the field test data.

In the real application, the total solution volumetric flow rate (solution pump 1) is adjusted according to the cooling capacity (Fig. 4.11), and the distribution ratio (solution pump 2) is kept constant at 0.5. While the gas volumetric flow rate maintains the chilled water outlet temperature

at approximately 7 °C. During the dynamic simulation, the total solution volumetric flow rate is assumed to be constant 51.3 l/min because the whole cooling capacity of the field test result on September 22nd, 2014 is almost lower than 55%. The solution distribution ratio is assumed according to the designed value of 0.5. Meanwhile, the gas volumetric flow rate of the dynamic simulation is controlled based on the field test data.

The calculation results of the outlet hot, cooling, and chilled water temperatures are depicted in Figs. 7.4 to 7.6, where they are compared to the experimental results. From these figures, the agreement between the simulation results and the field test results can be verified. Specifically, the absolute error in the temperature estimation of the simulation results with respect to the field test stays between 0.3 and 1.1 °C; where the biggest error occurs in the hot water outlet temperature (Fig. 4.12) and the condenser cooling water outlet temperature (Fig. 4.13(b)).

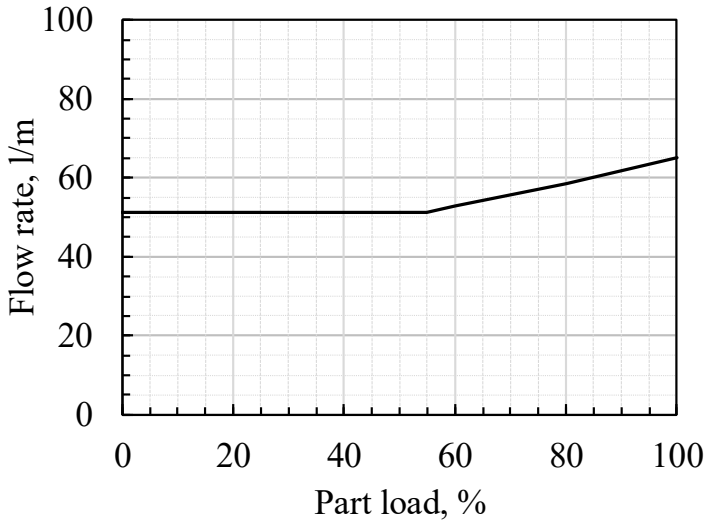

Fig. 4.11 Volumetric flow rate of the solution pump 1 according to cooling capacity percentage

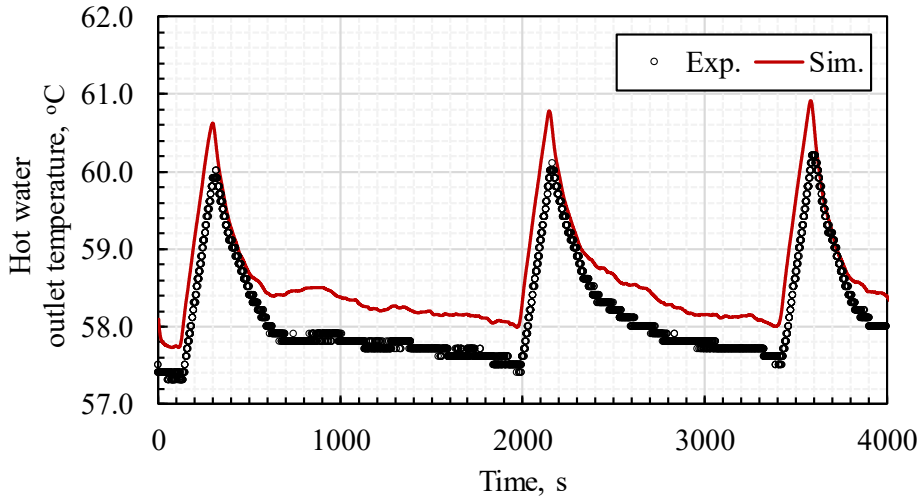

Fig. 4.12 Comparison of simulated and field test of the hot water outlet temperature

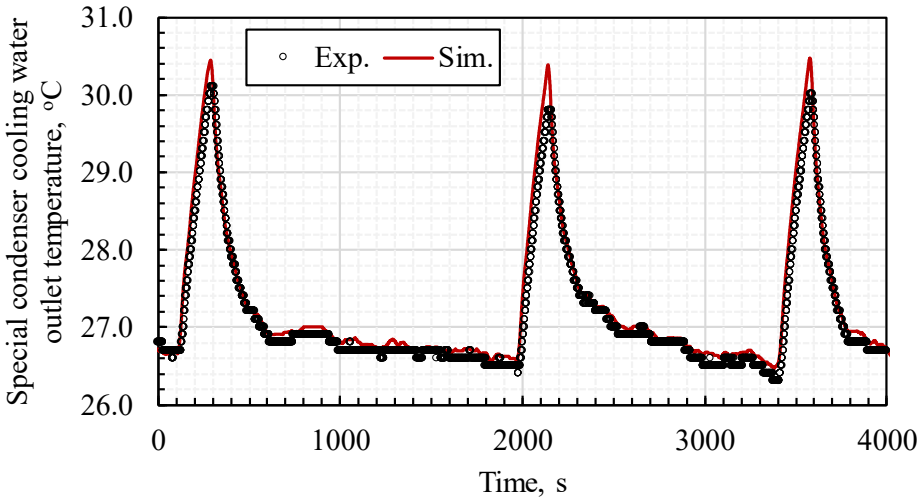

(a). Special condenser

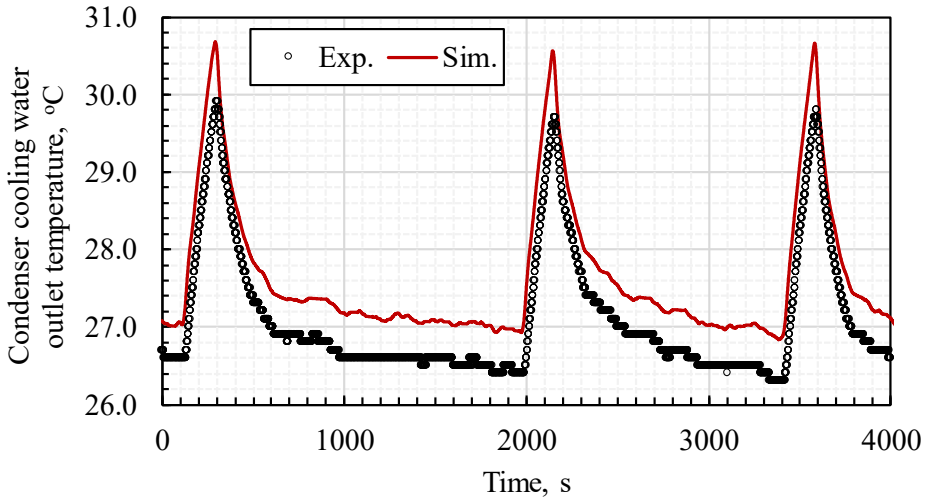

(b). Condenser

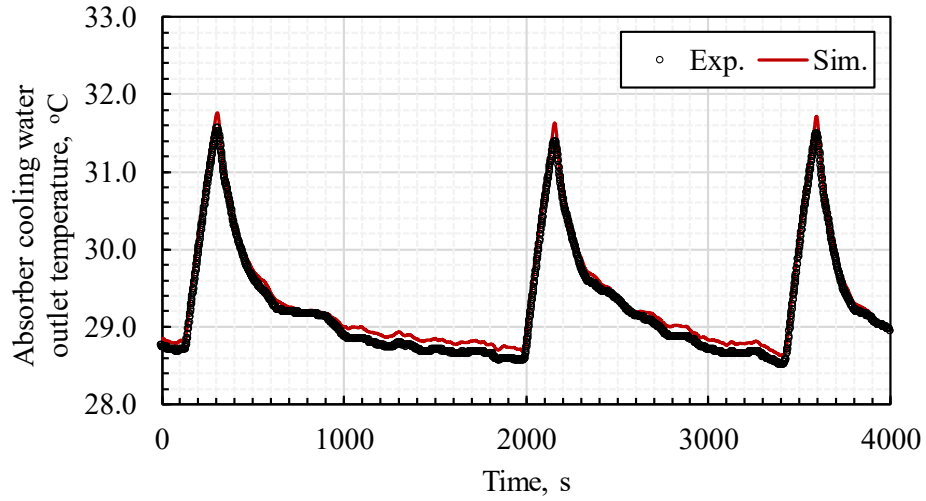

(c). Absorber

Fig. 4.13 Comparison of simulated and field test of the cooling water temperature at the outlet of (a). Special condenser, (b). Condenser, and (c). Absorber.

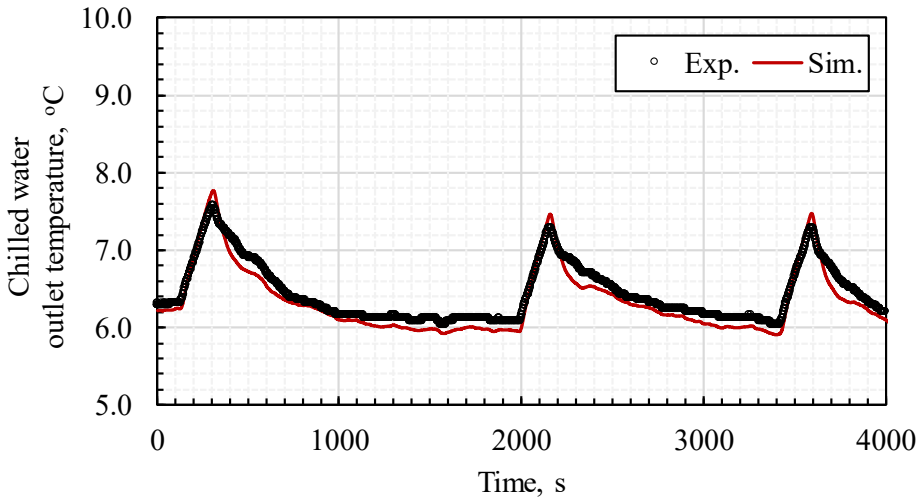

Fig. 4.14 Comparison of simulated and field test of the chilled water outlet temperature

Chapter 5
Basic Performance and Characteristics

Solar energy is a renewable source that can solve energy problems worldwide [66]. There are several reasons for use of renewable energy sources and for directing research efforts towards energy problems. Foremost, non-renewable energy sources are limited and steeply diminishing due to the increasing energy demands. Additionally, non-renewable sources are typically associated with environmental problems. Some tropical Asian countries are geographically aligned with the equator, and their locations are thus beneficial for the abundant availability of solar energy throughout the year.

Absorption chillers are driven by heat from an electrical heater, gas flaring, waste heat from engines, and other sources. Since the input heat needed for the single-effect absorption cycle is not required to have a high-temperature level, a system was conceived for use of heat from solar energy.

A collector area with a large size is required to fulfill a large capacity for hot water. The required hot water capacity depends on the nominal cooling capacity of the absorption chiller. For instance, a lithium bromide-water double-stage absorption chiller machine installed in Tunisia with a 16 kW cooling capacity needed a parabolic, trough solar collector area of 39 m^2 [67]. Based on another experiment in Reunion Island, a lithium bromide-water, single-effect absorption chiller possesses a 30 kW cooling capacity, and used a double-glazed flat plate solar collector with a total area of 90 m^2 [68]. Furthermore, in Seville (Spain), a double-effect absorption chiller with a 174 kW cooling capacity featured a linear Fresnel solar collector with a total aperture area of 352 m^2 [69]. Even though the cooling capacity and the solar collector area cannot be directly compared, these application cases can be used as references. In general, a higher cooling capacity requires a larger solar collector area.

Absorption chillers installed on buildings that have a large cooling load and limited exposed areas, cannot use only solar energy to fulfill the total cooling load due to the lack of available solar collector areas, and due to fact that the operative performance of the solar collector is highly dependent on the availability and intensity of solar radiation. The amount of solar radiation which can be absorbed is, in turn, greatly affected by weather conditions. Due to the occasional changes of the weather conditions, this type of absorption system requires a reserve of energy that can stabilise the system operability and match the user demand continuously. Among the conventional energy sources, natural gas is more environment-friendly and relatively cheaper than other fossil fuel. Therefore, natural gas is suitable to be combined with solar energy. The development of the single-double-effect absorption chiller, which uses a combination of solar energy and natural gas, is described in [70) 71)].

The COP of this system is calculated as the cooling capacity divided by the natural gas consumption. Therefore, the use of solar energy is always beneficial for the system operability. It

will be demonstrated by the analysis that follows that the single-double-effect absorption chiller is a suitable system for areas that are characterised by a high amount of available solar energy. Therefore, this system is mostly appropriate when used in the tropical regions, and the investment cost required is expected to be recovered in a short payback period. At first, the purpose of this study is to characterise the performance of the single-double-effect absorption chiller with variations in the cooling water inlet temperatures and the hot water inlet temperature from solar energy using simulations. This analysis will provide the basis for future optimisation efforts of the system and improve its operation methodology. Correspondingly, the elicited results confirm that solar energy can be fully utilised in a single-double-effect absorption chiller in tropical climates.

5.1 Performance analysis

The detailed mathematical model is explained in chapter 4. The fundamental heat and mass transfer processes are based on the mass and energy balance equations.

To calculate the COP, Eq. 5.1 is used, where the cooling capacity Q_E is divided by the fuel gas consumption Q_{HTG}. In this case, the solar energy is ignored because it can be freely obtained from nature.

$$COP = \frac{Q_E}{Q_{HTG}} \tag{5.1}$$

The gas reduction ratio (GRR) is used to evaluate how much the gas energy saving of the system is when utilising solar energy. To calculate the GRR value, Eq. (5.2) is used.

$$\text{GRR} = \left(1 - \frac{Q_{HTG,SDE}}{Q_{HTG,DE}}\right) \times 100\% \tag{5.2}$$

where, $Q_{HTG,SDE}$ is the fuel gas consumption when the system is utilising solar energy, and $Q_{HTG,DE}$ represents the fuel consumption of an equivalent system that does not use solar energy (but uses only gas).

The percentage in charge of the solar energy and gas in the entire cooling capacity is calculated using the comparison of refrigerant from the generator (STG, LTG and HTG). The percentage is calculated using Eqs. (5.3) and (5.4) as follows:

$$PQ_{E,solar\ energy} = \left(\frac{\dot{m}_{r,out,STG}}{\dot{m}_{r,out,M2}}\right) \times 100\% \tag{5.3}$$

$$PQ_{E,gas} = \left(\frac{\dot{m}_{r,out,HTG} + \dot{m}_{r,out,LTG}}{\dot{m}_{r,out,M2}} \right) \times 100\% \quad (5.4)$$

The lithium bromide-water properties are based on the 2013 ASHRAE Handbook-Fundamentals (SI).

5.2 Simulation condition

The simulation model adopted and validated with experimental data was used to investigate the performance of the system in a wider range of conditions. Simulations were carried out considering the assumptions in chapter 4.

The maximum cooling load of the mechanical research center building is 239 kW. Hence, the cooling capacity is adjusted to the same value of the cooling load. Simulation conditions used as a reference in this study can be seen in Table 5.1. The value entries in this table are quoted from the specifications of the real absorption machine.

Table 5.1 Simulation conditions

	Value	Unit
Cooling capacity	239	kW
Chilled water inlet temp.	15	°C
Chilled water outlet temp.	7	°C
Chilled water flow rate	25.7	m^3/h
Cooling water inlet temp.	28–34	°C
Cooling water flow rate	68	m^3/h
Hot water inlet temp.	75–90	°C
Hot water flow rate	7.8	m^3/h

5.3 Results and discussion

In general, the calculations are carried out to identify the effects of the cooling and hot water temperatures (solar energy) on the performance of this system. The evaluations used in this study, include the coefficient of performance, gas reduction ratio, the minimum hot water temperature, the energy input composition, and the ratio of cooling capacity charged by the solar energy and gas. These results are directed towards installations in tropical Asia regions, and specifically in Indonesia which was selected as a field test.

5.3.1 Performance (COP)

The performance of this system is affected by internal and external factors, namely, the cooling water inlet temperature, solar energy (hot water temperature), the control system, etc. The control system plays a major role for establishing a dynamic condition necessary to maintain a

good system performance. However, in this study more focus is placed on external factors, namely the tropical climate.

Fig. 5.1 explains the performance of the single-double-effect absorption chiller at various conditions of cooling and hot water inlet temperatures. The cooling water inlet temperatures (28–34 °C) and the hot water temperatures (75–90 °C) are chosen according to the tropical conditions. In general, the performance of this system increases when the hot water inlet temperature increases. Another tendency of this system is that for the same hot water inlet temperature, a higher COP was obtained at the lower cooling water inlet temperature. For example, with hot water at 90 °C, and cooling water at 34 °C, the system has a COP of 1.85. A highest COP value equal to 2.91 can be reached with 28 °C of the cooling water inlet temperature and 90 °C of the hot water inlet temperature, which maximises the desorption capacity of the STG at fixed cooling capacity in the operative range under analysis. In general, for a given cooling water temperature, higher inlet hot water temperatures increase the vapour desorption capacity of the STG by moving the solution equilibrium concentration to higher values; this leads to lower gas consumption and higher system COP. The COP of this system is anywise higher than a conventional double-effect absorption chiller, even when the hot water inlet temperature is as low as 75 °C, and the highest cooling water inlet temperature was 34 °C, compared to the COP of a conventional double-effect absorption chiller of 1.35 [65].

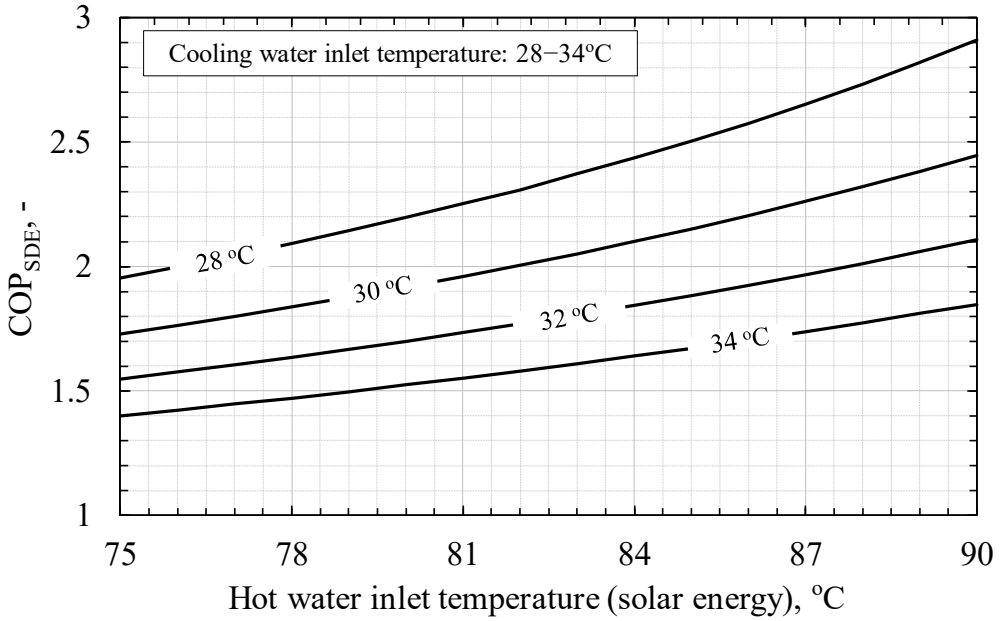

Fig. 5.1 COP of single-double-effect absorption chiller

This system has a higher COP than the conventional double-effect absorption chiller because the COP is obtained by the cooling capacity divided by the gas consumption [in accordance to Eq. 5.1], even though this system also uses solar energy. Solar energy was ignored because it is available from nature at no cost.

Fig. 5.2 describes in more details how the COP for a cooling water inlet temperature of 32 °C increases significantly since higher hot-water inlet temperatures, reduce the gas consumption at a constant cooling load.

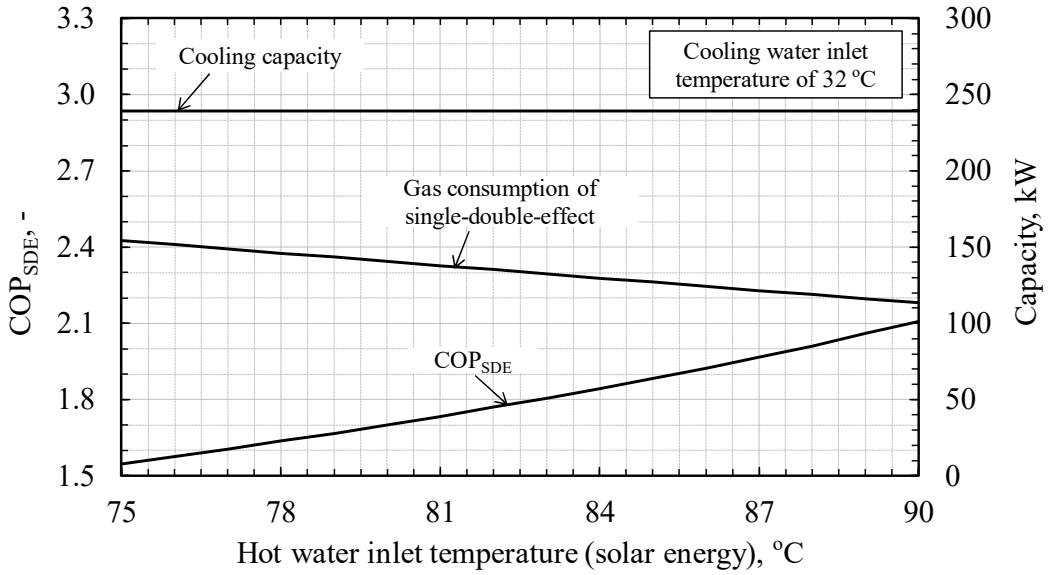

Fig. 5.2 COP of single-double-effect absorption chiller at a cooling water inlet temperature of 32°C

5.3.2 Gas reduction ratio (GRR)

Energy savings can be achieved by increasing the energy efficiency, which is the basis of engineering works, and specifically achievement of a reduction of energy consumption for a given output objective. In this case, the reduction of gas consumption is due to the effective use of solar energy, which can be obtained from nature without any additional fuel cost and environmental damage. In this study, the energy saving is evaluated by the definition of the gas reduction ratio (GRR) defined in Eq. 5.2. This parameter is related to the enhancement of the utilisation of solar energy, but most importantly, it expresses quantitatively, both in terms of energy consumption and operative cost, the advantage of this system with respect to the corresponding conventional system. When the hot water temperature increases, the GRR value also increases, and this is observed in Fig. 5.3. The enhancement of the GRR value is not only affected by the temperature of the hot water but also by the cooling water inlet temperature. The cooling water inlet temperature influences the performance of this system as well as that of the conventional double-effect absorption chiller. Thus, an increasing GRR value shows how the benefit of a higher inlet, hot water temperature or a lower inlet cooling water temperature related to the single-double effect system is increased. At a constant hot water inlet temperature of 90 °C and a cooling water inlet temperature of 34 °C, the system yields to a GRR value of 28%. The GRR value increases to 50.9% when the cooling water inlet temperature is 28 °C. At the most demanding condition in terms of energy consumption, namely, at a low hot water inlet temperature (75 °C) and a high

cooling water inlet temperature (34 °C), this system is still capable to elicit an energy saving with a GRR value of 5%.

The direct effect of a positive GRR is the corresponding reduction of CO_2 emissions. From this standpoint, a decision to adopt this system in tropical regions to maximise the utilisation of solar energy can be justified by results that are globally salutary in addressing global warming and environmental issues in general.

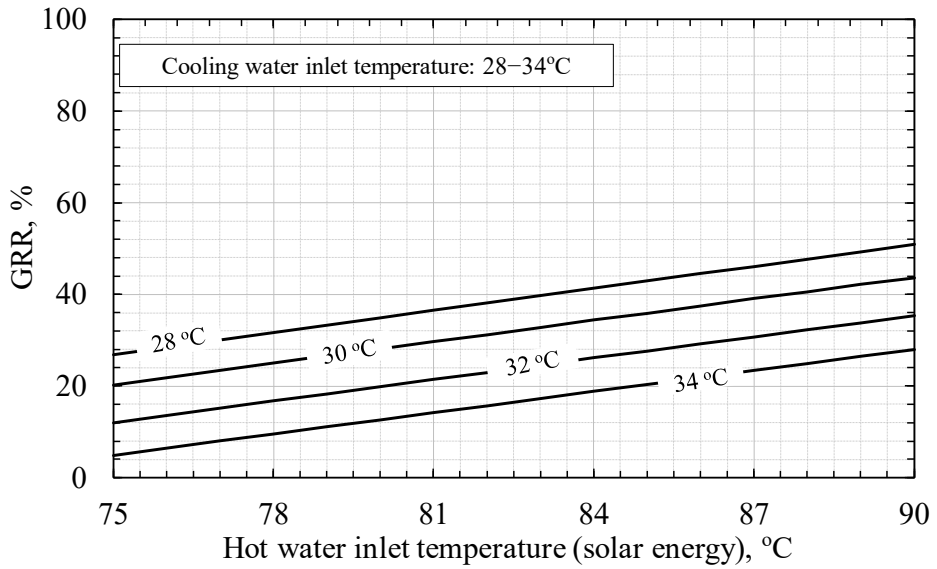

Fig. 5.3 Gas reduction ratio of single-double-effect absorption chiller

5.3.3 Minimum hot water temperature

The knowledge of the minimum value of the hot water inlet temperature enabling the system to exploit solar energy in different operative conditions is fundamental for the proper functional operation of the system. Fig. 5.3 indicates that the existence of this minimum value is suggested by the trend of the GRR as a function of hot water inlet temperature. Specifically, when the line corresponding to a fixed cooling water temperature crosses the horizontal axis (GRR=0), the system will operate at the same efficiency as that of a conventional double-effect absorption chiller. Additionally, the components dedicated to the collection and utilisation of solar energy would not, in fact, elicit any operational advantages. On the contrary, they would generate additional complexities, lower reliability, sources of additional losses, and a higher investment cost. Fig. 5.4 illustrates the lowest hot water inlet temperature which was required by the system at the special temperature generator when the system is controlled to obtain constant cooling capacity and chilled water outlet temperature (Table 5.1) by changing the gas consumption. This parameter is calculated as the temperature of the hot water at which the solution would not receive heat from the solar energy. The minimum hot water inlet temperature is affected by the cooling water temperature as well as the chilled water temperature and flow rate. In particular, hot water

at 58.8 °C can still be used in the STG at a cooling water inlet temperature of 28 °C, whereas, when the cooling water temperature increases up to 34 °C, then the minimum hot water inlet temperature required by the system reaches a value of 72.2 °C.

A low value of the cooling water inlet temperature leads to a diminished HTG gas consumption. It also causes the overall solution temperature to decrease when the solution temperature to STG is decreased, in a manner that it allows use of the lower, hot water inlet temperature.

Knowledge of the minimum limit of the hot water inlet temperature can be used as a fundamental criterion for the system control and for hot water usage. When the value is close to this limit, the utilisation can be paused until it reaches the appropriate value.

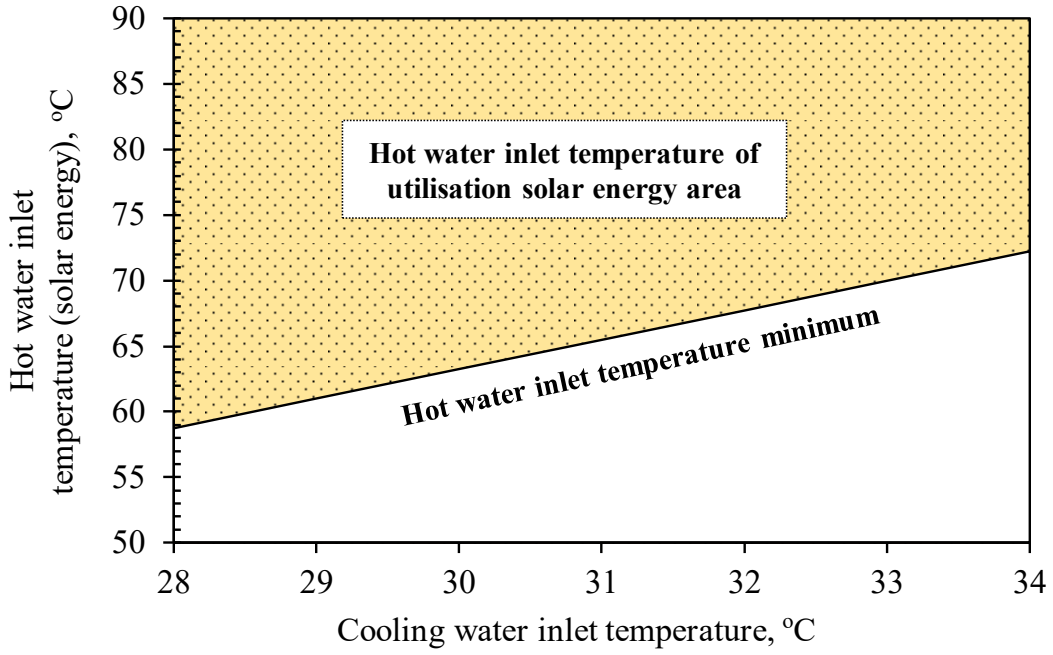

Fig. 5.4 Minimum limits for the hot water inlet temperature at fixed chilled water outlet temperature of 7°C and cooling capacity 239 kW

5.3.4 Energy input

The total input energy, and the ratio between the input energy derived from the hot water of the solar panels and that obtained from the combustion of the gas, can be obtained from Fig. 5.5(a)–(d) for different temperatures of the hot water at the special temperature generator. It can be highlighted that the simulation results yield a different total energy requirement for different cooling water inlet temperatures and hot water inlet temperatures. Specifically, at fixed hot water

temperature, a lower cooling water temperature reduces the vapour pressure at the SCOND, therefore, the vapour generation at STG increases. Accordingly, since the cooling capacity is set to be constant the vapour generation at the HTG decreases lowering the gas consumption. At a low cooling water inlet temperature, the total input energy is larger if compared to other cooling water inlet temperatures within the range considered. Even though the energy input is large, the energy input composition is dominated by the hot water heated by solar energy. The highest input energy is 234.7 kW at a cooling water inlet temperature of 28 °C and a hot-water inlet temperature of 90 °C, with an energy composition of 152.5 kW of solar energy and 82.2 kW of gas energy. The worst operating condition of this system (cooling water temperature of 34 °C and a hot water inlet temperature of 75 °C) from an efficiency standpoint requires the lowest total input energy (184.1 kW). However, in this circumstance, the smallest amount of solar energy (13.4 kW, or equivalently, 7.3% of the total energy input) is utilised. The thermal efficiencies of single-effect (driven by solar energy) and double-effect (driven by gas) cycles determine the cooling capacity subdivision among these two sub-cycles.

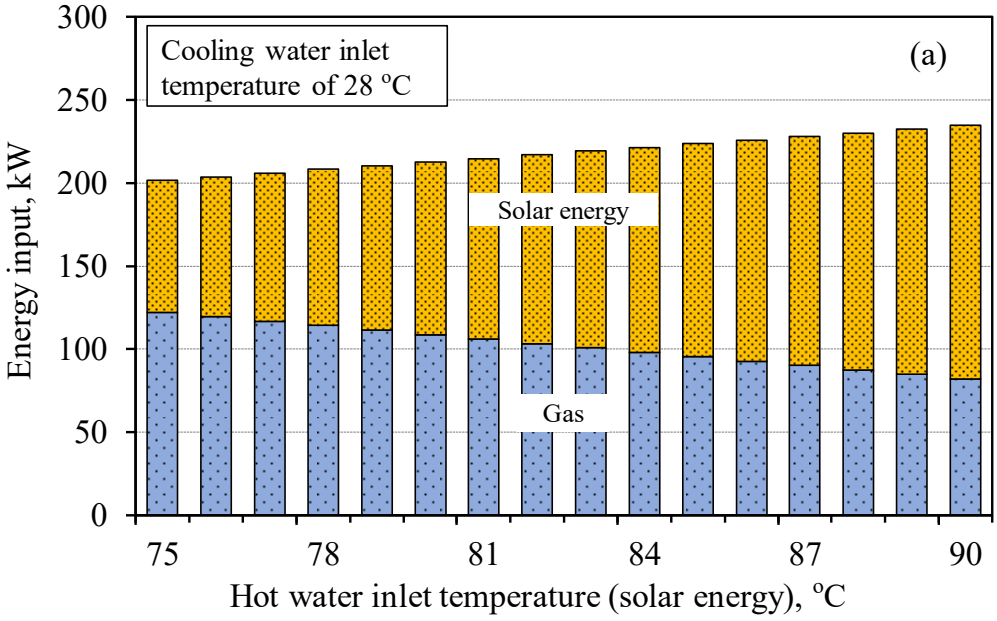

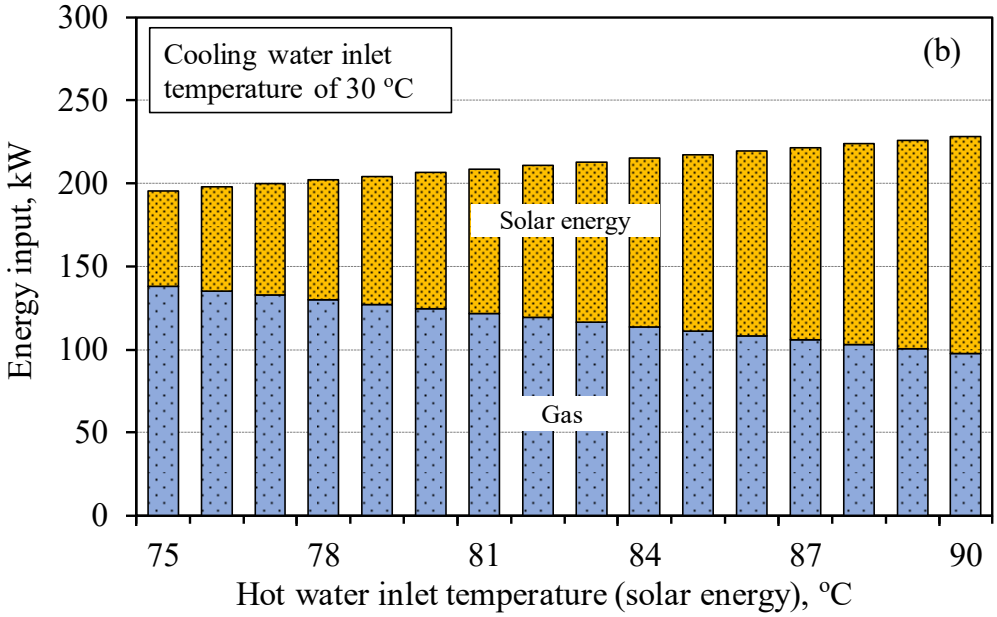
Cooling water inlet temperature of 30 °C
(b)
Solar energy
Gas
Energy input, kW
300
250
200
150
100
50
0
75
78
81
84
87
90
Hot water inlet temperature (solar energy), °C

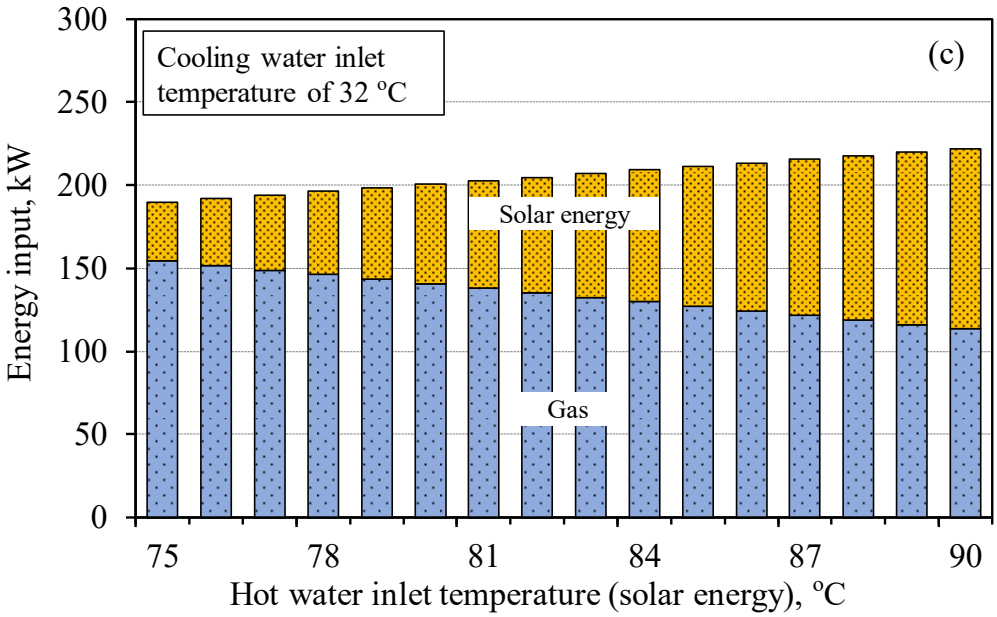
Cooling water inlet temperature of 32 °C
(c)
Solar energy
Gas
Energy input, kW
300
250
200
150
100
50
0
75
78
81
84
87
90
Hot water inlet temperature (solar energy), °C

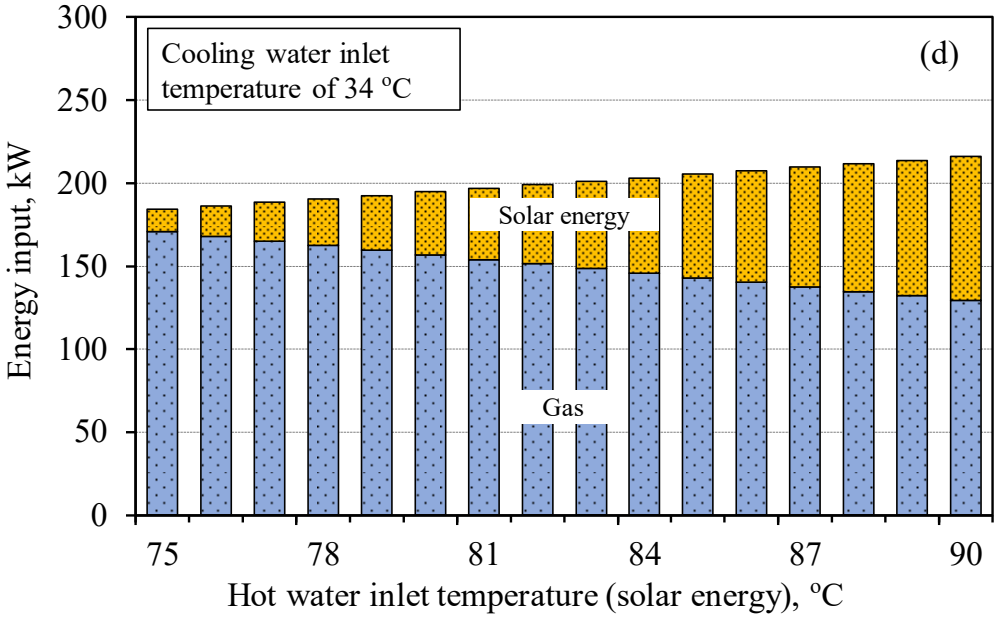

Fig. 5.5 Energy input of single-double-effect absorption chiller at fixed chilled water outlet temperature of 7 °C and cooling capacity 239 kW for the cooling water inlet temperature of (a). 28 °C, (b). 30 °C, (c). 32 °C, and (d). 34 °C,

4.3.5 Ratio of cooling capacity generated by solar energy and gas

The ratio of the cooling capacity generated by the solar energy and gas is described in this paragraph. Since this analysis considers a constant cooling capacity at a fixed chilled water outlet temperature of 7 °C, the total amount of refrigerant required to realise the cooling effect is also constant. Accordingly, the ratio of the cooling capacity coming from the solar energy and gas combustion is proportional to the ratio of the refrigerant desorbed in the STG [Eq. 5.3] due to solar energy and the part desorbed in the HTG and LTG [Eq. 5.4] due to the gas combustion. These two parts are generated following two different thermodynamic cycles, namely those for the single-effect and double-effect (Fig. 5.5). Therefore, knowing the ratio of the cooling capacity generated by the solar energy and the gas, it is possible to understand the performance of the single-effect, and the double-effect cycles realised inside the system. This ratio is influenced by the cooling water inlet temperature, and also the hot water inlet temperature from the solar energy itself. The trends of this parameter match the trends of energy input represented in Fig. 5.5. However, this parameter cannot be obtained directly from the comparison of the total energy input from the solar energy and gas.

Fig. 5.6 shows the percentage of the cooling capacity that is produced by the solar energy and gas as a function of the hot water inlet temperature (from solar energy), for different values of the cooling water inlet temperature (ranging from 28 °C to 34 °C). Continuous lines represent the

percentage of the total cooling capacity that can be ascribed to the energy provided by the gas combustion. Reciprocally, dashed lines depict the percentage of the total cooling capacity generated by the solar energy for corresponding values of cooling water inlet temperatures. When the system is supported at a hot water temperature of 90 °C from the solar collector, and heat rejection occurs with a cooling water inlet temperature of 32 °C, i.e. 35% of the cooling capacity is generated by solar energy.

The difference between the ratio of the cooling capacities and the ratio of the input energies (Fig. 5.6) is related to the different performances of the single-effect and the double-effect cycles. As already pointed out, the heat collected from the solar energy drives a single-effect cycle to produce the cooling effect. On the other hand, the energy obtained from the gas combustion drives a double-effect cycle, and as a consequence, is capable of achieving a higher cooling efficiency. Specifically, at a hot water inlet temperature of 90 °C and a cooling water inlet temperature of 30 °C, 57% of the total energy input is derived from solar energy. This difference can be explained by considering that solar energy drives a single-effect cycle that is at a lower efficiency than the double-effect cycle. Hence, at this condition, even though the portion of solar energy is higher (57%) than the energy input from gas (43%), 57% of the cooling capacity is generated by energy coming from the gas combustion.

Fig. 5.8 highlights that the cooling water inlet temperature is really important for maximisation of the utilisation of solar energy. At a cooling water inlet temperature of 34 °C, and even though the hot water inlet temperature is 90 °C, the percentage of the cooling capacity by solar energy is really low and around 28%. This percentage value slowly increases when the cooling water inlet temperature decreases to 28 °C, and even if the percentage of the cooling capacity by the solar energy is higher than that of the gas energy. In addition, it is possible to predict based on these results when the percentage values are in balance. The balance in these percentages occurs at cooling water inlet temperatures of 28 °C, and at hot water inlet temperatures of 89.25 °C.

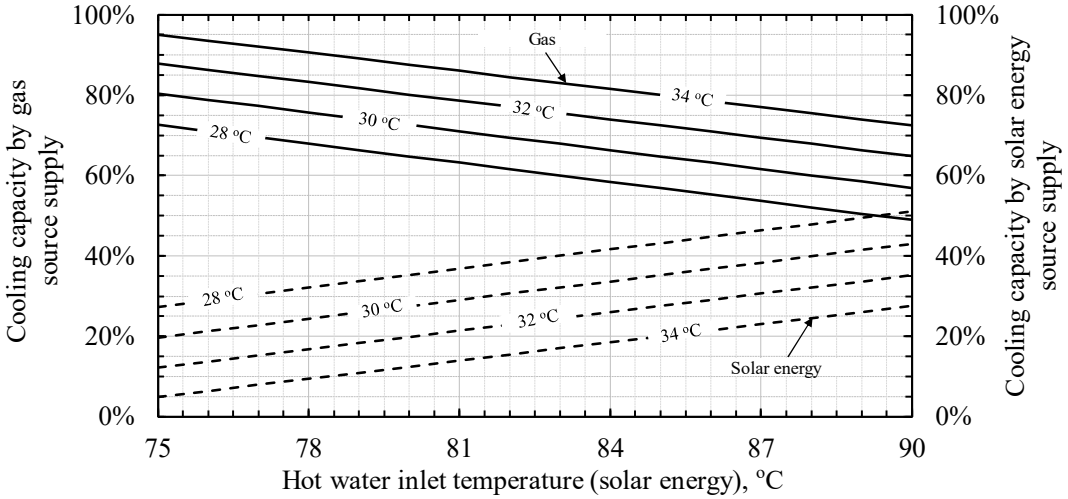

Fig. 5.6 Percentage of cooling capacity generated by solar energy and gas for a chilled water outlet temperature of 7 °C

Summary

Solar energy is accessible throughout the year in tropical regions. The latest development of absorption chillers has demonstrated that these systems are suitable for effective use of solar energy. The utilisation of solar energy for heat-driven cooling systems has significant advantages. Without a doubt, solar energy represents a clean energy source that is available without any additional fuel cost, and that can be proportionally accessible when the cooling load increases during the middle hours of the day. This study focuses on a single-double-effect absorption chiller machine that was installed in Indonesia. The system is driven by a dual-heat source that combines gas and solar energy. This system is characterised by simulating its performance in various conditions in terms of the cooling water (28–34 °C) and the hot water (75–90 °C) inlet temperatures. The reference operating condition of this system is 239 kW of cooling capacity. The mathematical model is validated and shows a good agreement with experimental data. In the operative range considered, simulation results yield a coefficient of performance between 1.4 and 3.3, and a gas reduction ratio from 7 to 58% when compared to a double-effect absorption chiller driven by gas. Based on the simulation results, this system is expected to have a good potential for widespread use in tropical Asia regions.

Chapter 6
Operation performance enhancement

The configuration of the single-double-effect absorption chiller uses two energy sources, solar and gas, at the same time in manner dependent on the specific conditions. Owing to the complex interconnections between the components under continuous strong solar radiation and high tropical temperatures, an appropriate operation strategy of this system is required. Such a operation strategy would act directly on the internal parameters in order minimise the use of gas while keeping the system in a safe operation. A new system configuration of a single-double-effect absorption chiller for solar cooling applications in tropical areas is under analysis, and a newly developed performance maximisation method is suggested. The operation performance of this system can be improved by the proper manipulation of internal parameters, the absorber outlet solution flow rate and the solution distribution ratio, achieving a significant reduction of the primary energy consumption, without any additional cost while safely operating the system taking into account its technological constraints (crystallisation and overpressure).

6.1 Manipulated parameters, technical constraints, and performance definition

6.1.1 Manipulated parameters

The outlet solution mass flow rate of the absorber and the solution distribution ratio, Fig. 2.13(b), play a significant role when the system operates in the single-double-effect mode. The conventional operation strategy controls the solution mass flow rate of the absorber outlet depending on the cooling capacity, and the chilled water outlet temperature by adjusting the gas heat input. In addition, this system has another degree of freedom, namely the solution distribution ratio, which can be used to improve the operation performance. The solution distribution ratio γ (Eq. 6.1) of this system is defined as the ratio of the solution mass flow rate of the HTG inlet $\dot{m}_{s,in,HTG}$ to the solution mass flow rate of the LTG outlet $\dot{m}_{s,out,LTG}$. Based on the current design, the distribution ratio is 0.5. This value was selected to avoid the occurrence of crystallisation of the strong solution. The distribution ratio is defined when the double-effect operates alone (double-effect mode) or supports the single-effect (single-double-effect mode). Therefore, the appropriate solution mass flow rate and distribution ratio need to be investigated for enhancing the operation performance.

$$\gamma = \frac{\dot{m}_{s,in,HTG}}{\dot{m}_{s,out,LTG}} \tag{6.1}$$

6.1.2 Technical constraints

The simulation procedure is carried out under specific technical constraints, depicted in Fig. 2.13(b). First, crystallisation should be considered as the upper limit of the outlet concentration

at the high-temperature solution heat exchanger. Therefore, the maximum strong solution concentration X_{S4} is assumed 65% to assure safe operability in the range of the analysis conditions. Second, the internal pressure of the HTG P_{R4} is limited below 101.3 kPa in order to keep it below the atmospheric pressure because of the maintenance expenditures derived from pressurised vessels.

When using the outlet solution temperature of the high-temperature heat exchanger at a strong concentration as the input value, the crystallisation line is calculated using the linear trend line (ASHRAE handbook 2013–Fundamentals) for a solution temperature from 40.95 up to 101.9 °C (Eq. 6.2). When the input value is higher than 101.9 °C, then the crystallisation line is assumed at 70% solution concentration.

$$X_{CL} = 0.0804T_{HHX,out} + 61.677 \tag{6.2}$$

6.1.3 Performance definition

The single-double-effect absorption chiller can be conceived as the combination of two systems in one. Thus, when this system works in the single-double-effect mode, the COP can be defined for the single-double-effect cycle, single-effect cycle (driven by solar energy), and double-effect cycle (driven by gas). The COP of the single-double-effect is the total cooling capacity Q_E divided by the gas consumption Q_{HTG} (Eq. 6.3). The COP of the double-effect (COP_{DE}) is the cooling capacity $Q_{E,DE}$ (produced only by the double-effect cycle) divided by the gas consumption Q_{HTG} (Eq. 6.4). The COP_{DE} is used for a comparison with the COP.

$$COP = \frac{Q_E}{Q_{HTG}} \tag{6.3}$$

$$COP_{DE} = \frac{Q_{E,DE}}{Q_{HTG}} \tag{6.4}$$

The cooling capacity produced only by the double-effect cycle is calculated from the ratio of refrigerant mass flow rate generated from gas to the total refrigerant mass flow rate generated from both solar and gas. Since this machine uses direct-fired in the high temperature generator, the calculation of gas consumption is obtained from how much gas flow rate is needed multiplied by the lower heating value (LHV) of gas.

6.2 Simulation methodology

The presented model calculates the inlet and outlet conditions of mass and energy balance considering the internal (working fluid side) and external (water side) parts of each component. The equations retrieve the values of all properties of lithium bromide/water solution and water refrigerant from ASHRAE Handbook 2013-Fundamentals and the Japan Society of Mechanical Engineers Steam Table 1980 SI [72) 73)].

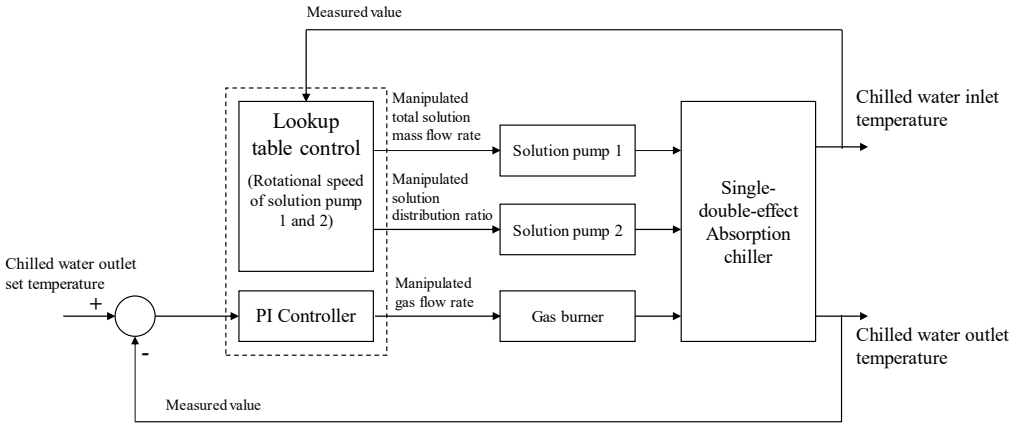

Fig. 6.1 Control block diagram of single-double-effect absorption chiller.

Fig. 6.1 shows the control algorithm used to control the chilled water outlet and inlet temperatures that satisfy the required cooling capacity. Three components are manipulated to obtain the best performance. The first two, the solution pumps 1 and 2, are controlled by the inverter to make the solution's absorber outlet mass flow rate and the solution distribution ratio appropriate according to the required cooling capacity. The third component, the gas flow rate, is controlled by a PI controller to keep the required chilled water outlet temperature at 7 ºC. For the inverter controlled solution pumps, a lookup table control is used to find the maximum performance at each condition. The lookup table control sends a signal, according to the feedback of the chilled water inlet temperature, to the inverter of the solution pumps to manipulate the right total solution mass flow rate and solution distribution ratio. The chilled water inlet temperature is proportional to the cooling capacity because the chilled water flow rate and outlet temperature are kept constant. Therefore, the measured chilled water inlet temperature can be directly used in the lookup table as an input in the control algorithm.

The simulation flow chart in Fig. 6.2 shows the calculation method that was adopted in order to calculate the appropriate operation points of the two manipulated parameters. The system operation conditions are given as input values. Specifically, the cooling water inlet temperature is manipulated in accordance to the required cooling capacity; for example, the full-load operation uses inlet cooling water at 32 °C, and 0% of the nominal cooling capacity is associated to 27 °C. The simulation is carried out by iteratively solving all the equations presented in section 4 until the convergence of the assumed values and results is reached in the whole defined range of the manipulated parameters: absorber outlet solution mass flow rate and the solution distribution ratio

(Fig. 6.2). When the convergence fulfils a maximum error of 10^{-6} the system COP is calculated. The thermodynamic properties are calculated according to the assumed values (pressure, temperature, mass flow rate, and concentration of each component). Therefore, the final results for a set of manipulated parameters are used as the next assumed values. In this way, convergence to the condition that maximises the system performance can be reached in the entire range of absorber outlet solution mass flow rate and the solution distribution ratio. Note that the assumed initial values differ from each other at different cooling capacities. The obtained results were plotted in contour graphs (see results and discussion) to identify the maximum achievable COP under the specified technical constraints.

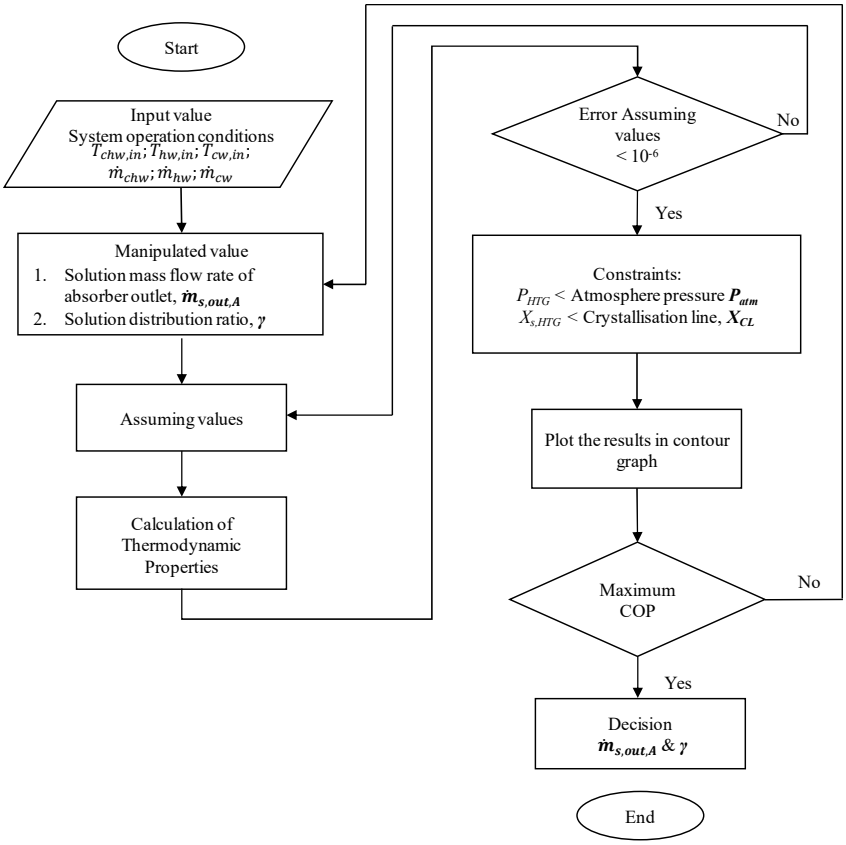

Fig. 6.2 Simulation flow chart.

6.3 Experimental conditions, simulation conditions, and evaluation methods

The design/manufacturing conditions of a first case [64] regarding the cooling capacity, the chilled, cooling, and hot water temperatures as well as the flow rates, are summarised in Table 6.1. The system was designed to operate in a range of hot water inlet temperatures between 75 °C and 90 °C. The experimental results reported in Fig. 2.7 are taken into consideration to validate the model and evaluate the performance improvement by adopting the proposed operation strategy based on the range of conditions in Table 6.1.

An improvement of the system performance is targeted by searching for the operation point which maximises the COP and fulfils the technical constraints. Subsequently, the same method is adopted for a second case of the single-double-effect absorption chiller installed in Indonesia. These two cases feature the same system configuration. However, the hot, cooling, and chilled water flow rates differ in order to match the specific operation conditions.

Table 6.1 Operation conditions

	Value	Unit
Chilled water inlet temperature	15	°C
Chilled water outlet temperature	7	°C
Chilled water flow rate	30.2	m^3/h
Cooling water inlet temperature	32	°C
Cooling water flow rate	79.9	m^3/h
Hot water inlet temperature	75–90	°C
Hot water flow rate	9.2	m^3/h
Cooling capacity	281	kW

Matlab software is used to calculate the equation system using a Newton-Raphson method with a Jacobian matrix. The simulation uses the same conditions as the actual field test.

6.4 Results and discussion

In order to maximise the performance of the system operated by the conditions shown in Table 6.1, its COP is investigated by varying the solution mass flow rate of the absorber outlet and the solution distribution ratio. In Fig. 6.3 the X and Y axis represent, the solution distribution ratio and the solution mass flow rate of the absorber outlet, respectively. The maximum COP (1.6) can be quickly noticed in Fig. 5.3(a) inside the smallest contour line. Fig. 6.3(b) describes the performance of the double-effect cycle while working to support the single-effect side. Figs. 6.3(c), 6.3(d), and 6.3(e) show the strong solution concentration line, the crystallisation line, and pressure at the HTG, respectively. The crystallisation lines on the graph delineate the region of possible operative conditions since the strongest solution concentration at the lowest temperature (outlet of the HHX) must be smaller than the crystallisation value. The internal pressures of the HTG, resulted from the calculation, are always lower than the pressure constraint. When the distribution ratio is lowered the pressure of LTG decreases, therefore, the crystallisation point

moves to lower concentrations, Fig. 6.3(d). On the contrary, for lower distribution ratios and absorber outlet solution mass flow rates, the strong solution concentration and the pressure of HTG increase, Fig. 6.3(c) and 6.3(e).

For the same conditions of cooling capacity, the hot and cooling water inlet temperature when the distribution ratio decreases while the absorber outlet solution mass flow rate is kept constant, a smaller amount of solution reaches the HTG, hence, making the outlet solution concentration and temperature higher. The solution enters the HHX at a higher temperature and increases the outlet solution temperature of the cold side of the same heat exchanger. Consequently, the temperature of the inlet solution to the HTG increases. Therefore, the solution concentration difference in the HTG becomes greater. Furthermore, if the distribution ratio is excessively low, there is a possibility of reaching the crystallisation condition of the strong solution at the HTG outlet. Therefore, the outlet solution temperature of the solution high heat exchanger HHX must be controlled above a specific value to avoid crystallisation.

It can be observed that, for a given operative condition, a performance peak can always be identified when the solution mass flow rate of the absorber outlet varies, while the distribution ratio is kept constant or vice versa. In other words, the maximum performance can always be calculated, Fig. 6.3(a). For a given cooling capacity, hence, a defined amount of refrigerant vapour needs to be generated, the maximum COP operation is achieved when the heat input at the HTG is minimised considering the absorber outlet solution mass flow rate and solution distribution ratio by simulation as shown in Fig. 6.3(a).

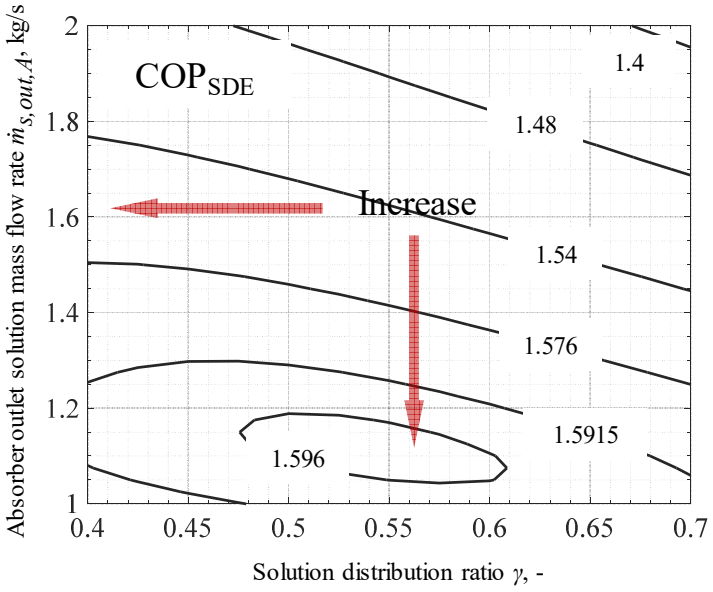

(a) COP line

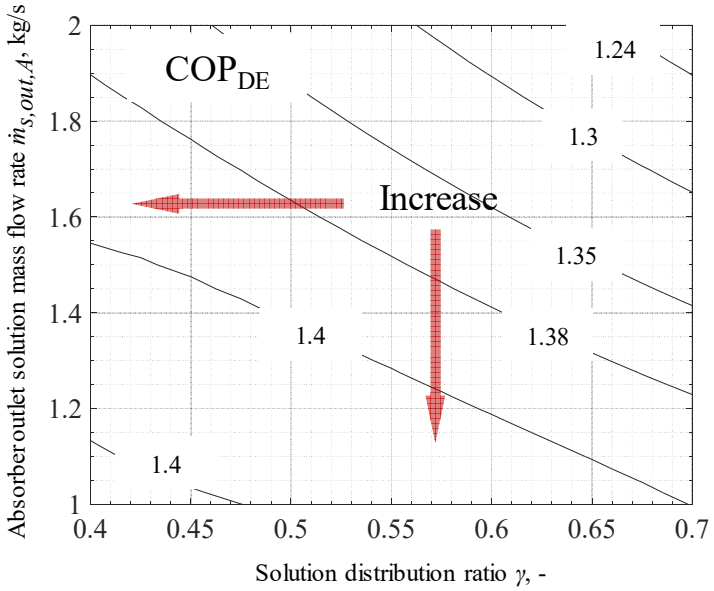

(b) COP_{DE} line

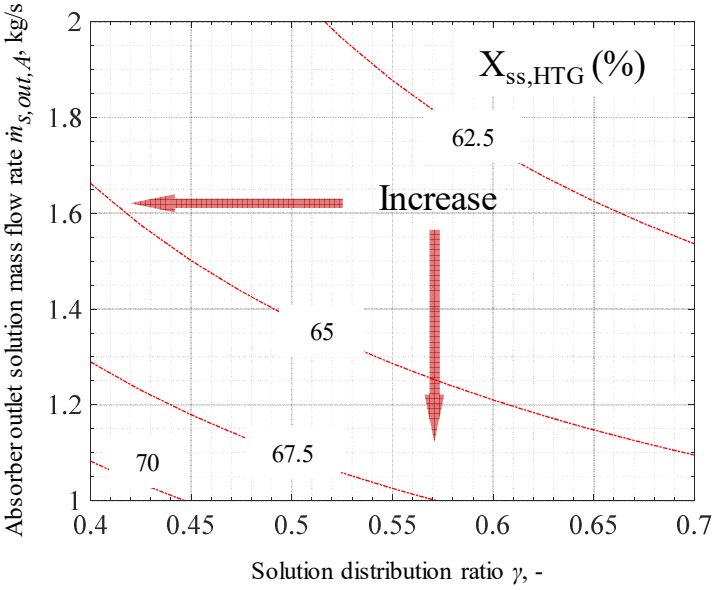

(c) Strong concentration line

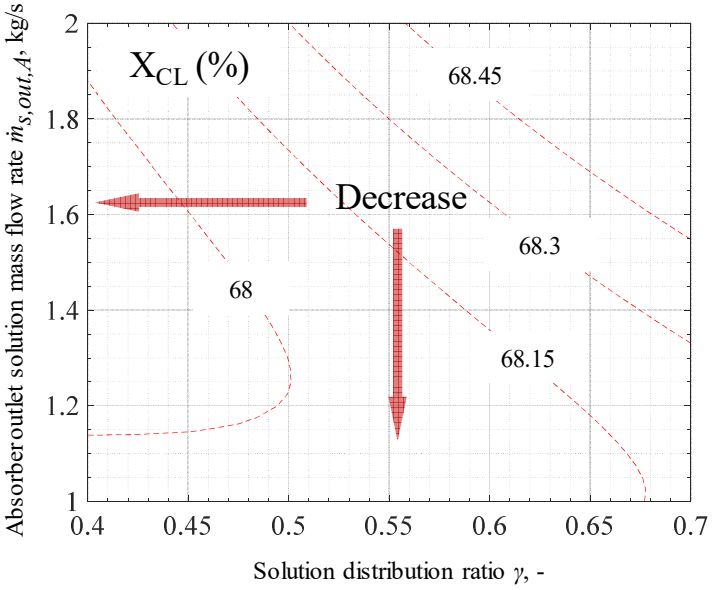

(d) Crystallisation line

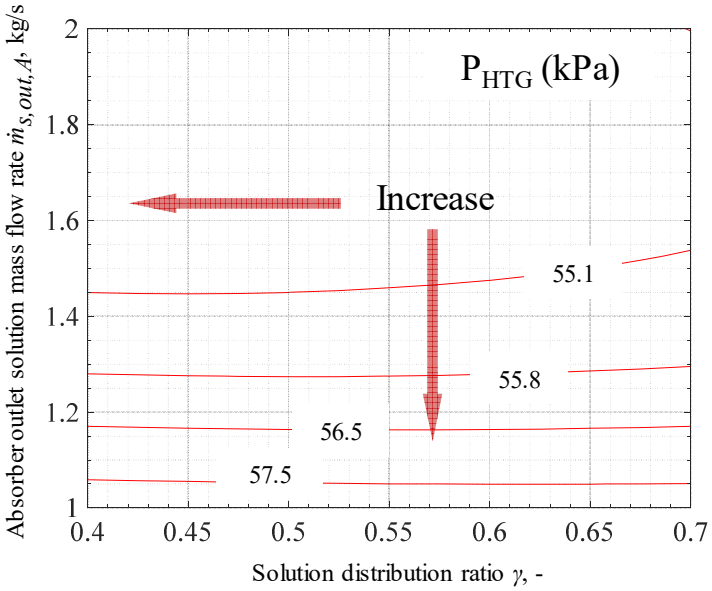

(e) Pressure line

Fig. 6.3 Each contour line at Q_E 100% rated point

Figs. 6.4, 6.5, and 6.6 show the maximum operation performance for a cooling capacity of 100%, 80%, and 60% of the maximum value at the hot water inlet temperature of 75 °C, respectively. The highest COP contour line shown in Fig. 6.4 defines the range of these key parameters, which yields close to maximum operation performance for full-load operation (100%

cooling capacity). The strong solution concentration is close to the crystallisation line; thus, the maximum strong solution concentration of 65% is set for safe system operation. At full-load, a maximum COP of 1.59, marked with a yellow dot, is placed at the contour line tangent to the 65% strong concentration line from P point (black dot). When operating at part-load (cooling capacities of 80% and 60%), the maximum COP point can be achieved without conflicting with the safety-restricted area.

When compared to the design values of the manipulated variables, distribution ratio 0.5 and solution flowrate 1.8 kg/s, different manipulated values are required. For instance, at the condition of 100% of cooling capacity, the distribution ratio must be increased from 0.5 to 0.625 and the absorber outlet solution mass flow rate must be decreased from 1.8 kg/s to 1.19 kg/s. Nevertheless, for the condition in which 80% of the nominal cooling capacity is required, the maximum COP can be achieved by reducing the solution mass flow rate to 1.08 kg/s and distribution ratio to 0.475. In addition, by observing Figs. 6.4−6.6 without considering the constraint of 65% maximum strong solution concentration to reach the maximum performance, the maximum COP operation point of 100%, 80%, and 60% have the absorber outlet solution mass flow rates: 1.19, 1.08, and 1.02 kg/s respectively and the solution distribution ratios: 0.625, 0.475, and 0.375 respectively. In other words, the maximum COP operation can be obtained using the certain absorber outlet solution mass flow rate and distribution ratio.

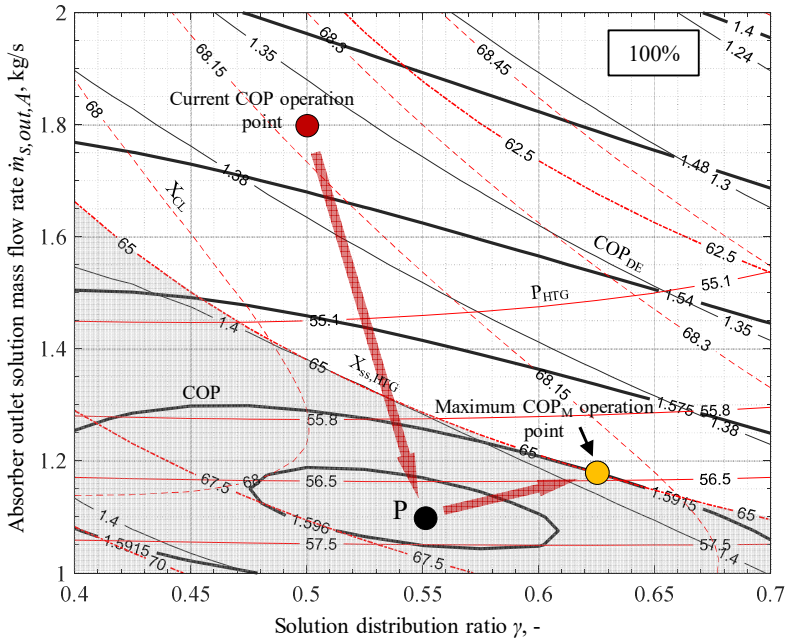

Fig. 6.4 Maximum operation point of 100% cooling capacity at 75 °C hot water inlet temperature.

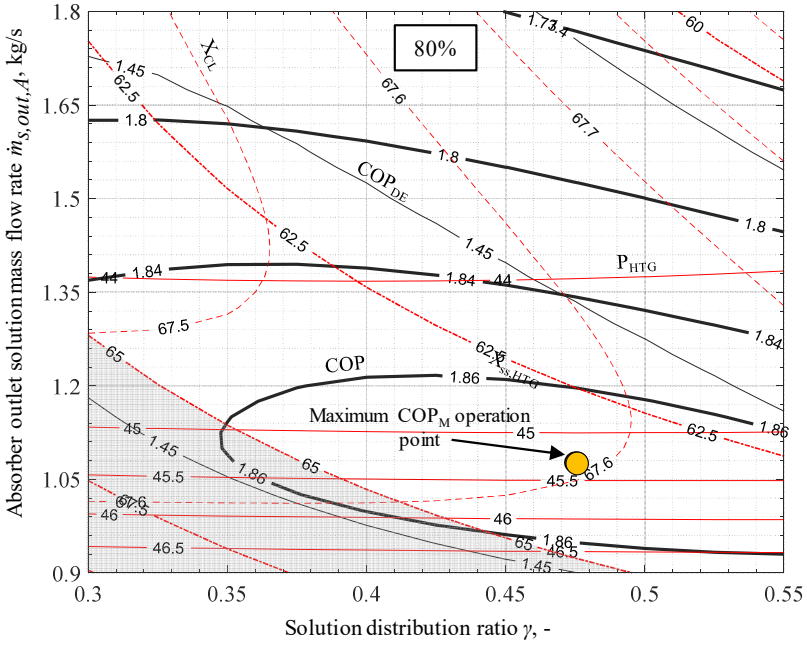

Fig. 6.5 Maximum operation point of 80% cooling capacity at 75 °C hot water inlet temperature.

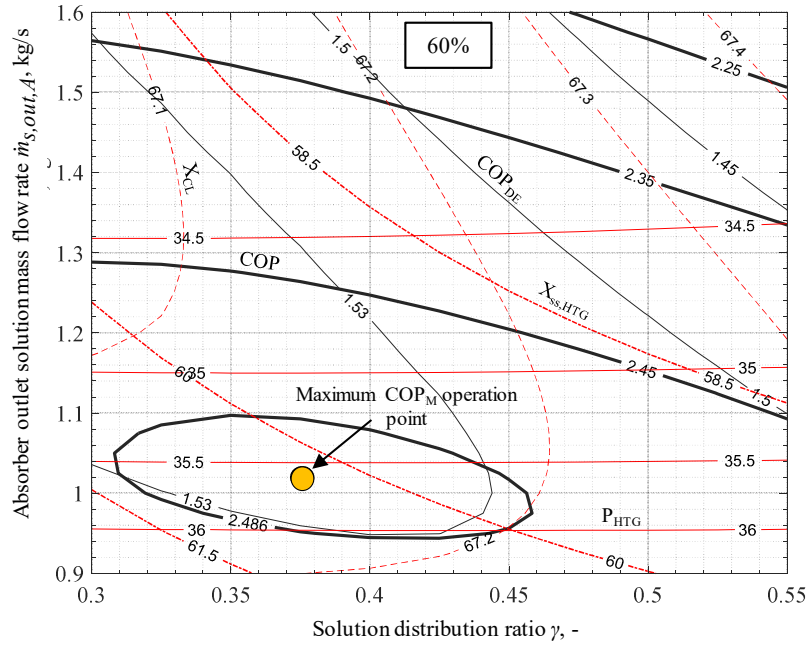

Fig. 6.6 Maximum operation point of 60% cooling capacity at 75 °C hot water inlet temperature.

Fig. 6.7 shows the maximum operation performance (COP_M) of the system, according to the simulation results, analysed from Figs. 6.4–6.6. In the same graph, the COP_M is compared with the simulation COP_{CON} and experimental results COP_{DE} in order to estimate the related performance improvement. COP_{CON} is the simulation result based on the same operation conditions in COP experiment with mark ◯. As an example of 100% cooling capacity, the maximum operation point can be increased from COP 1.48 to 1.59. As the second term of comparison, the maximum COP operation (continuous line in Fig. 6.7) can be compared with the COP_{DE} of the corresponding double-effect cycle (dashed line), yielding an upgrade of 14%. From Fig. 6.7, the new operation points, along with the COP_M line, can enhance the operation performance approximately 5% of COP_{CON} by conventional rated operation points. Moreover, the new operation points can raise the performance approximately 14–62% of the performance COP_{DE} of the double-effect cycle. In addition, by plotting the experimental data (markers) and the simulation results (dash dot line) in in Fig. 6.7 have the additional purpose of supporting the model results and showing the model accuracy. Table 6.2 shows the new lookup table that can improve the performance of this system based on the new operation points along with the COP_M line. Therefore, this operation strategy can also be applied for the efficient operation performance of the same system installed at the University of Indonesia in the tropical area.

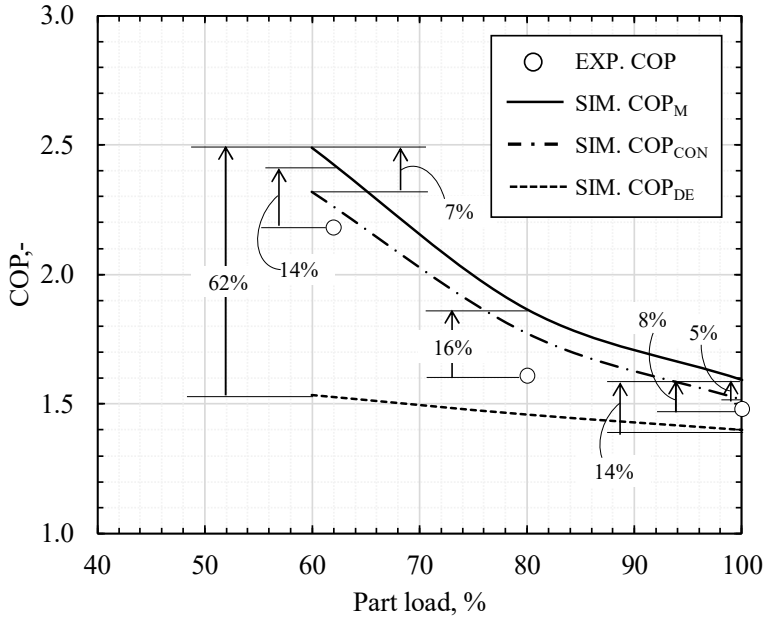

Fig. 6.7 Simulated and experimental COP for hot water inlet temperature of 75 ºC.

Table 6.2 Operation conditions by the lookup table.

Chilled water temperature		Cooling capacity, %	Solution flow rate at pump 1, kg/s	Solution flow rate at pump 2, kg/s	Distribution ratio, -
Inlet, ºC	Outlet, ºC				
15.0	7.0	100	1.175	0.695	0.625
13.4	7.0	80	1.080	0.487	0.475
11.8	7.0	60	1.020	0.364	0.375

The plant, Fig. 6.8, which has been installed in the Northern Java Island of Indonesia, serves a newly built building of the University of Indonesia. The required cooling load and the operation performance of this system are affected by the fluctuations of the weather and the occupancy of the building. The system operation adopted the conventional operation strategy (0.5 solution distribution ratio and total solution flow rate variation along with cooling capacity). The operation conditions (the flow rate of the chilled, cooling, and hot water) of this system have been set according to the cooling load of the building (239 kW), as listed in Table 6.3. The actual operation data of the system at the University of Indonesia were gathered from 1:05 p.m. until 1:14 p.m. on May 6th, 2015, Fig. 6.9. The actual temperature and flow rate measurements from the field test data are used as the input conditions for calculating and evaluating the maximum operation performance of the real system. The COP measured by the field operation was 1.9 for an average cooling capacity of 61.2%, hot water inlet temperature of 70.5 °C, and cooling water inlet temperature of 29.4 °C.

Table 6.3 Water flow rate and cooling capacity of the absorption chiller at the University of Indonesia

	Value	Unit
Chilled water flow rate	25.7	m^3/h
Cooling water flow rate	68	m^3/h
Hot water flow rate	7.8	m^3/h
Cooling capacity (full load)	239	kW

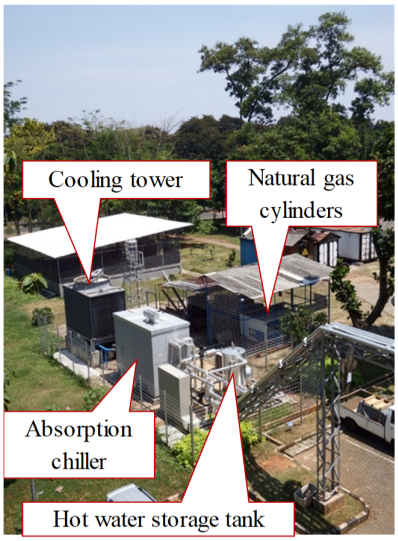

(a) Actual photo of the solar cooling system

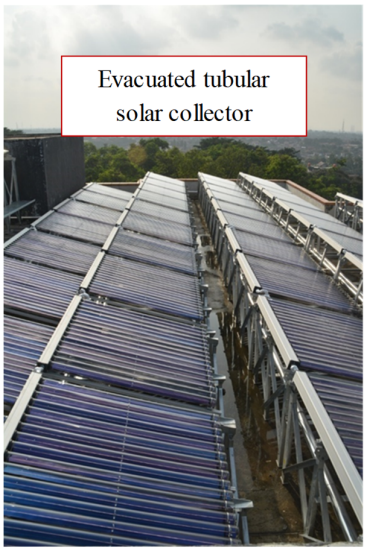

(b) Actual photo of the solar collector

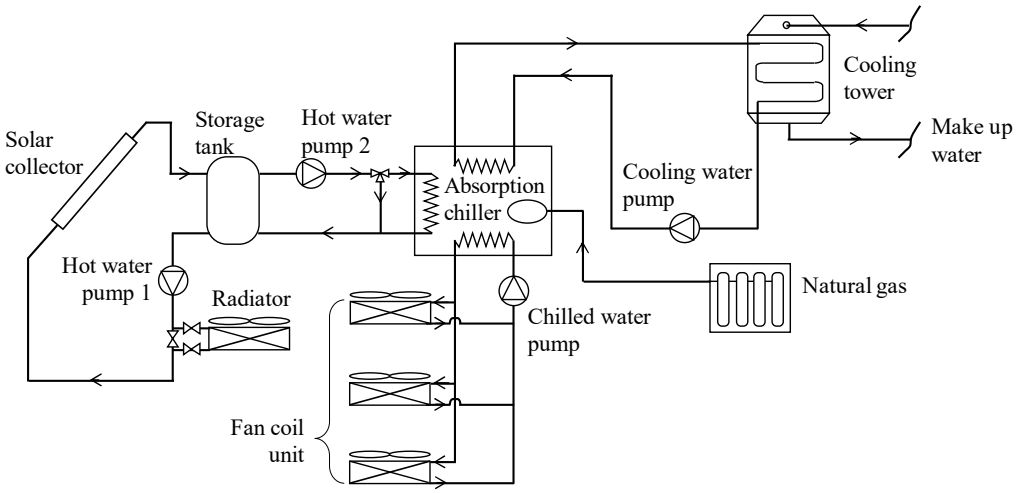

(c) Schematic diagram of the solar cooling system

Fig. 6.8 The solar cooling system field test at University of Indonesia.

The simulation results in Fig. 6.9 are calculated by adopting the conventional operation points (dash line) and the new operation points (continuous line), and compared to the field test data (markers). From the simulation results, it can be observed that the appropriated manipulation of the absorber outlet solution mass flow rate and solution distribution ratio can increase the operation COP from 2.15, based on field operation conditions, to 2.32 (Fig. 6.9). This means that a percentage enhancement of approximately 7.9% can be achieved and the reduction of the absorber outlet solution mass flow rate leads to a smaller electricity consumption from the circulation pumps. From a different standpoint, this performance enhancement can reduce the operation costs and shorten the payback period of the system.

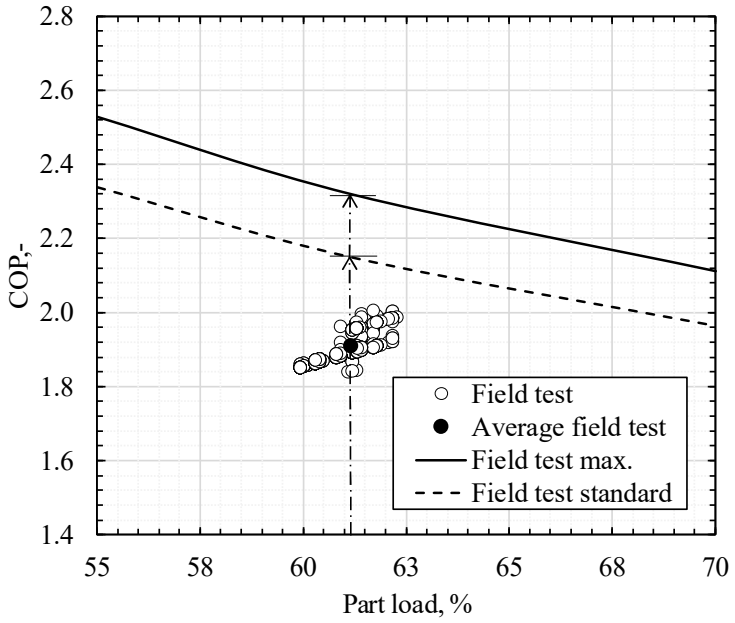

Fig. 6.9 Comparison between actual and enhanced operation performance.

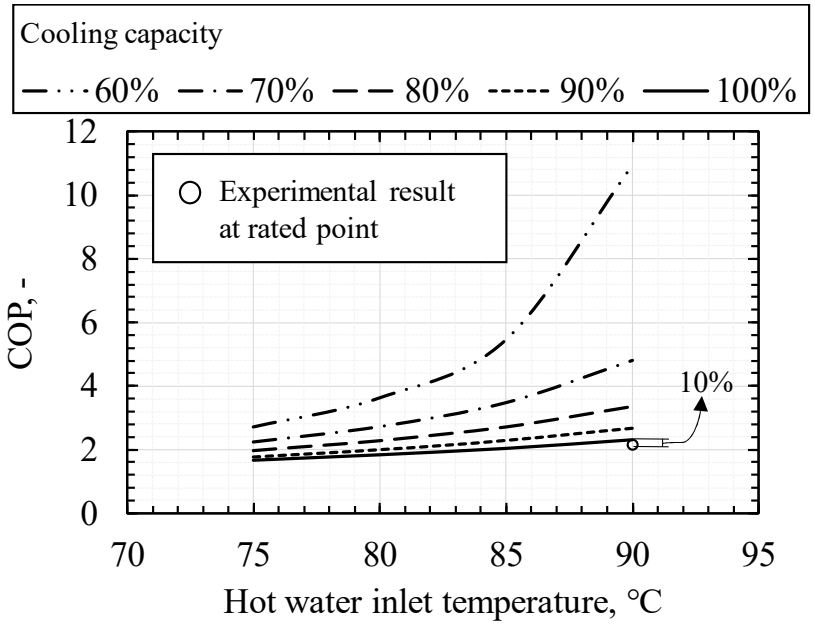

(a) COP

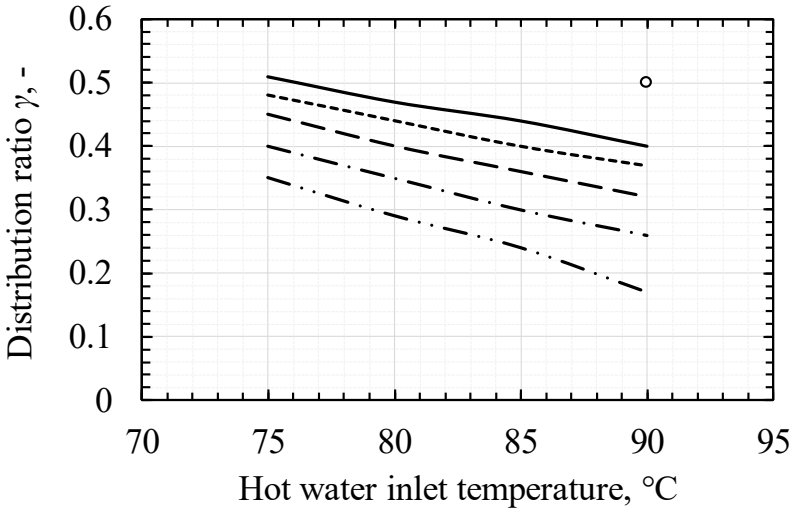

(b) Solution distribution ratio

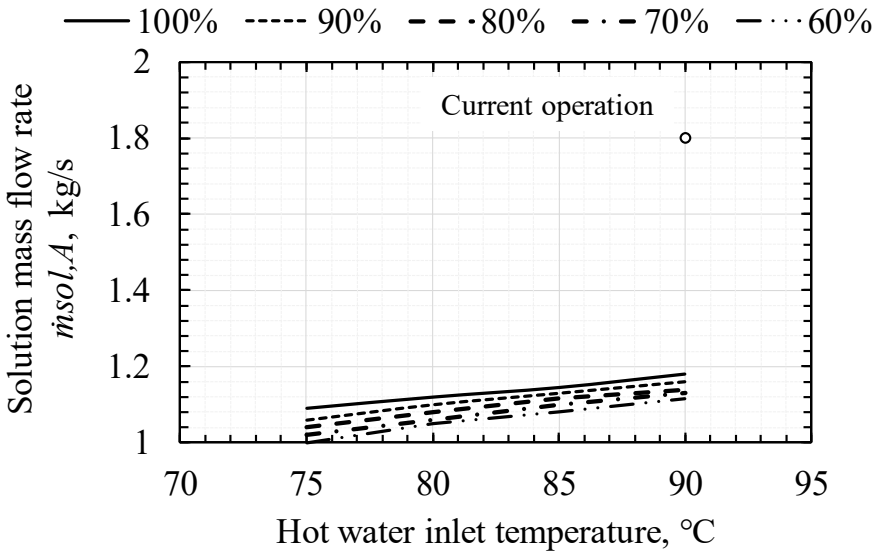

(c) Absorber outlet solution mass flow rate

Fig. 6.10 The effect of the hot water inlet temperature, 75–90°C, for a cooling capacity of 60–100% based on a rated point of 239 kW.

The actual operation performance is influenced by the weather conditions. Therefore, the simulations consider the change of hot water inlet temperature and cooling capacity (Fig. 6.10). Using the same method, the new suggested operation points for the cooling capacity of 60–100% and the hot water inlet temperature ranging between 75–90 °C are obtained. The lines obtained

by plotting all the maximum COP operation points can be seen in Fig. 6.10(a), summarising the main contribution of this study. The maximum COP operation points are obtained from the corresponding combination between the solution distribution ratio and the absorber outlet solution mass flow rate, Figs. 6.10(b) and (c) respectively. It can be observed that, even though the solution distribution ratio that maximises the COP of the system depends on the cooling capacity, the selection of the absorber outlet solution mass flow rate is almost independent from it.

All new operation points (Figs. 6.10(b) and (c)) can be used as a reference for the internal control of this system in order to achieve the maximum performance, where it can be a lookup table control. This lookup table control is used according to two conditions, the cooling capacity and hot water inlet temperature. In order to visualise the enhancement of the COP of this system by using the new operation points and the difference in the operation condition of the manipulated parameters selected the experimental result of the actual condition at the rated point is plotted as a dot marker in Fig. 6.10. Using the new operation points at full load conditions and hot water inlet temperature of 90 ºC, the COP of this system is enhanced approximately 10% compared to the actual field test COP, from 2.11 to 2.31. The new operation points reduce the absorber outlet solution mass flow rate from 1.8 kg/s to 1.18 kg/s and the solution distribution ratio from 0.5 to 0.4. For a cooling capacity of 60%, the COP is enhanced drastically compared to the other cooling capacity conditions. This happens because the system utilises more solar energy than gas. In general, reducing the absorber outlet solution mass flow rate and solution distribution ratio means the rotation speed of the solution pump decreases, which in turn lowers the electricity consumption of the solution pumps.

Summary

Absorption chillers constitute a valuable option for utilising solar energy. Specifically, when installed in tropical regions, this technology ideally matches the needs for refrigeration and air-conditioning because of the abundance of solar energy throughout the year. A single-double-effect absorption chiller combines the single and double-effect configurations to compensate for the unpredictable instantaneous availability of solar radiation and cooling load fluctuations. The operative performance of this system is strongly affected by internal parameters such as the absorber outlet solution flow rate and the solution distribution ratio, which connect the operability of the single and double-effect configurations. Therefore, these important parameters are currently used to maximise system performance while assuring its stability. This study discusses how the COP of a single-double-effect absorption chiller, for solar cooling applications in tropical areas, can be maximised (1.59 at full load, and up to 2.49 at 60% partial load) by manipulating those internal parameters. The simulation results were compared with the experimental data (field test data) and, by adopting the appropriate operation strategy, showed an improvement of the system performance between 14–62% when compared to a corresponding double-effect configuration.

Chapter 7
Suggested operation strategy

Based on the simulation results of Chapter 6, the operation performance of single-double-effect absorption chiller can be enhanced by adjusting the internal parameters according to the cooling capacity and the hot water inlet temperature. Those internal parameters are the solution mass flow rate of the absorber outlet (the total solution mass flow rate) and the solution distribution ratio (the solution flow rate enters the high temperature generator). By using an appropriate combination from those internal parameters, the maximum performance and also safe operability from the single-double-effect absorption chiller operation can be achieved. For the real application, the appropriate internal parameter combinations from Chapter 6 can be the reference for an operation strategy. As known, there are several possibilities operation strategy that can be applied to this system. However, only an applicable operation strategy that can simplify the control process and also be applied in different conditions easily is suggested in this study.

The operation strategy plays an essential role in the absorption chiller system to maintain a stable cooling capacity and keep the system operating safely. Moreover, an appropriate control strategy applied to the absorption chiller could drastically enhance the seasonal system performance. The control system in absorption chiller systems can be classified into internal and external [74) 75)]. The internal control usually refers to the control of the internal parameters (solution and refrigerant) of the system, such as mass flow rate, level, concentration, temperature, and pressure. The external control is used to provide the required cooling load for a building by setting the hot, chilled, and cooling water temperatures and by adjusting or fixing their flow rates. Changing the external parameters gives a direct effect on the internal parameters of the absorption chiller.

Many studies focus on the control of the external parameters of the single-effect absorption chiller. Xiaohong Liao and Reinhard Radermacher (2007) proposed a new control methodology for the LiBr−H_2O air-cooled absorption chiller while avoiding the crystallisation issue. The ambient temperature is used as a feedback to set the chilled water and exhaust temperatures [76)]. For the water-cooled absorption chiller, other researchers showed that the adaptation of the cooling water temperature to the generator temperature could be an option for the external control strategies of the single-effect absorption systems [74) 77–81)]. The cooling water flow rate and cooling tower fan have to be suitably adjusted to achieve the required cooling water inlet temperature. Another study with a different focus on the external parameters is that of A. Shirazi et al. (2016) who suggested a proper external control for a solar-assisted absorption air-conditioning system by adjusting the inlet temperature and flow rate of the hot water; the hot water inlet temperature varied according to the required cooling load [81)].

A new control strategy for absorption chiller systems using Artificial Neural Networks (ANN) has been developed by [75) 82) 83)]. V. Verda et al. (2012) used ANN in the absorption chiller system to minimise its primary energy consumption. The input variables of ANN are the solar

radiation, ambient temperature, and the cooling request [83]. Furthermore, J. Labus et al. (2012) combined ANN and Genetic Algorithms (GA) optimisation to minimise the primary energy consumption of the absorption chiller by adjusting the hot and cooling water inlet temperature while maintaining constant the chilled water outlet temperature [75]. Additionally, J. Labus et al. (2012) manipulated the hot water inlet temperature, cooling water inlet temperature, and cooling water flow rate by using Inverse ANN to produce the proper cooling capacity [83].

Due to the strong interdependence between heat, mass, and momentum transfer [84] [85], controlling the internal parameters of the absorption chiller results into a direct influence on the system operation [86]. Jose Fernandez-Seara and Manuel Vazquez (2001) developed a new internal control strategy for a NH_3−H_2O absorption refrigeration system to set and maintain the optimum generator temperature by adjusting the generator heat flux [87]. Furthermore, Yu-Jie Xu et al. (2016) suggested that manipulation of the generator's solution temperature is better control in off-design conditions for the single-effect absorption chiller [88]. Jeong Ah Seo et al. (2012) proposed an internal control strategy for the solution level in the high-temperature generator, of the double-effect absorption chiller system, for linear controllability and solution economy [89]. This control strategy shows that the solution level can be maintained by adjusting the solution mass flow rate [89] [90].

The focus of this chapter is to find the applicable internal operation strategy that can bring the system to reach the maximum performance. This operation strategy is analysed by using simulation and compared under the same initial condition based on the results of Chapter 6. Finally, a dynamic simulation is used to understand how the suggested operation strategy for the single-double-effect absorption chiller works.

7.1 Description of the applicable operation strategy

The criterion followed to select the operation strategy for the single-double-effect absorption chiller, is that of minimising the primary energy consumption while being of easy applicability for the actual plant. To this aim, several possible control strategies among those that have been used by conventional single- or double-effect absorption chiller are applied to the single-double-effect absorption chiller to be analysed according to the operative points selected in the Chapter 6.

In this study, the operation strategy is focused on the control of the internal parameter according to the results of chapter 6, such as the total solution mass flow rate, and the solution level is chosen instead of the solution distribution ratio because they actually have the same function to manage the solution amount entering the high temperature generator in order to minimise the fuel gas heat input. In actual condition, installing the level sensor for the signal of the solution pump 2 is simpler and cheaper to keep the solution level than using the flow meter to adjust the proper solution distribution ratio.

In order to realise the suggested applicable operation strategy according to the cycle of this system, the chilled water outlet temperature is controlled by adjusting the gas flow rate for the

combuster. The solution level is maintained by controlling the solution pump 2. Where the solution level of the high temperature generator is kept constant for any condition.

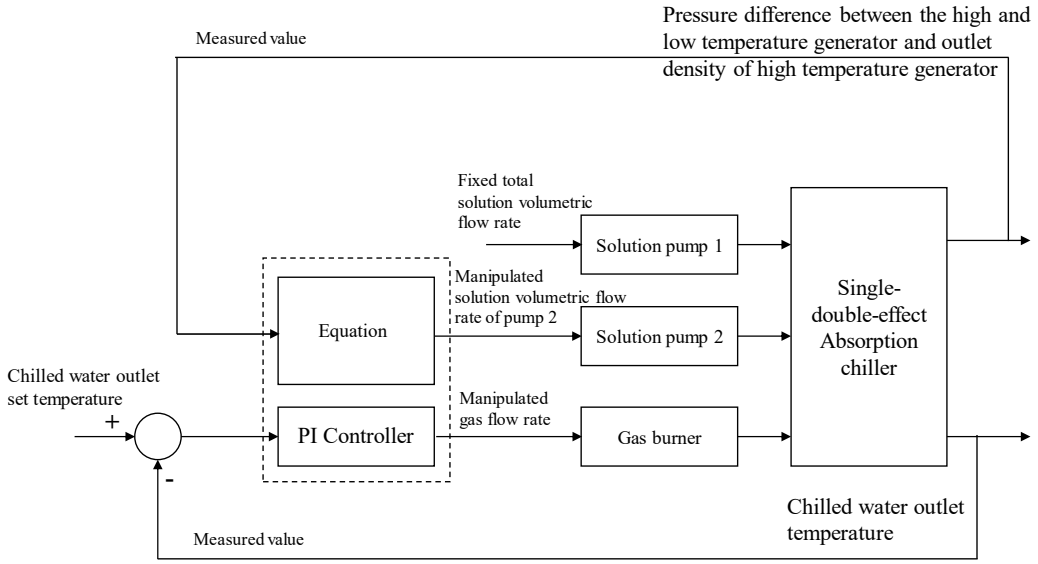

Fig. 7.1 Block diagram of the suggested operation strategy

In the simulation, the solution level calculation of the high temperature generator is simplified. The influence of the driving force from each head of the HTG and the LTG can be neglected because the pressure difference between the high temperature generator and the condenser is bigger than the head difference of the HTG and LTG. In the single-double-effect absorption chiller, the head difference can be ignored. Therefore, by assuming $\rho_{s,out,LTG}H2 \fallingdotseq \rho_{s,out,HTG}H1$, then the solution level of the HTG can be kept constant by using Eq. 7.1, which ensures a constant solution level corresponding to the full load conditions.

$$V_{s,out,HTG} = Vo_{s,out,HTG}\sqrt{\left[\left(\frac{\rho o_{s,out,HTG}}{\rho_{s,out,HTG}}\right)\left(\frac{(P_{HTG}-P_C)}{(Po_{HTG}-Po_C)}\right)\right]} \tag{7.1}$$

where $Vo_{s,out,HTG}$, $\rho o_{s,out,HTG}$, and $(Po_{HTG} - Po_C)$ are obtained from the maximum COP results of full load at Chapter 6. They are then used as the operative point of this operation strategy.

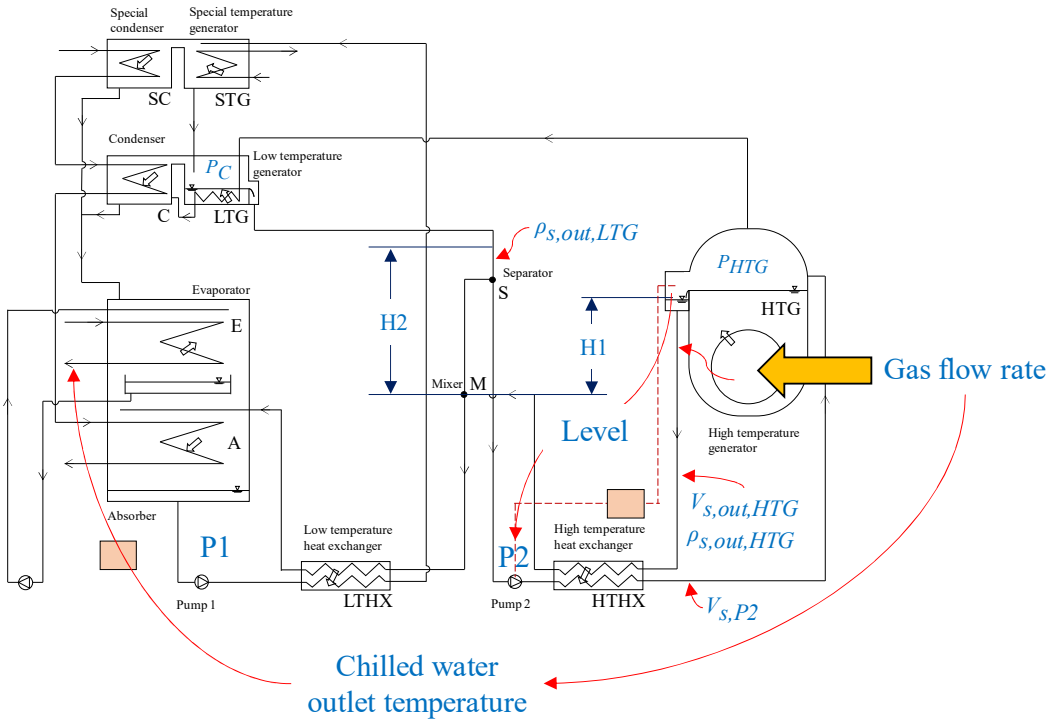

Fig. 7.2 SDE schematic diagram of the operation strategy

For this operation strategy, the total solution mass flow rate or the volumetric of the solution pump 1 is kept constant based on the results of Chapter 6 (Fig. 6.10(c)), because the flow rates are not so much different according to the hot water inlet temperature and the partial load. The flow rate of the cooling capacity of 100% ($V_{s,out,A}$ = *43.132* [l/min]) is chosen to be applied for this operation strategy to cover all the conditions.

7.2 Investigation of the suggested operation strategy

To evaluate the characteristics of the suggested operation strategy, this operation strategy is then simulated for the transient condition.

For the transient simulation of the suggested operation strategy, three internal parameters are controlled to satisfy the target chilled water outlet temperature. The three internal parameters are total volumetric solution flow rate, the solution level of the outlet high temperature generator, and the gas flow rate. The detailed explanation about this operation strategy refers to the subsection 7.1. Therefore, in this section only add information about the gas flow rate control.

The gas flow rate at the high temperature generator is controlled to satisfy the target chilled water outlet temperature. PID controller is then used to control the gas flow rate according to the

real machine. In general for the simulation, the mathematical equation of PID controller is written as follows:

$$u(t)= K_p e(t)+K_i \int_0^t e\, dt + K_d \frac{de(t)}{dt} \tag{7.2}$$

where K_p, K_i, and K_d are the coefficients for the proportional, integral, and derivative terms respectively. For the numerical simulation of the gas flow rate in this study, Eq. 7.2 is then modified becomes Eq. 7.3. Approximations for the first- and second-order derivatives are used backward finite differences.

$$V_{gas(i)}=V_{gas(i-1)}+\left(K_p+K_i\frac{\Delta t}{2}+\frac{K_d}{\Delta t}\right)e_{(i)}+\left(-K_p+K_i\frac{\Delta t}{2}-\frac{2K_d}{\Delta t}\right)e_{(i-1)}+\frac{K_d}{\Delta t}e_{(i-2)} \tag{7.3}$$

where index i introduces the time discrete parameters.

Due to the working direction between PID controller and the chilled water outlet temperature are opposite, the coefficient values of PID in this simulation is then given negative. The coefficient values of PID affect the calculation results directly. Therefore, the given coefficient values must be corrected. The PID calculation result gives directly the right gas flow rate with unit of m^3/s to the simulation. Thus, the PID coefficient values are small.

After several trial of calculation, this simulation only needs PI controller. The PI coefficient values K_p and K_i are $1e^{-5}$ and $1e^{-5}$ respectively. As noted, the focus of this study is not to discover the best PI controller. This PI controller is only the method to calculate the transient simulation to evaluate the operation strategy. But, in the future, it can be one of the focus of the study.

For the transient simulation, the initial condition is kept constant with the simulation conditions in Table 7.1. The initial condition is calculated for 6000 s to ensure that the system operates until reach the steady-state. Then, starting at 6001 s, the operation srtategy with the PID controller is used to satisfy the targeted chilled water outlet temperature at 7 ± 0.5 °C. In order to reduce calculation time but it is still reliable for the calculation, thus, the simulation time step is set 60 s.

Table 7.1 Initial conditions for the transient simulation

	Value	Unit
Chilled water inlet temp.	15	°C
Chilled water flow rate	25.7	m^3/h
Cooling water inlet temp.	32	°C
Cooling water flow rate	68	m^3/h
Hot water inlet temp.	90	°C
Hot water flow rate	7.8	m^3/h
Gas flow rate	5.4	m^3/h

Before the transient simulation using the suggested operation strategy and PI controller is simulated, the initial steady-state condition needs to be obtained. Therefore, at the first step of the calculation, the gas flow rate is kept constant at 5.4 m^3/h to ensure that all the parameters are already steady before the transient simulation starts (Fig. 7.3). From Fig. 7.3, it can be seen the transient of this system when the gas flow rate is adjusted by PI mathematical model to set the chilled water outlet temperature. However, the optimal PI values for this system is not the main focus of this chapter.

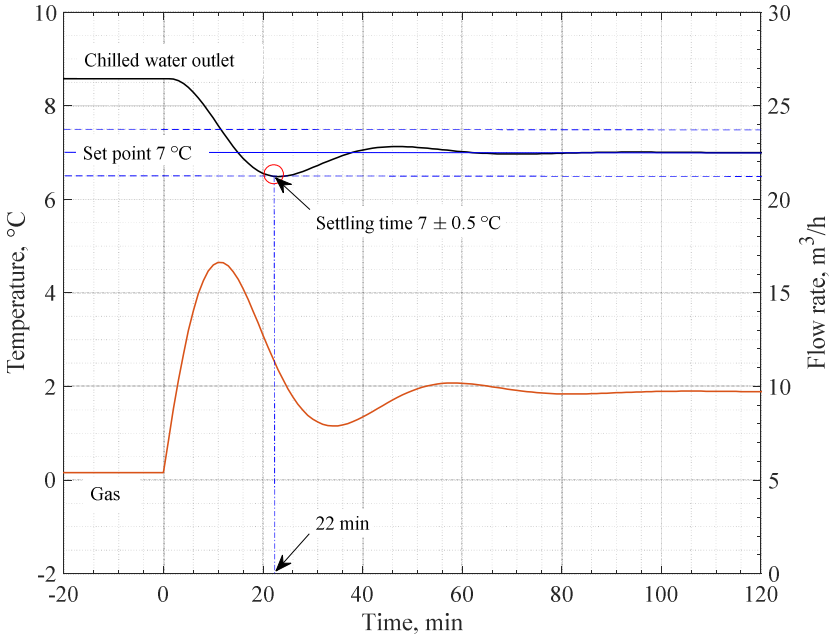

Fig. 7.3 Transient simulation of the suggested operation strategy (gas flow rate and chilled water outlet temperature)

PI controller adjusts the gas flow rate to alter the chilled water outlet temperature from 8.6 °C to 7 °C (set point). Concerning the accuracy of the temperature sensor, the steady state of the temperature can be reached when the set point temperature is ± 0.5 °C.

Based on Figs. 7.4 and 7.5, the suggested operation strategy is able to manipulate the gas flow rate and the solution pump 2 flow rate to generate the cooling capacity of 239 kW with the chilled water outlet temperature of 7 °C. The gas flow rate increases simultaneously from 5.4 m^3/h until get steady at 9.7 m^3/h to make the chilled water outlet temperature is around 7 °C ± 0.5 °C. At the same time, Eq. 7.1 (the solution level control) adjusts the solution flow rate of the solution pump 2 to maintain the solution level at the HTG. On the other hand, the solution flow rate of the solution pump 1 (total solution flow rate) is kept constant at 43.13 l/min.

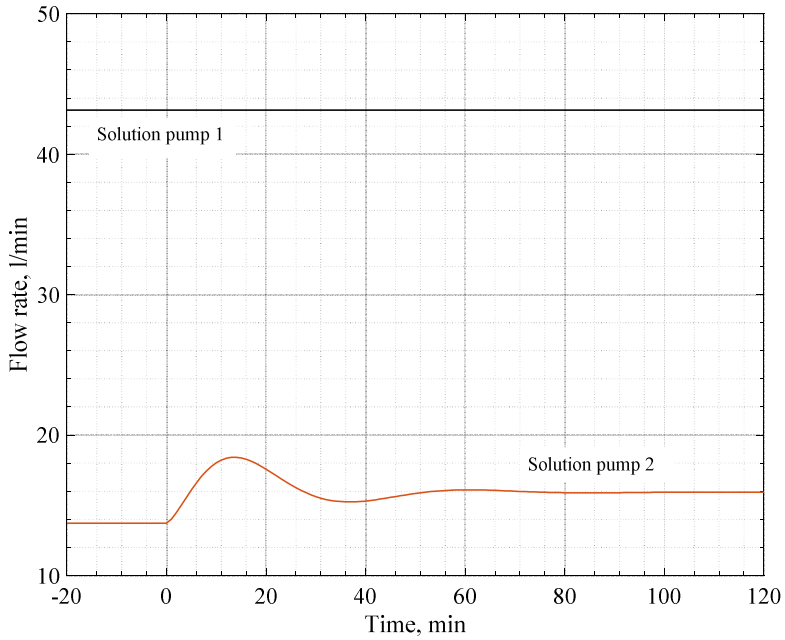

Fig. 7.4 Transient simulation of the suggested operation strategy (solution pump flow rate)

Figs. 7.5 – 7.11 show the simulated response of some internal and external variables from the suggested operation strategy such as: total mass of solution and refrigerant, pressure, solution concentration, solution temperature, water temperature, capacity, and COP.

In Fig. 7.5, it can be seen that the total mass between the solution (LiBr/water) and refrigerant (water) are balance, which means the simulation model works well. As seen in Fig. 7.5, the total mass of the solution decreases because the high-temperature generates more vapour (Fig. 7.10) to be sent to the evaporator to satisfy the target of the chilled water outlet temperature of 7 °C, therefore, the total mass of refrigerant increases and due to the mass balance equations, the total mass of solution decreases. The mass balance equations have connection between the solution concentrations, thus, when the total mass of refrigerant increases, which means the number of refrigerant in the solution decreases and the number of the LiBr increases, in the other word, the LiBr concentration increases, it can be seen in Fig. 7.7.

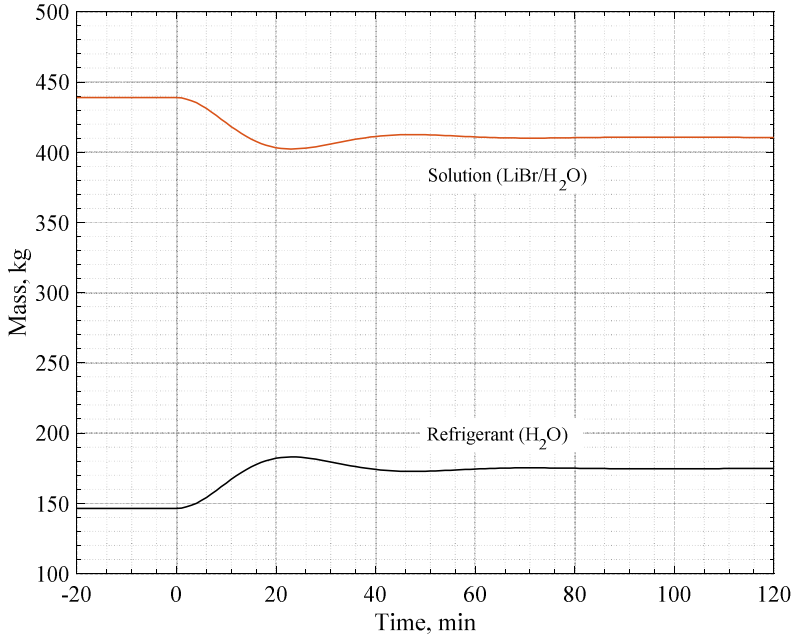

Fig. 7.5 Transient simulation of the suggested operation strategy (refrigerant and solution mass storage)

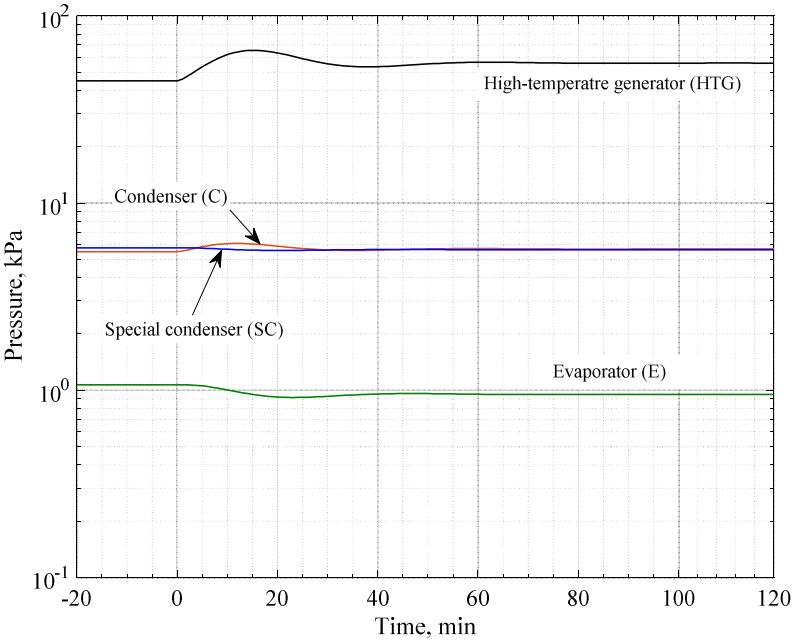

Fig. 7.6 Transient simulation of the suggested operation strategy (pressure)

The simulated response from the pressure is illustrated in Fig. 7.6. The pressure of the high-temperature generator and the condenser or low-temperature generator increase when the gas flow rate increase to the HTG in order to generate more vapour. Conversely, the pressure of the evaporator decreases, and also the special condenser decreases when the hot, cooling, and chilled water inlet temperature are constant. If the external sides change then the trend will be different.

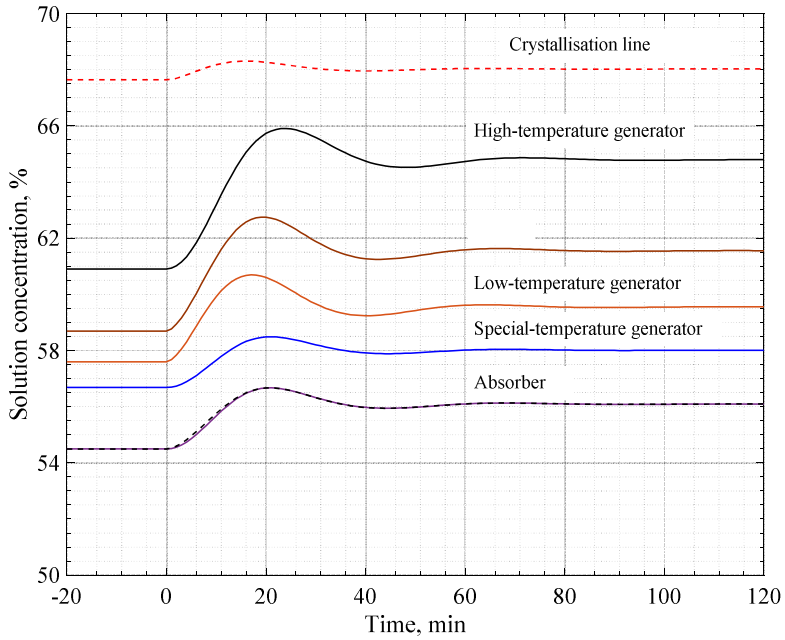

Fig. 7.7 Transient simulation of the suggested operation strategy (solution concentration)

This suggested operation strategy can enhance the performance of the single-double-effect absorption chiller and keep the strongest solution concentration under the crystallisation line (Fig. 7.7). In general, behavior of the solution concentration follows the heat input rules; when the heat input increases and the solution concentration also increases. The solution temperatures also have the same behavior as same as the solution concentration.

The input values and the simulation result of the external side of the absorption machine can be seen in Fig. 7.9. In this suggested operation strategy's investigation, the inlet temperature of the hot, cooling, and chilled water are kept constant of 90 °C, 32 °C, and 15 °C respectively. Therefore, decreasing the chilled water outlet temperature with constant inlet temperature input increase the outlet temperature of the cooling and hot water because the cooling water receives more heat, and the hot water releases less heat to the solution.

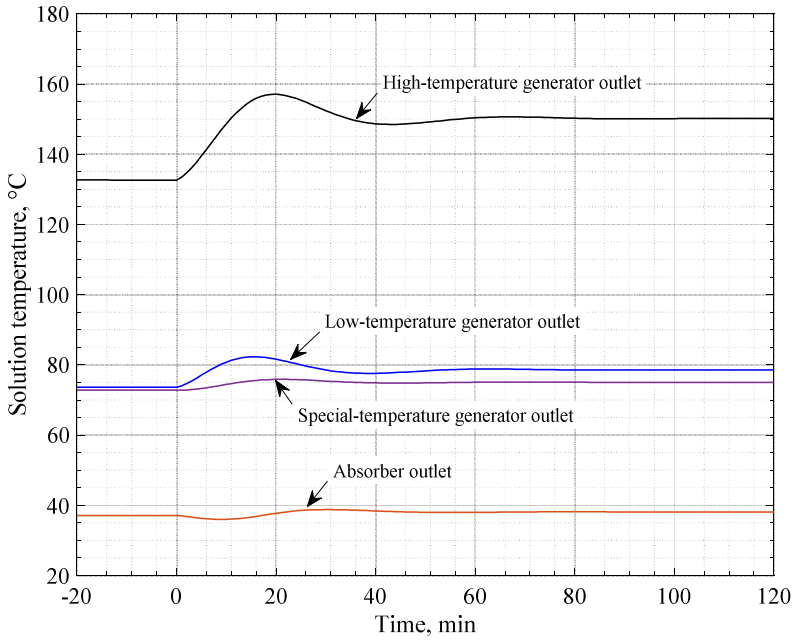

Fig. 7.8 Transient simulation of the suggested operation strategy (solution temperature)

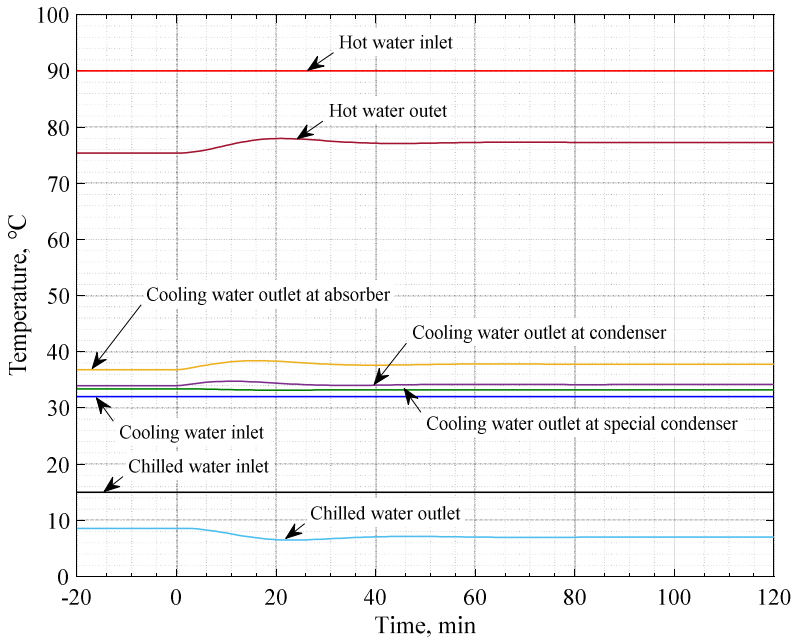

Fig. 7.9 Transient simulation of the suggested operation strategy (water temperature)

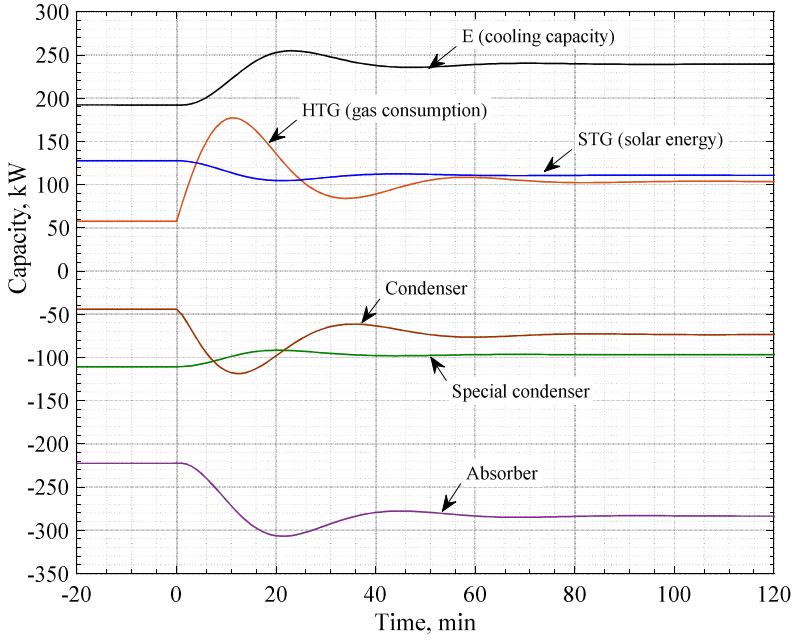

Fig. 7.10 Transient simulation of the suggested operation strategy (capacity)

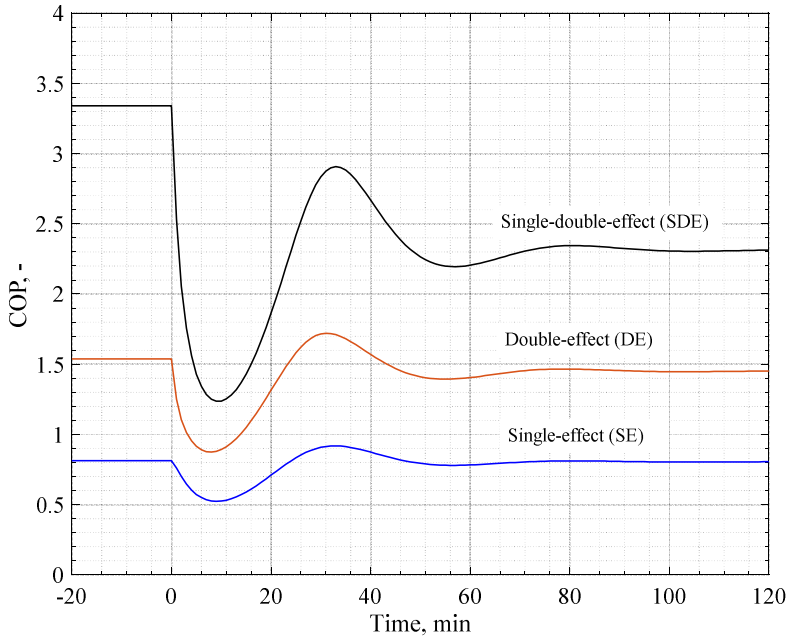

Fig. 7.11 Transient simulation of the suggested operation strategy (COP)

7.3 The performance result of the suggested operation strategy

After investigating the suggested operation strategy by transient simulation, then, in this section the suggested operation strategy is simulated by steady-state. For the steady state simulation, the cooling water inlet temperature follows Japanese Industrial Standard (JIS). Therefore, the cooling water inlet temperature at full load is 32 °C and at no load is 27 °C. Also, the gas volumetric flow rate is calculated by assuming that the chilled water outlet temperature is 7 °C.

When the cooling capacity is reduced, the COP of the suggested operation strategy increases any partial load operation. Comparing the COP of the suggested operation strategy with the maximum COP of Chapter 6, from 100% to 70% of the part load operation, the COP of the operation strategy deviates slightly, but at 60% of the part load, the COP of each operation strategy differs around 3%. From Fig. 7.12 it can be observed that the suggested operation strategy can reach the operation performance of the COP results maximisation method. Therefore, the suggested operation strategy is selected to drive the single-double-effect absorption chiller.

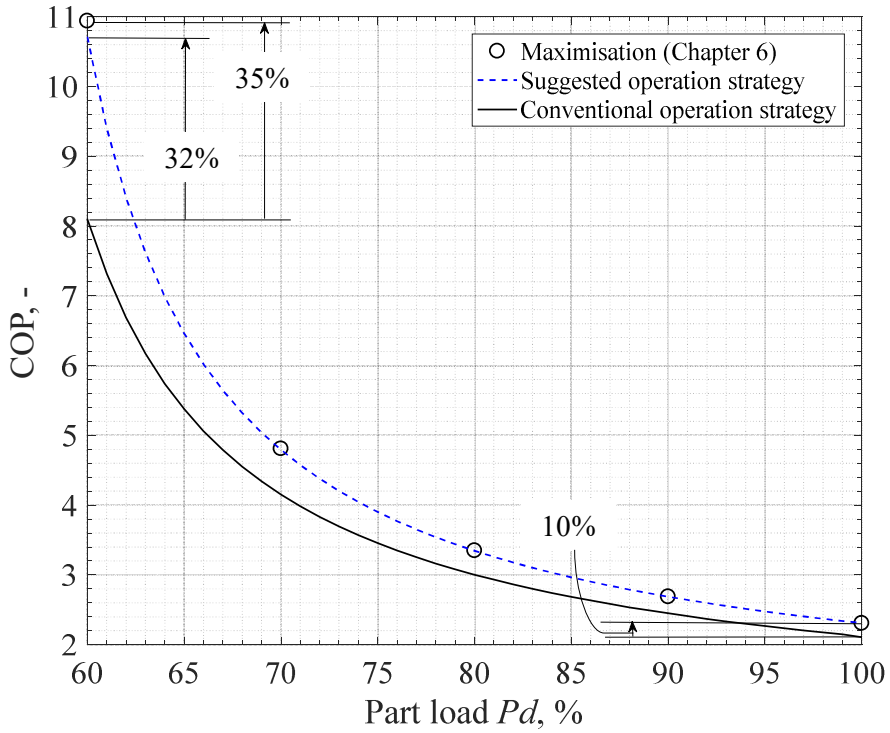

Fig. 7.12 COP of the suggested operation strategy, Chapter 6 result, and conventional operation strategy

Adopting the new flow rate of the solution pump 1 (from Chapter 6) and the new design point (solution level) of $Vo_{s,out,HTG}$, $\rho o_{s,out,HTG}$, and $(Po_{HTG} - Po_C)$ into the suggested operation strategy can enhance the COP up to 32% compared to the conventional operation strategy.

Therefore, this chapter suggests this operation strategy for the real application control of the single-double-effect absorption chiller.

Chapter 8
Conclusion

Based on the advantages associated with the use of a single-double-effect absorption cooling system, the construction of this system in the tropical climate of Asia is expected to be a promising solution for reducing the usage of non-renewable energy when the building area is limited, as well as for addressing the related energy problems and environmental issues.

Simulation results have been validated with experimental data and show good agreement. Therefore, the predicted performance of the system is explored for operative ranges of cooling water inlet temperatures and hot water inlet temperatures that are typical for tropical Asia climates. The simulation results show and explain that this system exhibits a good performance under tropical Asia climates. These results are particularly relevant to buildings in the tropical regions associated with high cooling loads and limited available areas for solar collectors. With cooling water inlet temperatures ranging from 28–34°C and hot water inlet temperatures ranging from 75–90°C, this system has a performance coefficient of approximately 1.4–2.91 and a gas reduction ratio of approximately 5–50.9%. The implementation of this system will be appropriate, especially in tropical Asia regions, because the solar energy can be utilised almost throughout the entire year, and this is expected to drastically reduce the operational cost compared to the conventional system of either the absorption chiller or the vapour compressor.

Furthermore, this thesis presented how the performance of a reference unit of single-double-effect absorption chiller is maximised by manipulating the distribution ratio and solution flow rate. The operation points at different cooling capacities have been investigated and compared with the conventional operation condition of this system. Strong solution concentration and pressure at the high-temperature generator have been considered in the simulation to keep that the operation safe from crystallisation and overpressure.

The new operation points can increase the actual operation COP approximately 5 to 7%. In addition, the performance enhancement of the double-effect side by using the new operation points is approximately 14–62%. Finally, the method is used to improve the operation performance of the single-double-effect absorption chiller at the University of Indonesia. It has been clarified that the performance of the actual system installed for the field test in the tropical area can be improved by the appropriate operation strategy. The operation performance increases by 17% compared to the average actual operation performance using conventional operation points. Eventually, the new operation points, Fig. 6.10, can be used as the reference for the suggested operation strategy.

The criterion followed to select the operation strategy for the single-double-effect absorption chiller, is that of minimising the primary energy consumption while being of easy applicability for the actual plant. Based on the results of Chapter 6, the operation strategy is focused on the control of the internal parameter. But then the solution level is chosen instead of the solution

distribution ratio because they actually have the same function to manage the solution amount entering the high temperature generator in order to minimise the fuel gas heat input. In actual condition, installing the level sensor for the signal of the solution pump 2 is simpler and cheaper to keep the solution level than using the flow meter to adjust the proper solution distribution ratio. The total solution mass flow rate or the volumetric of the solution pump 1 is kept constant based on the results of Chapter 6 (Fig. 6.10(c)), because the flow rates are not so much different according to the hot water inlet temperature and the partial load. Adopting the new flow rate of the solution pump 1 (from Chapter 6) and the new design point (solution level) of $Vo_{s,out,HTG}$, $\rho o_{s,out,HTG}$, and (Po_{HTG}-Po_C) into the suggested operation strategy can enhance the COP up to 32% compared to the conventional operation strategy.

Based on the results of Chapter 6, manipulating the total solution mass flow rate of the absorber (solution pump 1) and the solution distribution ratio (solution pump 2) according to the cooling capacity and the hot water inlet temperature are the best operation strategy to achieve the optimum operation performance. However, adopting this operation strategy to the real machine needs an important measuring device, namely mass flow meter, to set the right solution distribution ratio. As known, the price of the mass flow meter is expensive. Therefore, adopting the suggested operation strategy is the best option instead of the manipulating total solution mass flow rate and the solution distribution ratio, because adopting the suggested operation strategy does not need an expensive measuring device. Moreover, the suggested operation strategy can reach the operation performance of this system is near to the COP results of Chapter 6.

For the future research, the suggested operation strategy (in Chapter 7) will be adopted to the real single-double-effect absorption chiller machine. Then, this operation strategy will be compared with the conventional operation strategy by using the annual performance factor (APF) method.

References

Chapter 1

[1] Saber EM, Tham KW, Leibundgut H. A review of high-temperature cooling systems in tropical buildings. Build. Environ. 2016;96:237–249.

[2] Oh SJ, Ng KC, Thu K, Chun W, Chua KJE. Forecasting long-term electricity demand for cooling of Singapore's buildings incorporating an innovative air-conditioning technology. Energy Build. 2016;127:183–193.

[3] Alahmer A,Wang X, Al-Rbaihat R, Alam KCA, Saha, BB. Performance evaluation of a solar adsorption chiller under different climatic conditions. Appl Ener 2016;175: 293–304.

[4] https://solargis.info/imaps/#tl=GeoModel:t_yr_avg&c=0.117187,117.359095 January 30th, 2018

[5] M.H. Hasan, T.M.I. Mahlia, H. Nur, A review on energy scenario and sustainable energy in Indonesia, Renewable and Sustainable Energy Reviews 16 (2012) 2316–2328.

[6] H.C. Ong, T.M.I. Mahlia, H.H. Masjuki, A review on energy scenario and sustainable energy in Malaysia, Renewable and Sustainable Energy Reviews 15 (2011) 639–647.

[7] T. Jaruwongwittaya, G. Chen, A review: renewable energy with absorption chillers in Thailand, Renewable and Sustainable Energy Reviews 14 (2010) 1437–1444.

[8] S. Janjai, P. Pankaew, J. Laksanaboonsong, P. Kitichantaropas, Estimation of solar radiation over Cambodia from long-term satellite data, Renewable Energy 36 (2011) 1214–1220.

[9] Q. Zhao, P. Wang, L. Goel, Optimal PV panel tilt angel based on solar radiation prediction, IEEE 11th International Conference, Singapore, 2010, ISBN: 978-1-4244-5720-5.

[10] R. Mahtta, P.K. Joshi, A.K. Jindal, Solar power potential mapping in India using remote sensing inputs and environmental parameters, Renewable Energy 71 (2014) 255–262.

[11] https://solargis.com/products/maps-and-gis-data/download/world January 30th, 2018

[12] Jafarian M, Arjomandi M, Nathan GJ. A hybrid solar and chemical looping combustion system for solar thermal energy storage. Appl Ener 2013;103:671–678.

[13] Bakhtyar B, Sopian K, Sulaiman MY, Ahmad SA. Renewable energy in five South East Asian countries: Review on electricity consumption and economic growth. Renew Sustain Energy Rev 2013;26:506–514.

[14] Ahmed T, Mekhilef S, Shah R, Mithulananthan N, Seyedmahmoudian M, Horan B. ASEAN power grid: A secure transmission infrastructure for clean and sustainable energy for South-East Asia. Renew Sustain Energy Rev 2017;67:1420–1435.

[15] Choudhury B, Saha BB, Chatterjee PK, Sarkar JP. An overview of developments in adsorption refrigeration systems towards a sustainable way of cooling. Appl Energy 2013;104:554–567.

[16] Giannetti N, Rocchetti A, Saito K. Thermodynamic optimization of three-thermal irreversible systems. Int J Heat Technol 2016;34:S83–S90.

[17] Saito K, Inoue N, Nakagawa Y, Fukusumi Y, Yamada H, Irie T.Experimental and numerical performance evaluation of double-lift absorption heat transformer. Sci Technol Built Environ 2015;21:312–322.

[18] Lubis A, Giannetti N, Yamaguchi S, Saito K, Inoue N. Experimental performance of a double-lift absorption heat transformer for manufacturing-process steam generation, Energy Conver Manag 2017;148:267-278.

[19] Bataineh K, Taamneh Y. Review and recent improvements of solar sorption cooling systems. Energy Build 2016;128:22–37.

[20] Drosou V, Cosmopoulos P, Papadopoulos A. Solar cooling system using concentrating collectors for office buildings: A case study for Greece. Renew Energy 2016;97:697–708.

[21] Pongtornkulpanich A, Thepa S, Amornkitbamrung M, Butcher C. Experience with fully operational solar-driven 10-ton LiBr/H2O single-effect absorption cooling system in Thailand Renew Energy 2008;33:943–949.

[22] Bermejo P, Pino FJ, Rosa F. Solar absorption cooling plant in Seville. Solar Energy 2010;84:1503–1512.

[23] Hang Y, Qu M, Winstonc R, Jiang L, Widyolar B, Poiry H. Experimental based energy performance analysis and life cycle assessment for solar absorption cooling system at University of Californian, Merced. Energy Build 2014;82:746–757.

[24] Eicker U, Pietruschka D, Haag M, Schmitt A. Systematic design and analysis of solar thermal cooling systems in different climates. Renew Energy 2015;80:827–836.

[25] Hartmann N, Glueck C, Schmidt FP. Solar cooling for small office buildings: Comparison of solar thermal and photovoltaic options for two different European climates. Renew Energy 2011;36: 1329–1338.

[26] Hang Y, Qu M, Zhao F. Economical and environmental assessment of an optimized solar cooling system for a medium-sized benchmark office building in Los Angeles, California. Renew Energy 2011;36:648–658.

[27] Casals XG.Solar absorption cooling in Spain: Perspectives and outcomes from the simulation of recent installations. Renew Energy 2006;31:1371–1389.

[28] S. K. Wang, Handbook of air conditioning and refrigeration, McGraw-Hill. 2001. ISBN 0-07-068167-8.

[29] R. Gomri, Investigation of the potential of application of single effect and multiple effect absorption cooling systems, Energy Conversion and Management 51 (2010) 1629–1636.

[30] R. Gomri, Simulation study on the performance of solar/natural gas absorption cooling chillers, Energy Conversion and Management 65 (2013) 675–681.

[31] V. Boopathi Raja, V. Shanmugam, A review and new approach to minimize the cost of solar assisted absorption cooling system, Renewable and Sustainable Energy Reviews 16 (2012) 6725–6731.

[32] Ahmed Hamza H. Ali, Performance-cost and global warming assessments of two residential scale solar cooling systems versus a conventional one in hot arid areas, Sustainable Energy Technologies and Assessments 20 (2017) 1–8.

[33] Ming Li, Chengmu Xu, Reda Hassanien Emam Hassanien, Yongfeng Xu, Binwei Zhuang, Experimental investigation on the performance of a solar powered lithium bromide–water absorption cooling system, international journal of refrigeration 71 (2016) 46–59.

[34] J.F. Chen, Y.J. Dai, R.Z. Wang, Experimental and analytical study on an air-cooled single effect LiBr-H2O absorption chiller driven by evacuated glass tube solar collector for cooling application in residential buildings, Solar Energy 151 (2017) 110–118.

[35] E. Bellos, C. Tzivanidis, K.A. Antonopoulos, Exergetic, energetic and financial evaluation of a solar driven absorption cooling system with various collector types, Applied Thermal Engineering 102 (2016) 749–759.

[36] Nasiru I. Ibrahim, Fahad A. Al-Sulaiman , R. Saidur, Performance assessment of water production from solar cooling system in humid climate, Energy Conversion and Management 127 (2016) 647–655.

[37] Ming Li, C. Xu, R.H.E Hassanien, Y. Xu, B. Zhuang, Experimental investigation on the performance of a solar powered lithium bromide–water absorption cooling system, International Journal of Refrigeration 71 (2 0 1 6) 46–59.

[38] Ali Shirazi, Robert A. Taylor, Stephen D. White, Graham L. Morrison, A systematic parametric study and feasibility assessment of solar-assisted single-effect, double-effect, and triple-effect absorption chillers for heating and cooling applications, Energy Conversion and Management 114 (2016) 258–277.

[39] Felix Ziegler, State of the art in sorption heat pumping and cooling technologies, International Journal of Refrigeration 25 (2002) 450–459.

[40] Gianfranco Chico, Pierluigi Mancarella, Models and Indicators for Energy and CO2 Emission Assessment of Electric Chillers and Direct-Fired Absorption Chillers, 5th WSEAS Int. Conf. on ENVIRONMENT, ECOSYSTEMS and DEVELOPMENT, Tenerife, Spain, December 14-16, 2007.

[41] Mehmet Efe Biresselioglu, Tezer Yelkenci, Ibrahim Onur Oz, Investigating the natural gas supply security: A new perspective, Energy 80 (2015) 168–176.

[42] Mario Martín-Gamboa, Diego Iribarren, Javier Dufour, Environmental impact efficiency of natural gas combined cycle power plants: A combined life cycle assessment and dynamic data envelopment analysis approach, Science of the Total Environment 615 (2018) 29–37.

[43] Zeyu Li, Xiangyang Ye, Jinping Liu, Performance analysis of solar air cooled double effect LiBr/H2O absorption cooling system in subtropical city, Energy Conversion and Management 85 (2014) 302–312.

[44] Z.S. Lu, R.Z. Wang, Experimental performance investigation of small solar air-conditioning systems with different kinds of collectors and chillers, Solar Energy 110 (2014) 7–14.

[45] Lingyu Zhou, Xian Li, Yao Zhao, Yanjun Dai, Performance assessment of a single/double hybrid effect absorption cooling system driven by linear Fresnel solar collectors with latent thermal storage, Solar Energy 151 (2017) 82–94.

Chapter 2

[46] IIR Information. Solar Cooling. 34th Informatory Note on Refrigeration Technologies/April 2017.

[47] Kimijima S, Waragai S, Uekasa T, Kanao M, Kawai S. Characteristics of single/double-effect combination absorption refrigerator driven by steam and hot water, 3rd Report: Study on high efficiency operation by absorbent flow rate control. Trans JAR 1998;15(1):85–96.

[48] Saito K, Sugano N, Nishiyama N, Homma R, Wakimizu H. Studies on the characteristics of absorption refrigerator driven by two different heat sources (1st Report, Hot Water and Steam). Trans JAR 1994;60(573):250–257.

Chapter 3

[49] R. Cabello, E. Torella, J. Navarro-Esbri, Experimental evaluation of a vapour compression plant performance using R134a, R407C and R22 as working fluids, Applied Thermal Engineering, 24 (2004) 1905–1917.

[50] J. Navarro-Esbri, J.M. Mendoza-Miranda, A. Mota-Babiloni, A. Baragan-Cervera, J.M. Belman-Flores, Experimental analysis of R1234yf as a drop-in replacement for R134a in a vapor compression system, International Journal of Refrigeration 36 (2013) 870–880.

[51] Akhilesh Arora, S.C. Kaushik, Theoretical analysis of a vapour compression refrigeration system with R502, R404A and R507A, International Journal of Refrigeration, 31 (2008) 998–1005.

Chapter 4

[52] Keith E. Herold, Reinhard Radermacher, Sanford A. Klein. (2016). Absorption chillers and heat pumps (second edition). Boca Raton, CRC Press: Taylor & Francis Group.

[53] P. Kohlenbach, F. Ziegler. A dynamic simulation model for transient absorption chiller performance. Part I: The model. International Journal of Refrigeration 31 (2008) 217–225.

[54] P. Kohlenbach, F. Ziegler. A dynamic simulation model for transient absorption chiller performance. Part I: Numerical results and experimental verification. International Journal of Refrigeration 31 (2008) 226–233.

[55] 古川,佐々木,金子,野瀬渓：吸収冷温水機の吸収器用伝熱促進管_冷論 Vol.10,No.2(1993)

[56] 高橋，佐伯：吸収式蒸発器用伝熱管(エンドクロス)の伝熱性能，神戸製鋼技報/Vol. 54 No. 1（Apr. 2004）

[57] 藤井，小田. 水平管群を流れる低圧水蒸気の膜状凝縮熱伝達，機論 Vol.48　No.436(1982)

[58] 西山 et al. 水平管型硫化液膜式再生器の伝熱性能に関する研究_空調衛生講演論文集(1974)

[59] 梶井,八橋,大田. ソーラー吸収冷温水機の開発_冷論 Vol.28, No.3(2011)

[60] Traviss et al. Forced-Convection Condensation inside Tubes_MIT DSR72591-74 (1971)

[61] 植田，井上_管内蒸気流の凝縮熱伝達_機論 Vol.43No.365 (1977)

[62] 藤井，本田，野津：フロン系冷媒の水平管内凝縮_冷凍 Vol.55, No.627 (1980)

[63] 岡田 et al.：新しいプレート型熱交換器の試作とその伝熱特性,化学工学 Vol.35_No.5(1971)

[64] Zahid H. Ayub. Plate Heat Exchanger Literature Survay _Heat Transfer Engineering 24(5)_2003

[65] R. Kajii, H. Yabase, M. Ohta, Development of solar absorption chillers-heaters, Transactions of the JSRAE 28(3) (2011) 249–256.

Chapter 5

[66] M.Z.A.A. Kadir, Y. Rafeeu, A review on factors for maximizing solar fraction under wet climate environment in Malaysia, Renewable and Sustainable Energy Reviews 14 (2010) 2243–2248.

[67] M. Balghouthi, M.H. Chahbani, A. Guizani, Investigation of a solar cooling installation in Tunisia, Applied Energy 98 (2012) 138–148.

[68] O. Marc, F. Lucas, F. Sinama, E. Monceyron, Experimental investigation of a solar cooling absorption system operating without any backup system under tropical climate, Energy and Buildings 42 (2010) 774–782.

[69] P. Bermejo, F.J. Pino, F. Rosa, Solar absorption cooling plant in Seville, Solar Energy 84 (2010) 1503–1512.

[70] Y. Hyodo, Solar absorption chillers using solar heat for cooling of Kawasaki thermal engineering Co., Ltd, Clean Energy 20(3) (2011) 5–9.

[71] A. Allouhi, T. Kousksou, A. Jamil, P. Bruel, Y. Mourad, Y. Zeraouli, Solar driven cooling system: an update review, Renew. Sustain. Energy Rev. 44 (2015) 159–181.

Chapter 6

[72] ASHRAE. ASHRAE handbook fundamental. Atlanta: ASHRAE.

[73] 1980 SI the Japan Society of Mechanical Engineers Steam Table.

Chapter 7

[74] Tsekouras PD, Drosou V, Antonopoulos KA, Karytsas CS. An innovative high solar fraction heating and cooling plant in Athens – Control strategy and initial measurements. Proc. ASME 2012 Summer Heat Transf Conf., Rio Grande.

[75] Labus J, Korolija I, Marjanovic-Halburd L, Zhang Y, Coronas A. ANN application to modelling and control of small absorption chillers. Proceedings of the First Building Simulation and Optimization Conference 2012, Loughborough.

[76] Liaoa X, Radermacher R. Absorption chiller crystallization control strategies for integrated cooling heating and power systems. Int J Refrig 2007;30:904–911.

[77] Bujedo LA, Rodrı´guez J, Martı´nez PJ. Experimental results of different control strategies in a solar air-conditioning system at part load. Sol Energy 2011;85:1302–1315.

[78] Albers J. New absorption chiller and control strategy for the solar assisted cooling system at the German federal environment agency. Int J Refrig 39 (2014) 48–56.

[79] Nienborg B, Dalibard A, Schnabel L, Eicker U. Approaches for the optimized control of solar thermally driven cooling systems. Appl Energy 2017;185:732–744.

[80] Kühn A, Ciganda JLC, Ziegler F. Comparison of control strategies of solar absorption chillers. Proceedings of the 1st International Congress on heating cooling and buildings, Eurosun.

[81] Shirazi A, Pintaldi S, White SD, Morrison GL, Rosengarten G, Taylor RA. Solar-assisted absorption air-conditioning systems in buildings: Control strategies and operational modes. Appl Therm Eng 2016;92:246–260.

[82] Verda V, Baccino G, Pizzuti S. Control strategy for the optimal operation of a solar cooling installation, Proceedings of the ASME 2012 11th Biennial Conference on Engineering Systems Design and Analysis, Nantes.

[83] Labusa J, Hernández JA, Brunoa JC, Coronas A. Inverse neural network based control strategy for absorption chillers. Renew Energy 2012;39:471–482.

[84] Giannetti N, Rocchetti A, Yamaguchi S, Saito K. Analytical solution of film mass-transfer on a partially wetted absorber tube. Int J Therm Sci 2017;118:176-186.

[85] Giannetti N, Rocchetti A, Yamaguchi S, Saito K. Heat and mass transfer coefficients of falling-film absorption on a partially wetted horizontal tube. Int J Therm Sci 2018;126:56-66.

[86] Giannetti N, Rocchetti A, Lubis A, Saito K, Yamaguchi S. Entropy parameters for falling film absorber optimization. Appl Therm Eng 2016;93:750–762.

[87] Fernandez-Seara J, Vazquez M. Study and control of the optimal generation temperature in NH3-H2O absorption refrigeration systems. Appl Therm Eng 2001;21:343–357.

[88] Xu Y-J, Zhang S-J, Xiao Y-H, Modeling the dynamic simulation and control of a single effect LiBr–H2O absorption chiller. Appl Therm Eng 2016;107: 1183–1191.

[89] Seo JA, Shin Y, Chung JD. Dynamics and control of solution levels in a high temperature generator for an absorption chiller. Int J Refrig 2012;35:1123–1129.

[90] Shin Y, Seo JA, Cho HW, Nam SC, Jeong JH. Simulation of dynamics and control of a double-effect LiBr–H2O absorption chiller. Appl Therm Eng 2009;29:2718–2725.

APPENDIX

Appendix 1 Initial, constant and assumptions

Table A 1.1 Initial parameter for the steady-state simulation

No.	Initial	Unit	Description
1	$X_{s,A}$	-	Solution concentration of absorber outlet
2	$T_{cw,A}$	°C	Cooling water temperature of absorber outlet
3	$\dot{m}_{v,A}$	kg/s	Vapour refrigerant mass flow rate
4	$T_{sat,E}$	°C	Saturation temperature in evaporator
5	$T_{s,out,A}$	°C	Solution temperature of absorber outlet
6	$T_{ss,out,LHX}$	°C	Strong solution temperature of low-temperature heat exchanger outlet
7	$T_{ws,out,LHX}$	°C	Weak solution temperature of low-temperature heat exchanger outlet
8	$T_{chw,out}$	°C	Chilled water outlet temperature
9	$\dot{m}_{r,out,M1}$	kg/s	Liquid refrigerant mass flow rate of mixer 1 outlet
10	$h_{r,out,M1}$	kJ/kg	Liquid refrigerant enthalpy of mixer 1 outlet
11	$\dot{m}_{r,out,M2}$	kg/s	Liquid refrigerant mass flow rate of mixer 2 outlet
12	$h_{r,out,M2}$	kJ/kg	Liquid refrigerant enthalpy of mixer 2 outlet
13	$\dot{m}_{s,out,LTG}$	kg/s	Solution mass flow rate of low temperature generator outlet
14	$X_{s,LTG}$	-	Solution concentration of low temperature generator outlet
15	$\dot{m}_{r,out,LTG}$	kg/s	Liquid refrigerant mass flow rate of condenser outlet
16	$T_{sat,C}$	°C	Saturation temperature in condenser
17	$T_{cw,C}$	°C	Cooling water temperature of condenser outlet
18	$T_{s,out,LTG}$	°C	Solution temperature of low temperature generator outlet
19	$T_{s,inside,LTG}$	°C	Solution temperature of low temperature generator inside
20	$T_{sh,LTG}$	°C	Superheat temperature in low temperature generator
21	$\dot{m}_{s,out,STG}$	kg/s	Solution mass flow rate of special temperature generator outlet
22	$X_{s,STG}$	-	Solution concentration of special temperature generator outlet
23	$\dot{m}_{r,out,STG}$	kg/s	Liquid refrigerant mass flow rate of special condenser outlet
24	$T_{sat,SC}$	°C	Saturation temperature in special condenser
25	$T_{cw,SC}$	°C	Cooling water temperature of special condenser outlet
26	$T_{s,out,STG}$	°C	Solution temperature of special temperature generator outlet
27	$T_{s,inside,STG}$	°C	Solution temperature of special temperature generator inside

28	$T_{sh,STG}$	°C	Superheat temperature in special temperature generator
29	$\dot{m}_{s,out,M}$	kg/s	Solution mass flow rate of mixer outlet
30	$X_{s,M}$	-	Solution concentration of mixer outlet
31	$h_{r,out,M}$	kJ/kg	Solution enthalpy of mixer outlet
32	$\dot{m}_{s,out,S}$	kg/s	Solution mass flow rate of separator outlet
33	$\dot{m}_{s,out,HTG}$	kg/s	Solution mass flow rate of high temperature generator outlet
34	$X_{s,HTG}$	-	Solution concentration of high temperature generator outlet
35	$T_{s,out,HTG}$	°C	Solution temperature of high temperature generator outlet
36	$\dot{m}_{r,out,HTG}$	kg/s	Liquid refrigerant mass flow rate of low temperature generator outlet
37	$T_{sh,HTG}$	°C	Superheat temperature in high temperature generator
38	$T_{s,inside,HTG}$	°C	Solution temperature of high temperature generator inside
39	$T_{sat,HTG}$	°C	Saturation temperature of low temperature generator outlet
40	$T_{ss,out,HHX}$	°C	Strong solution temperature of high -temperature heat exchanger outlet
41	$T_{ws,out,HHX}$	°C	Weak solution temperature of high -temperature heat exchanger outlet

Table A 1.2 Initial parameter for the dynamic simulation

No.	Initial	Unit	Description
1	$\dot{m}_{s,tb,A}$	kg/s	Solution mass flow rate of absorber tube bundle outlet
2	$X_{s,tb,A}$	-	Solution concentration of absorber tube bundle outlet
3	$X_{s,A}$	-	Solution concentration of absorber outlet
4	$T_{cw,A}$	°C	Cooling water temperature of absorber outlet
5	$M_{s,A}$	kg	Total solution storage in absorber
6	$T_{sat,E}$	°C	Saturation temperature in evaporator
7	$\dot{m}_{v,A}$	kg/s	Vapour refrigerant mass flow rate
8	$M_{r,E}$	kg	Total liquid refrigerant storage in evaporator
9	$\dot{m}_{r,E}$	kg/s	Liquid refrigerant mass flow rate of evaporator tube bundle outlet to the storage
10	$T_{s,out,tb,A}$	°C	Solution temperature of absorber tube bundle outlet
11	$T_{s,out,A}$	°C	Solution temperature of absorber outlet
12	$T_{s,inside,A}$	°C	Solution temperature of absorber inside
13	$T_{ss,out,LHX}$	°C	Strong solution temperature of low-temperature heat exchanger outlet
14	$T_{ws,out,LHX}$	°C	Weak solution temperature of low-temperature heat exchanger outlet
15	$T_{chw,out}$	°C	Chilled water outlet temperature
16	$h_{r,out,E}$	kJ/kg	Refrigerant storage enthalpy in evaporator
17	$\dot{m}_{r,out,M1}$	kg/s	Liquid refrigerant mass flow rate of mixer 1 outlet
18	$h_{r,out,M1}$	kJ/kg	Liquid refrigerant enthalpy of mixer 1 outlet
19	$\dot{m}_{r,out,M2}$	kg/s	Liquid refrigerant mass flow rate of mixer 2 outlet
20	$h_{r,out,M2}$	kJ/kg	Liquid refrigerant enthalpy of mixer 2 outlet
21	$\dot{m}_{s,out,LTG}$	kg/s	Solution mass flow rate of low temperature generator outlet
22	$X_{s,LTG}$	-	Solution concentration of low temperature generator outlet
23	$\dot{m}_{r,out,LTG}$	kg/s	Liquid refrigerant mass flow rate of condenser outlet
24	$T_{sat,C}$	°C	Saturation temperature in condenser
25	$T_{cw,C}$	°C	Cooling water temperature of condenser outlet
26	$T_{s,out,LTG}$	°C	Solution temperature of low temperature generator outlet
27	$T_{s,inside,LTG}$	°C	Solution temperature of low temperature generator inside
28	$T_{sh,LTG}$	°C	Superheat temperature in low temperature generator
29	$\dot{m}_{s,out,STG}$	kg/s	Solution mass flow rate of special temperature generator outlet
30	$X_{s,STG}$	-	Solution concentration of special temperature generator outlet
31	$\dot{m}_{r,out,STG}$	kg/s	Liquid refrigerant mass flow rate of special condenser outlet

32	$T_{sat,SC}$	°C	Saturation temperature in special condenser
33	$T_{cw,SC}$	°C	Cooling water temperature of special condenser outlet
34	$T_{s,out,STG}$	°C	Solution temperature of special temperature generator outlet
35	$T_{s,inside,STG}$	°C	Solution temperature of special temperature generator inside
36	$T_{sh,STG}$	°C	Superheat temperature in special temperature generator
37	$\dot{m}_{s,out,M}$	kg/s	Solution mass flow rate of mixer outlet
38	$X_{s,M}$	-	Solution concentration of mixer outlet
39	$h_{r,out,M}$	kJ/kg	Solution enthalpy of mixer outlet
40	$\dot{m}_{s,out,S}$	kg/s	Solution mass flow rate of separator outlet
41	$\dot{m}_{s,out,HTG}$	kg/s	Solution mass flow rate of high temperature generator outlet
42	$X_{s,HTG}$	-	Solution concentration of high temperature generator outlet
43	$T_{s,out,HTG}$	°C	Solution temperature of high temperature generator outlet
44	$\dot{m}_{r,out,HTG}$	kg/s	Liquid refrigerant mass flow rate of low temperature generator outlet
45	$T_{sh,HTG}$	°C	Superheat temperature in high temperature generator
46	$T_{s,inside,HTG}$	°C	Solution temperature of high temperature generator inside
47	$T_{sat,HTG}$	°C	Saturation temperature of low temperature generator outlet
48	$T_{ss,out,HHX}$	°C	Strong solution temperature of high -temperature heat exchanger outlet
49	$T_{ws,out,HHX}$	°C	Weak solution temperature of high -temperature heat exchanger outlet

Table A 1.3 Constant parameters of the dynamic model

No.	Initial	Unit	Value	Description
1	$A_{btm,A}$	m^2	1.4726	Bottom area of absorber
2	$A_{btm,E}$	m^2	1.0547	Bottom area of evaporator
3	$V_{chw,E}$	m^3	0.0976	Total chilled water volume in evaporator
4	$V_{cw,A}$	m^3	0.1906	Total cooling water volume in absorber
5	$V_{cw,C}$	m^3	0.0438	Total cooling water volume in condenser
6	$V_{cw,SC}$	m^3	0.0516	Total cooling water volume in special condenser
7	V_{hw}	m^3	0.0445	Total hot water volume in special temperature generator
8	$V_{s,LTG}$	m^3	0.0333	Total solution volume in low temperature generator
9	$V_{s,HTG}$	m^3	0.1960	Total solution volume in high temperature generator
10	$C_{p,mildsteel}$	kJ/kgK	0.5110	Specific heat of mild steel
11	$C_{p,copper}$	kJ/kgK	0.3768	Specific heat of copper
12	P_{hw}	kPa	101.325	Hot water pressure
13	P_{cw}	kPa	101.325	Cooling water pressure
14	P_{chw}	kPa	101.325	Chilled water pressure
15	$\dot{m}_{r,out,E}$	Kg/s	0.5	Refrigerant mass flow rate from the sump to the tube bundle in evaporator
16	γ	-	0.5	Solution distribution ratio
17	VF_{hw}	m^3/h	7.8	Hot water volumetric flow rate
18	VF_{cw}	m^3/h	68	Cooling water volumetric flow rate
19	VF_{chw}	m^3/h	25.7	Chilled water volumetric flow rate
20	LHV	kJ/m^3	38,360	Lower heating value (Universitas Indonesia)

Table A 1.4 Assumed heat capacities for each component

	$MC_{p,sol,A}$	$MC_{p,r,E}$	$MC_{p,s,LTG}$	$MC_{p,s,HTG}$	$MC_{p,ss,LHX}$	$MC_{p,ws,LHX}$	$MC_{p,ss,HHX}$	$MC_{p,ws,HHX}$
	(kJ/K)	(kJ/K)	(kJ/K)	(kJ/K)	(kJ/K)	(kJ/K)	(kJ/K)	(kJ/K)
100%	174	180	80	264	74	74	74	74
50%	87	90	40	132	37	37	37	37
0%	0	0	0	0	0	0	0	0

	$MC_{p,cw,A}$	$MC_{p,cw,E}$	$MC_{p,cw,C}$	$MC_{p,hw}$	$MC_{p,cw,SC}$
	(kJ/K)	(kJ/K)	(kJ/K)	(kJ/K)	(kJ/K)
100%	186	182	140	208	210
50%	93	91	70	104	105
0%	0	0	0	0	0

Appendix 2 Technical data of solar cooling system

A. 2.1 Storage tank

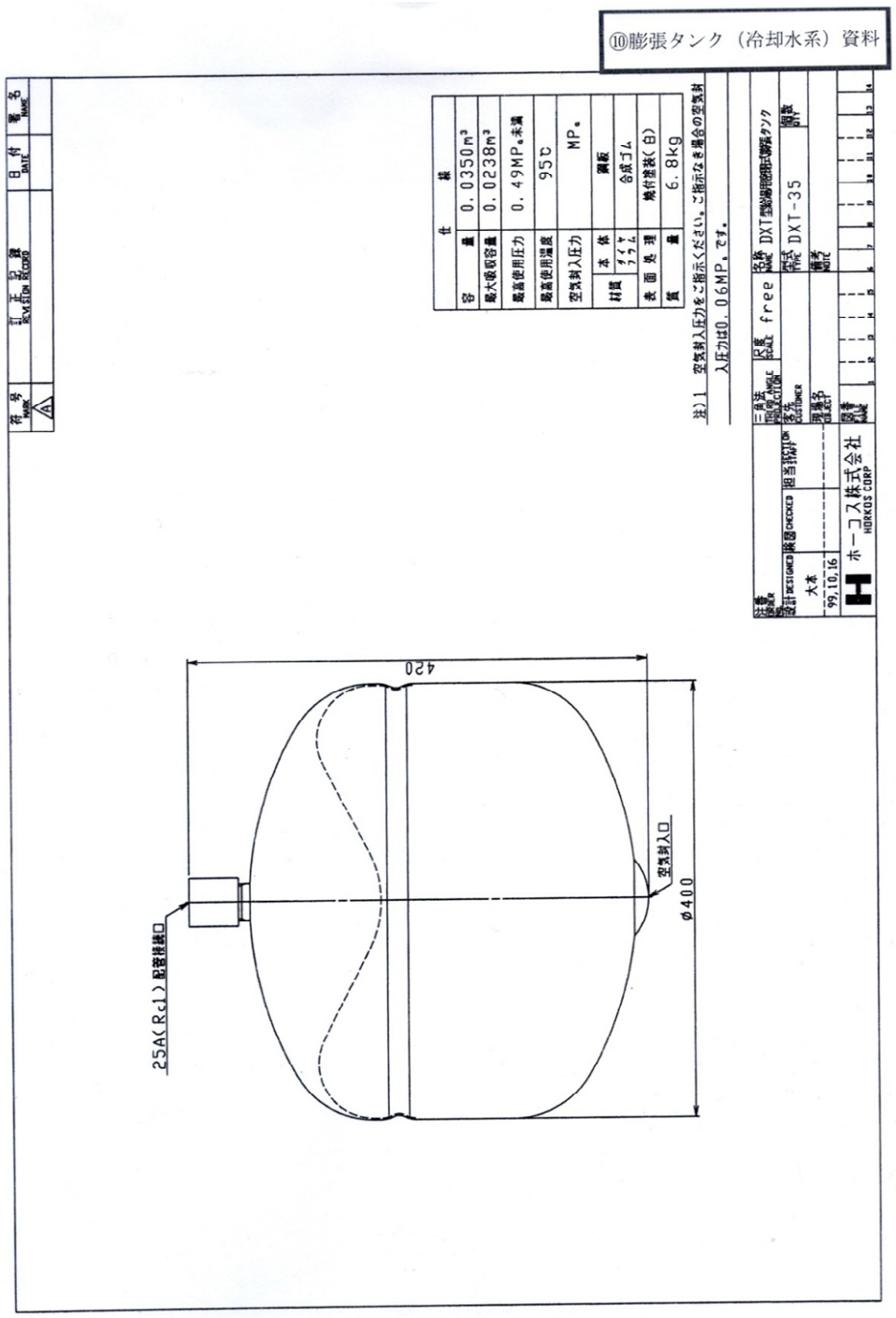

A. 2.2 Solar collector

②ソーラーパネル資料

清华阳光 TSINGHUA SOLAR

SLU Series Solar Collector

Description

SLU series is an all-glass evacuated tubular collector with metal U tubes.

SPECIFICATIONS			
MODELS		SLU-1500/12	SLU-1500/16
Tube		SL-I-1500	SL-I-1500
Number of tubes		12	16
U Tube	material	copper	
	diameter,mm	8 mm	
	thickness, mm	1 mm	
Aperture area, m2		1.09 m2	1.44 m2
Efficiency (η_0)		0.616	0.616
Heat loss (a_1)		1.293 W/(m^2K)	1.293 W/(m^2K)
Net weight		30 kg	45kg
Reflector		Flat plate diffuse	
Max. Pressure		0.6 MPa	
Inlet/outlet connections		1/2"	3/4"
Stagnation temp.(with reflector)		220℃	

Operational Principle

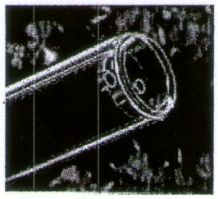

The selective coating on the inner cover of the evacuated tubes ensures high energy absorption and low heat radiance loss, which converts solar energy into heat energy and transfers heat to metal U tube by an aluminum fin. The liquid (anti-freezing liquid or purified water) in the metal U tube is heated, and conducts the heat energy to the water inside the storage tank through plate exchanger or internal spiral coils.

- Utilization all year round even in cold climates;
- Can operate with water pressure up to 0.6MPa;
- Annual heat gain 576 kWh/m^2 (tested in ITW-Stuggart, Germany);
- The collector will still operate in the event of occasional tube breakages;
- Modular system means easy handling, installation and can be extended to cover larger areas;
- Easy to install on roofs, balconies or façades;
- Can be combined with existing energy source;
- Quasi-tracking in all seasons.
- The diffuse flat plate reflector unit behind the glass tubes can be easily assembled and increase efficiency by 5%;

9

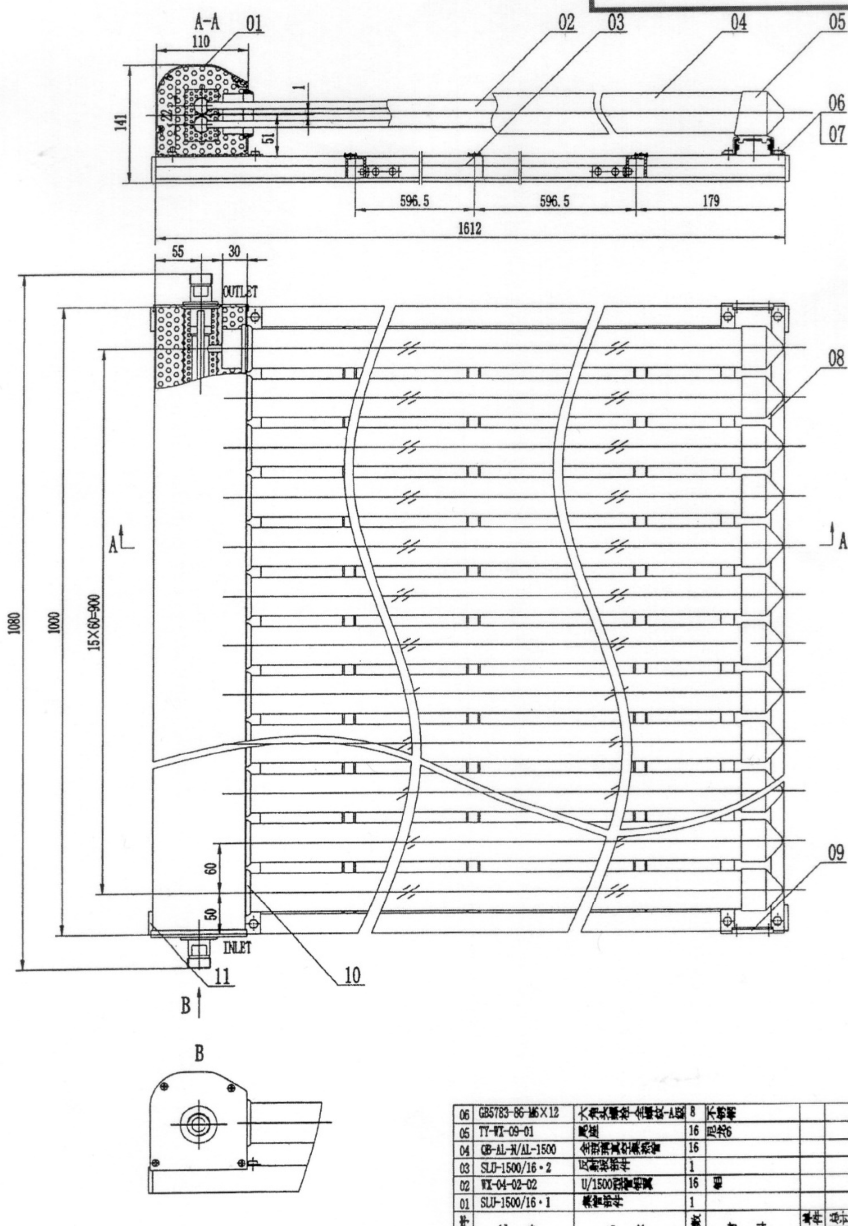

06	GB5783-86-M6×12	六角头螺栓-全螺纹-A级	8	不锈钢			
05	TY-WX-09-01	尾座	16	尼龙6			
04	GB-AL-N/AL-1500	[illegible]	16				
03	SLU-1500/16・2	反射板部件	1				
02	WX-04-02-02	U/1500[illegible]	16	铝			
01	SLU-1500/16・1	集管部件	1				
序号	代号	名称	数量	材料	单件 重量	总计 重量	备注

11	WX-06-02-06	U[illegible]	4	[illegible](黑色)			
10	WX-06-01-02	集热器挡风圈	16	硅橡胶			
09	WX-06-01-04	[illegible]	2	尼龙6			
08	SLU-1500/16-01	尾架	1	6063T5			
07	GB6170-86-M6	1型六角螺母-A和B级	8	不锈钢			
序号	代号	名称	数量	材料	单件 重量	总计 重量	备注

标记	处数	分区	更改文件号	签名	年,月,日	数量	1 台
设计	[illegible]	03.04.15	标准化			阶段标记 / 重量 / 比例	
制图	[illegible]	03.11.05				1:4	
审核						共 张 第 张	
工艺			批准				

清华阳光太阳能设备有限责任公司

U型管总装图

SLU-1500/16・0

A. 2.3 Cooling tower

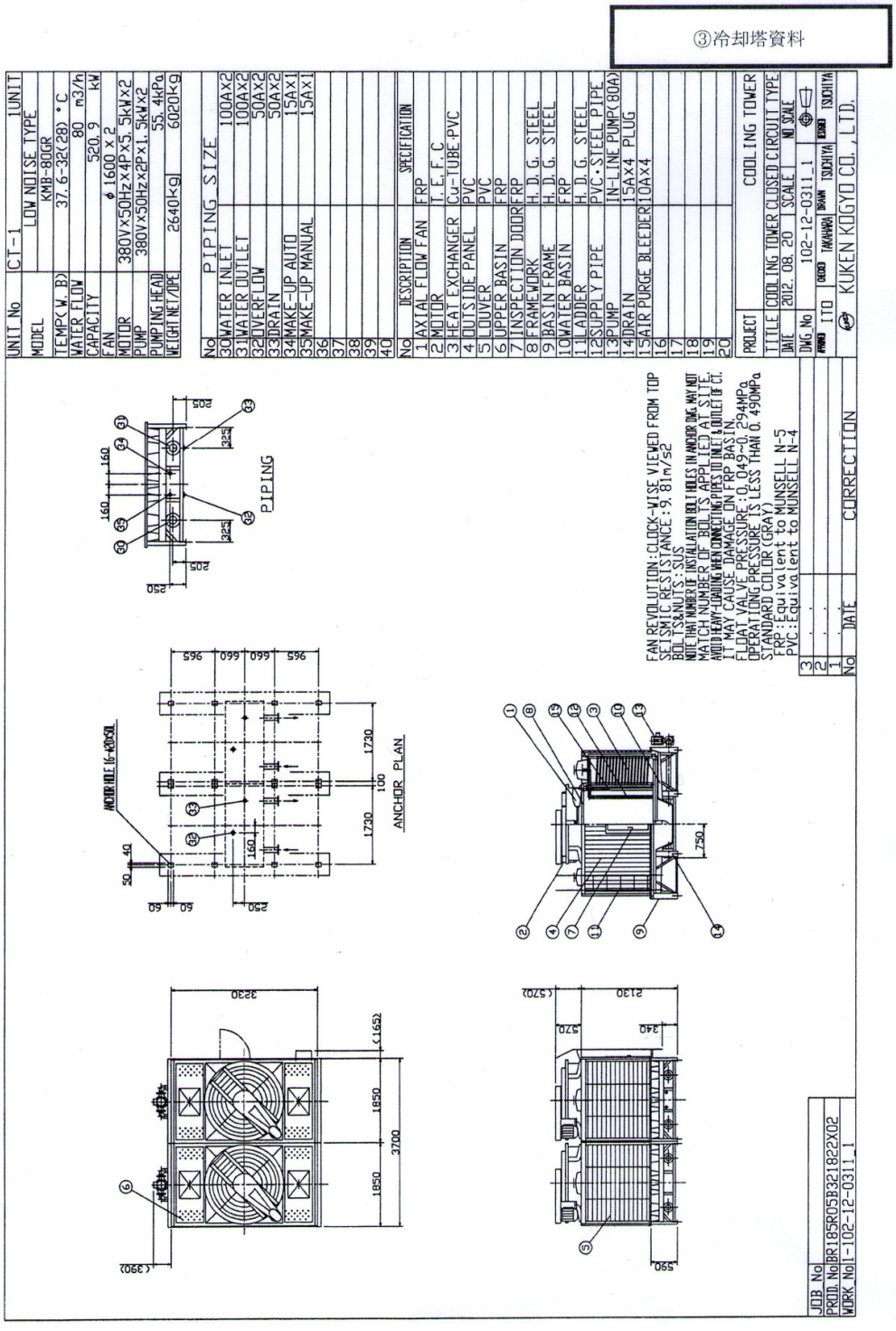

A. 2.4 Layout solar collector

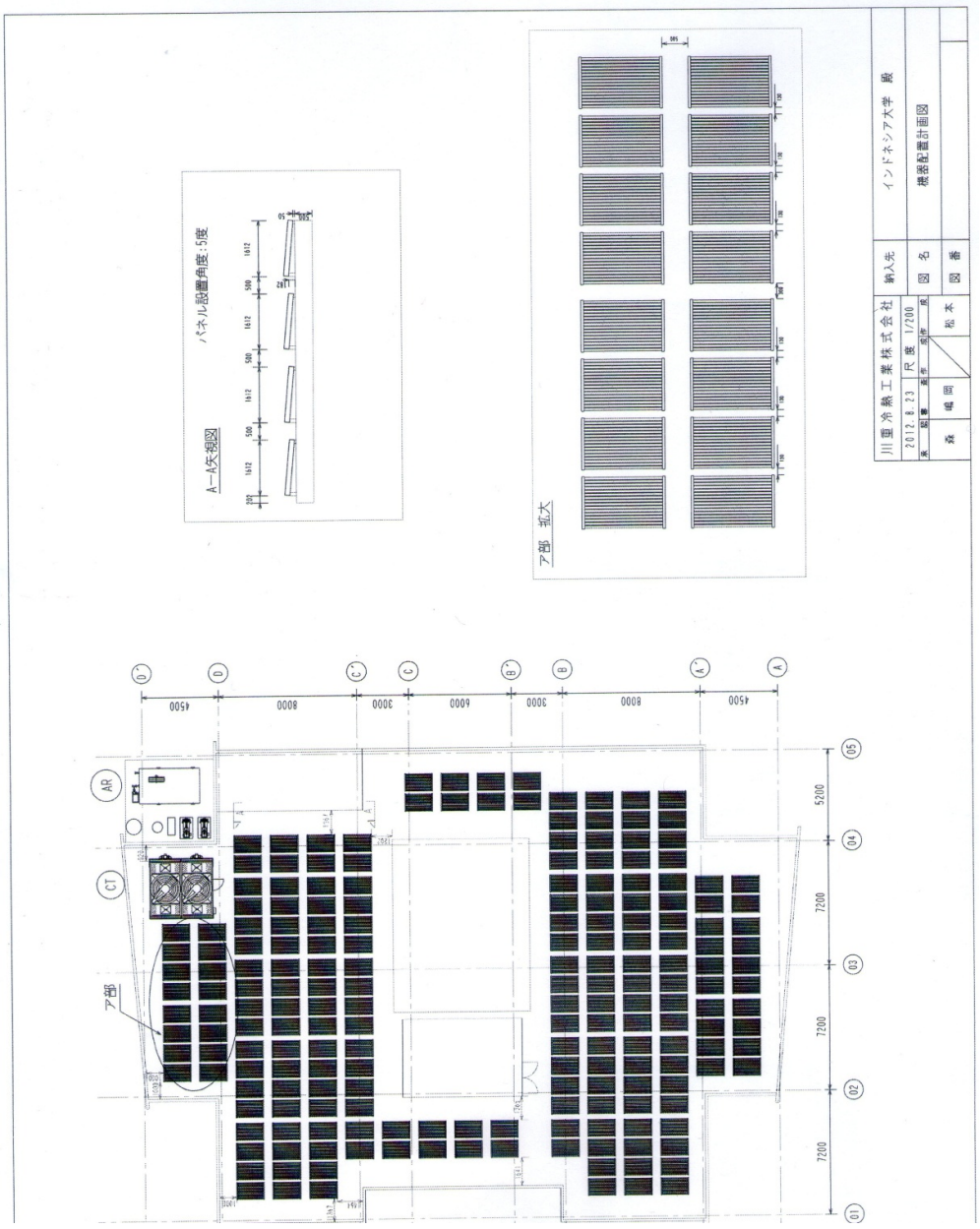

A. 2.5 Ebara end suction volute pumps 80x65FS4K611

エバラＦＳ型片吸込渦巻ポンプ
EBARA END SUCTION VOLUTE PUMPS

④冷却水ポンプ資料

外形寸法図
DIMENSIONS

機名 MODEL 80X65FS4K611　　周波数 FREQUENCY 60 Hz　　出力 OUTPUT 11 kW

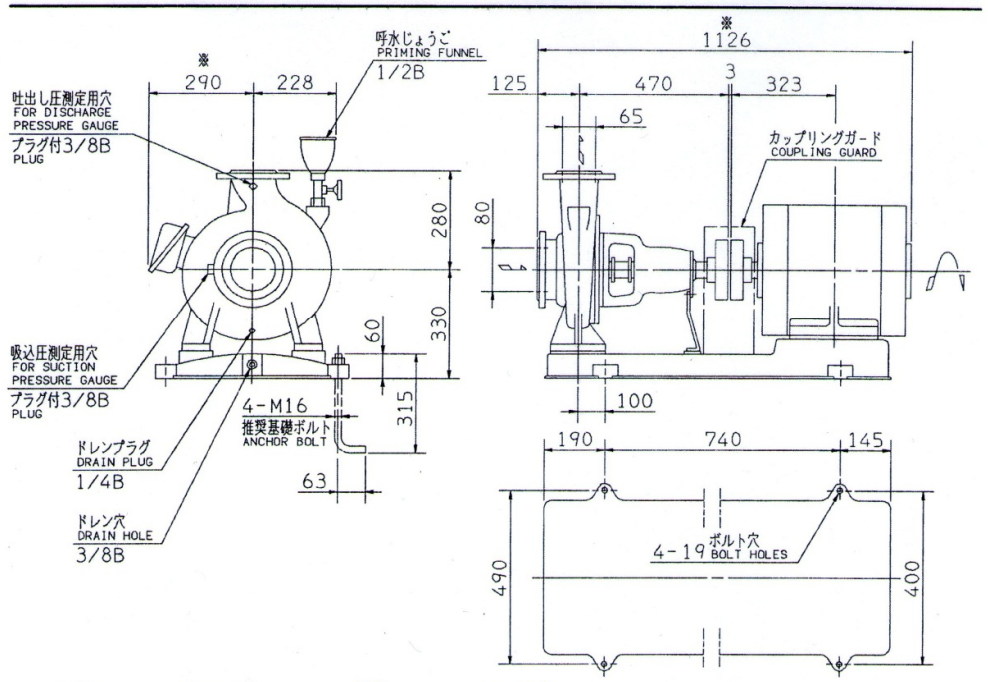

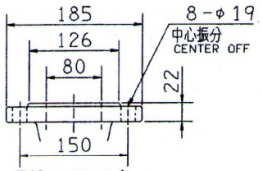

吸込フランジ
SUCTION FLANGE

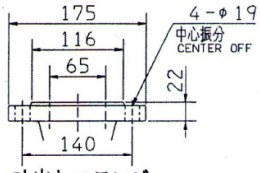

吐出しフランジ
DISCHARGE FLANGE

注) NOTE
1. 電動機仕様 : 三相誘導電動機
MOTOR SPEC. THREE PHASE INDUCTION MOTOR.
形式 TYPE : 防滴保護形 O.D.P.
2. ※印の値は、概略値を示します。
DIMENSIONS MARKED ※ INDICATE ROUGH VALUE.

質量 MASS ※223 kg

標準附属品 STANDARD ACCESSORIES				特別附属品 SPECIAL ACCESSORIES		電動機 MOTOR		特殊仕様 SPECIAL SPEC.
1	共通ベース COMMON BASE	8		1		周波数 Hz	Hz	
2	呼水じょうご PRIMING FUNNEL	9		2		電圧 V	V	
3	カップリング SHAFT COUPLING	10		3		出力 kW	kW	
4	カップリングガード COUPLING GUARD	11		4		形式 TYPE		
5	ガスケット GASKET	12		5		メーカ MAKER		
6		13		6				
7		14		7				

御注文主 CUSTOMER			機器番号 ITEM NO.			
御使用先 FINAL USER			機器名称 ITEM NAME			
在原製番 SER.NO.	機名 MODEL	吐出し量 CAPACITY	全揚程 TOTAL HEAD	同期速度 SPEED min-1	出力 OUTPUT	数量 Q'TY

図番 DWG.NO. D80X65FS4K611 002

EBARA

EBARA CORPORATION

MFS-D031

090707

エバラFS型片吸込渦巻ポンプ
EBARA END SUCTION VOLUTE PUMPS

④冷却水ポンプ資料

代表性能曲線
PERFORMANCE CURVE

機名 MODEL 80X65FS4K611　　周波数 FREQUENCY 60 Hz　　出力 OUTPUT 11 kW

電動機定格 MOTOR RATING　200 V　40.8 A　1735 min⁻¹ / 400 V　20.4 A　1735 min⁻¹　11 kW　形式 TYPE 防滴保護形 O.D.P.

本図はエバラ標準電動機を使用した場合のデータです

番号 TEST NO.	ポンプ PUMP			三相誘導電動機 MOTOR						
				電圧 VOLTS (200V)			電圧 VOLTS (400V)			
	吐出し量 CAPACITY	全揚程 TOTAL HEAD	効率 EFF.	電流 CURRENT	入力 INPUT	効率 EFF.	電流 CURRENT	入力 INPUT	効率 EFF.	出力 OUTPUT
	l/min	m	%	A	kW	%	A	kW	%	kW
1	0	40.6	0.0	14.81	3.46	88.5	7.41	3.46	88.5	3.06
2	500	39.5	54.3	22.53	6.44	92.0	11.27	6.44	92.0	5.92
3	1000	35.5	68.6	30.58	9.17	92.0	15.29	9.17	92.0	8.43
4	1500	27.5	66.2	36.66	11.10	91.5	18.33	11.10	91.5	10.15
5	1800	15.0	43.1	36.86	11.15	91.5	18.43	11.15	91.5	10.20

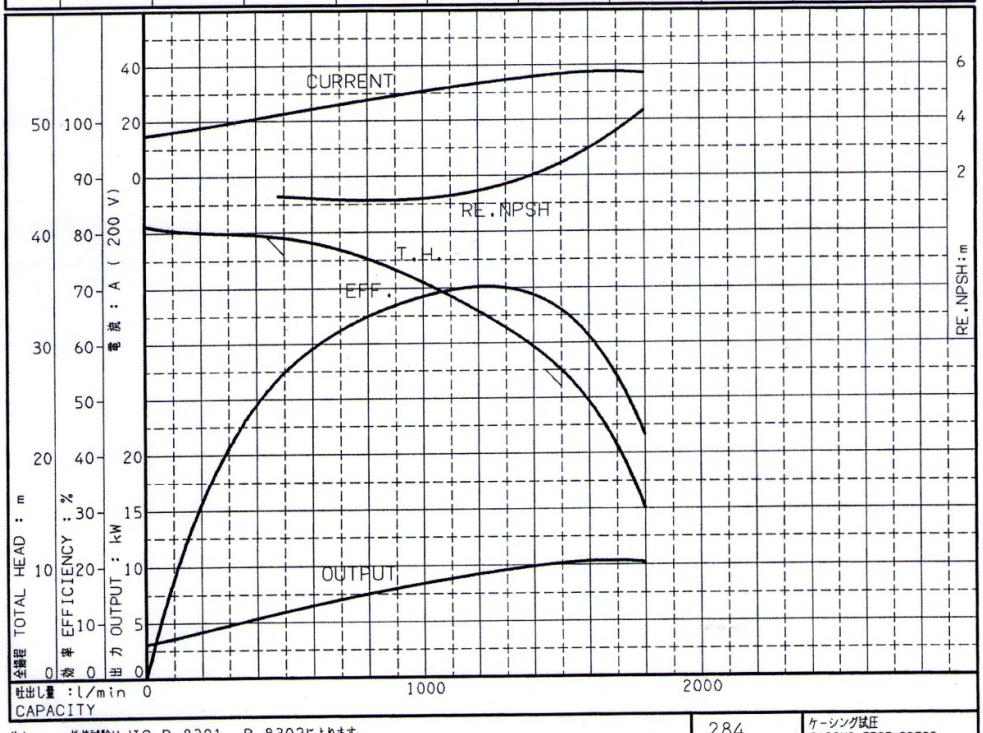

注) 性能試験はJIS B 8301, B 8302によります。

NOTE THIS CURVE IS BASED ON JIS TESTING CODE (B 8301,B 8302).

284

ケーシング試圧 CASING TEST PRESS. 1.50 MPa

御注文主 CUSTOMER
御使用先 FINAL USER

機器番号 ITEM NO.
機器名称 ITEM NAME

在原製番 SER.NO.	機名 MODEL	吐出し量 CAPACITY	全揚程 TOTAL HEAD	同期速度 SPEED min⁻¹	出力 OUTPUT	数量 QUANTITY

図番 DWG.NO. P80X65FS4K611 000

EBARA

EBARA CORPORATION

A4-201
010330

A. 2.6 Ebara end suction volute pumps 65x50FS4J

エバラFS型片吸込渦巻ポンプ
EBARA END SUCTION VOLUTE PUMPS

④冷却水ポンプ資料

断　面　図
SECTIONAL VIEW

適用範囲 APPLICATION　65×50FS4J
80×65FS4H,4J,4K

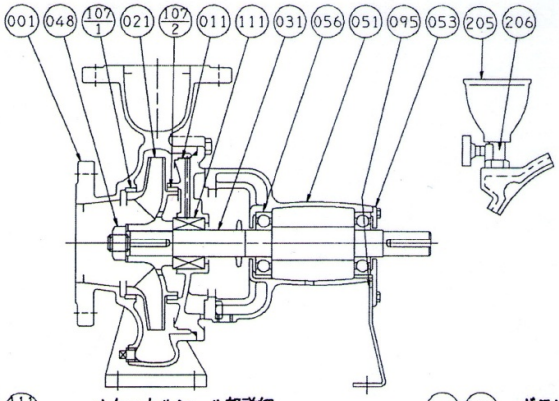

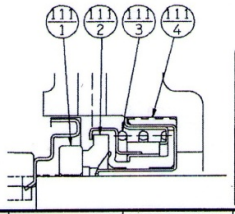

メカニカルシール部詳細
MECHANICAL SEAL DETAIL

番号 PART NO.	部品名 PART NAME	材料 MATERIAL
111-1	回転リング MATING RING	セラミック CERAMIC
111-2	シールリング SEAL RING	カーボン CARBON GRAPHITE
111-3	スプリング SPRING	SUS304 304 STAINLESS
111-4	パッキン PACKING	ゴム/NBR RUBBER/NBR

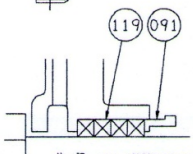

グランドパッキン仕様（特殊仕様）
GLAND PACKINGS SPECIFICATION (OPTION)

番号 PART NO.	部品名 PART NAME	材料 MATERIAL	個数 NO.FOR 1UNIT
119	グランドパッキン GLAND PACKING	炭化繊維 CARBONIZED FIBER	4

注記 NOTE
※1：軸封がグランドパッキン仕様 FOR ONLY GLAND PACKING SPECIFICATION
※2：全鉄仕様は軸封部グランドパッキン仕様 ALL IRON PARTS FOR ONLY GLAND PACKING SPECIFICATION

番号	部品名		標準仕様 STANDARD		全鉄仕様※2 ALL IRON		主軸材料 SUS304 304 STAINLESS SHAFT				個数 NO.FOR 1 UNIT
	PART NO.	PART NAME	材料 MATERIAL								
206	呼水弁	PRIMING VALVE	C3771BD	BRASS	FC150 SUS304	CAST IRON 304STAINLESS	C3771BD	BRASS			1
205	呼水じょうご	PRIMING FUNNEL	合成樹脂	PLASTIC	合成樹脂	PLASTIC	合成樹脂	PLASTIC			1
111	メカニカルシール	MECHANICAL SEAL	セラミック/カーボン	CERAMIC/ CARBON GRAPHITE	※2		セラミック/カーボン	CERAMIC/ CARBON GRAPHITE			1組※2 1SET
107-2	ライナリング	CASING RING	CAC406	BRONZE	FC150	CAST IRON	CAC406	BRONZE			1
107-1	ライナリング	CASING RING	CAC406	BRONZE	FC150	CAST IRON	CAC406	BRONZE			1
095	支柱	STAY	SS	STEEL	SS	STEEL	SS	STEEL			1
091	パッキン押え※1	GLAND	C3771BE	BRASS	FC150	CAST IRON	C3771BE	BRASS			1
056	玉軸受	BALL BEARING									2
053	軸受カバー	BEARING COVER	FC150	CAST IRON	FC150	CAST IRON	FC150	CAST IRON			1
051	軸受ケーシング	BEARING HOUSING	FC150	CAST IRON	FC150	CAST IRON	FC150	CAST IRON			1
048	羽根車ナット	IMPELLER NUT	C3604BD	BRASS	SUS304	304 STAINLESS	C3604BD	BRASS			1
031	主軸	SHAFT	SUS403	403 STAINLESS	SUS403	403 STAINLESS	SUS304	304 STAINLESS			1
021	羽根車	IMPELLER	CAC406	BRONZE	FC150	CAST IRON	CAC406	BRONZE			1
011	ケーシングカバー	CASING COVER	FC200	CAST IRON	FC200	CAST IRON	FC200	CAST IRON			1
001	ケーシング	CASING	FC200	CAST IRON	FC200	CAST IRON	FC200	CAST IRON			1

御注文主 CUSTOMER		機器番号 ITEM NO.	
御使用先 FINAL USER		機器名称 ITEM NAME	

荏原製番 SER.NO.	機名 MODEL	吐出し量 CAPACITY	全揚程 TOTAL HEAD	同期速度 SPEED min⁻¹	出力 OUTPUT	数量 Q'TY

図番 DWG.NO.	VFS-4411	002

EBARA

EBARA CORPORATION

VFS-4411

041130

A. 2.7 Cooling tower

Truwater Cooling Towers Sdn Bhd
Exec. Suite 702, Block B, Kelana Business Centre
97, Jalan SS 7/2, Kelana Jaya, 47301 Petaling Jaya.
Tel : 603-7880 8800 Fax : 603-7804 5519
www.truwater.com.my

TRUWATER

Project Details

Customer : M.IDRUS
Project :
Location :
Industry :
Reference :
Remarks :

Selection Results

	SI Unit	IP Unit
Hot Water Temperature	37.60 °C	99.68 °F
Cold Water Temperature	30.00 °C	86.00 °F
Wet Bulb Temperature	28.00 °C	82.40 °F
Flowrate	80.00 m3/hr	352.00 usgpm
Range	7.6	13.7
Series	TXS	

Model	Cell	Motor-kW	
TXS 250-1L	1	7.5	✓
TXS 250-2L	2	3.7	
TXS 300-2L	2	3.7	
TXS 300-1L	1	11.0	
TXS 300-3L	3	2.2	

Printed Date 21 Dec 2012 09:42

Page 1 of

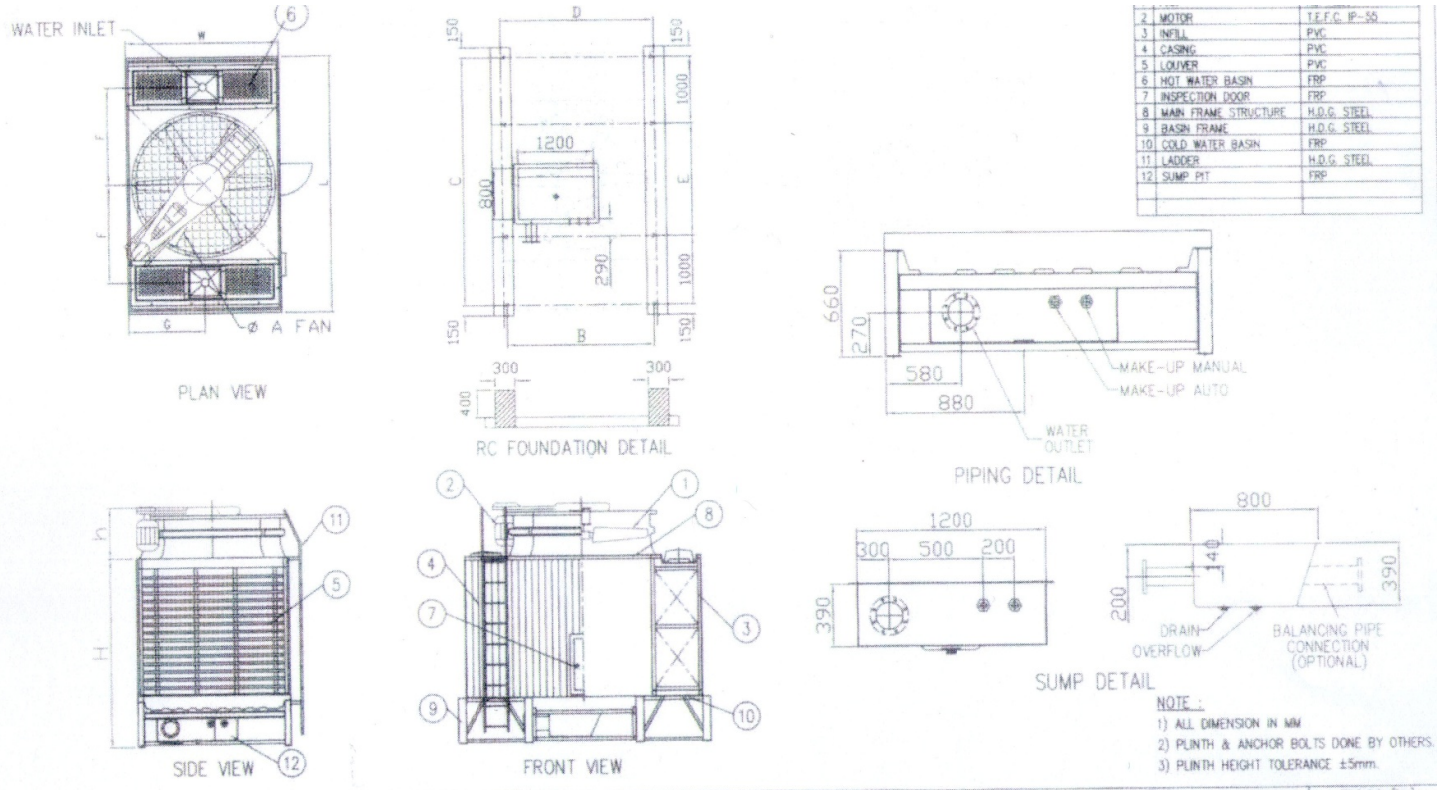

2	MOTOR	T.E.F.C. IP-55
3	INFILL	PVC
4	CASING	PVC
5	LOUVER	PVC
6	HOT WATER BASIN	FRP
7	INSPECTION DOOR	FRP
8	MAIN FRAME STRUCTURE	H.D.G. STEEL
9	BASIN FRAME	H.D.G. STEEL
10	COLD WATER BASIN	FRP
11	LADDER	H.D.G. STEEL
12	SUMP PIT	FRP

NOTE :
1) ALL DIMENSION IN MM
2) PLINTH & ANCHOR BOLTS DONE BY OTHERS.
3) PLINTH HEIGHT TOLERANCE ±5mm.

TOWER MODEL	Motor Kw/cell	Overall Dimension					Anchor Bolts Data				Piping Data			Piping Size					Weight (kg)	
		L	W	H	h	A	B	C	D	E	F	G	J	Water Inlet	Water Outlet	Over Flow	Drain	Make up Auto & manual	Dry Weight	Operatin Weight
XS 250-1L	7.5	3770	2280	2750	750	2000	2180	3650	2280	1650	1435	1140	–	125 x 2	200 x 1	50 x 1	50 x 1	50 x 1	1,190	3,200

TRUWATER
providing solutions to your cooling needs

Truwater Cooling Towers Sdn Bhd
Executive Suite 702, Block B,
Kelana Business Center, No.97, Jalan SS7/2,
47301 P.J. Selangor Darul Ehsan,Malaysia.

Telephone: 603-7880 8800 (4 Lines)
Fax: 603-7804 3519
E-mail : TW.Cooling@truwater.com.my

SCALE	DESIGNED BY	DRAWN BY	CHECKED BY	APPROVED BY
N.T.S.	BH CHEONG	WH TAP	TS LIN	EP TAN
DATE	20.7.2009	10.8.2009	1.9.2009	14.9.2009
OUR REF			YOUR REF	

REV NO :
REV DATE :
DRAWING NO :
CLIENT :
PROJECT :

TITLE :
PROPOSED GENERAL ARRANGEMENT & RC FOUNDATION FOR COOLING TOWER MODEL TXS 250-1L

A. 2.8 Fan coil unit

AICOOL

TÜV EN ISO 9001 no. 16 100 0256

DUCTED SPLIT

30.000 Btu/hr ...
750.000 Btu/hr

FD

R22, R134a, R407C

MADE IN INDONESIA BEST PERFORMANCE

Every Cooling Solution... We Have It

AICOOL

STANDARD FEATURES

Introduction
The AICOOL CU/FD air cooled ducted split air conditioner is special engineered to match latest requirements in medium commercial and light industrial application. These new series offer a generous a wide range of cooling capacity from 30 up to 750 MBH.

Using high quality components with international standard ISO, CE, GS, TUV, ULetc., CU/FD new series ensure a reliable heavy duty better efficiency unit in it's class. Compactness, modular design, easy access for installation and maintenance, heavy gauge generous material are the based characters of the its superior design.

The CFU/FD series are designed in simple modular form. Multiple outdoor units of bigger capacity give the flexibility in installation and maintenance. The compact design of the indoor and outdoor units optimize space for shipment and require only minimal installation space.

Performance The cooling capacity is rated according to ARI standard, using R22 - refrigerant.
Easy Maintenance The service-oriented design concept provides easy access to the components, by removing the front panel.
Cabinet The cabinet is made of heavy gauge galvanized steel, powder coating finished, providing optimum corrosion resistance.
Compressor Fully sealed hermetic scroll compressor with suction gas cooled motor windings, is single powered up to 15 HP, internal thermal protected, optimized for high tropical ambient, provides the units high EER.

Air Cooled Condenser
Air standard condenser coils have a generous 12 fpi, large enough to prevent from dust blocking of the fins, easy to clean, are made of inner grooved seamless copper tube arranged in staggered pattern, mechanically expanded into aluminium fins, leakage tested by 35 bars.

Dual speed 3 phase high efficiency external rotor condenser axial fan, well known for best quality, low noise level, energy saving and superior robust design, high ambient resistance up to 60 C, IP 54 motor thermal protected and insulated class F (DIN EN 60034-1)

Indoor Units
All standard evaporator coils are designed with such large face area, to prevent from carry over of condensation water into the air duct system, made of inner grooved seamless copper tube arranged in staggered pattern, mechanically expanded into aluminium fins, leakage tested by 35 bars. Drain pan is double skinned insulated of 10 mm thick PE foam with 0.12 gr/mm^3 density.

Thermal expansion valves are essential for stabile operation even in changing conditions and part load.
All FD up to 600 MBH supplied with forward curve centrifugal direct driven fans, no need readjustment, therefore applicable for clean room applicatin. The indoor fans provide sufficient external static pressure at minimal energy consumption.

Air Filter High performance filter media about durable thermal bonded filters (100% polyesther), free of silicon, can be cleaned by beating or washing.
Refrigerant circuit The outdoor and indoor units are factory N_2 pre-charged, pressure tested and includes an initial oil charge. Single refrigerant circuit designs up to 150 MBH capacity. High and Low Pressure Switch supplied. Flare connection for suction pipe and valve for liquid pipe.
Electrical circuit Electrical panel supplied with overload, delay starter, phase failure and room thermostat, easy wiring.

OPTIONAL FEATURES

- Higher grade air filter up to H15 class (Hepa filter)
- Higher external static pressure
- Epoxy coated aluminum fins or copper fins.
- Double skinned with up to 50 mm PE insulation.
- Suction and discharge pressure gauge, filter dryer, sight glass and liquid valve.
- Stepless fan speed controller, compressor inverter technology
- Other refrigerant, R134a, R507c, R404a on request.

AICOOL reserves the right to change in specifications without prior notice

SPECIFICATION DATA

DUCTED SPLIT AIR CONDITIONING UNIT

AICOOL

Model		Outdoor	CU 32	CU 42	CU 52	CU 62	CU 77	CU 102	CU 127	CU 152	CU 202	CU 252	CU 302	CU 252 + CU 102	CU 202 (2)	CU 252 + CU 202	CU 252 (2)	CU 302 (2)	CU 252 (3)
		Indoor	FD 32	FD 42	FD 52	FD 62	FD 77	FD 102	FD 127	FD 152	FD 202	FD 252	FD 302	FD 352	FD 402	FD 452	FD 502	FD 602	FD 752
Cooling Capacity		Btu/h	30,000	40,000	50,000	60,000	75,000	100,000	125,000	150,000	200,000	250,000	300,000	350,000	400,000	450,000	500,000	600,000	750,000
		TR	2.5	3.3	4.2	5.0	6.3	8.3	10.4	12.5	16.7	20.8	25.0	29.2	33.3	37.5	41.7	50.0	62.5
Refrigerant			R22																
Refrigerant Control			Thermostatic Expansion Valve																
Power Supply		V/Ph/Hz	380 Volt / 3 Phase / 50 Hertz																
Pipe Connection	Liquid	Inch	3/8	3/8	1/2	1/2	5/8	5/8	5/8	3/4	5/8	5/8	3/4	5/8	5/8	5/8	5/8	3/4	5/8
	Suction	Inch	5/8	5/8	3/4	7/8	1 1/8	1 3/8	1 3/8	1 5/8	1 3/8	1 3/8	1 5/8	1 3/8	1 3/8	1 3/8	1 3/8	1 5/8	1 3/8
Outdoor Unit																			
Compressor	Type		Hermetic Scroll																
	Protection Device		Phase Protector, Thermal Overload Relay, High and Low Pressure Control																
	Quantity	Pcs	1	1	1	1	1	1	1	1	2	2	2	3	4	4	4	4	6
	Nominal Motor	HP	3	4	5	6	7.5	10	12.5	15	20	25	30	35	40	45	50	60	75
	Power Input	kW	2.7	3.43	4.17	4.96	6.54	8.96	10.8	13.62	8.96 (2)	10.8 (2)	13.6 (2)	10.8 (2) + 8.9	8.96 (4)	10.8(2)+8.9(2)	10.8 (4)	13.6 (4)	10.8 (6)
	Rated Load Ampere	A	5.7	7.2	8.2	10	12.1	20.7	22.9	30.3	20.7 (2)	22.9 (2)	30.3 (2)	22.9 (2) + 20.7	20.7 (4)	22.9 (2) + 20.7 (2)	22.9 (4)	30.3 (4)	22.9 (6)
	Locked Rotor Ampere	A	40	48	61.8	65.5	98	130	145	175	130 (2)	145 (2)	175 (2)	145 (2) + 130	130 (4)	145 (2) + 130 (2)	145 (4)	175 (4)	145 (6)
Coil	Material		Aluminum Fins on Inner Grooved Copper Tubes																
	Face Area	m^2	18.2	23.6	35.4	42.5	47.3	71	82.6	105.5	151.4	169.1	183.4	169.1 + 71	151.4 (2)	169.1 + 151.4	169.1 (2)	183.4 (2)	169.1 (3)
Fan	Type		Axial Fan with External Rotor Motor																
	Diameter	mm	500	500	500	500	630	630	630	630	630	630	630	630	630	630	630	630	630
	Quantity	Pcs	1	1	2	2	1	1	1	1	1	2	2	2 + 1	1 + 1	2 + 2	2 + 2	2 + 2	2 + 2 + 2
	Power Input	kW	0.4	0.4	0.8	0.8	0.72	0.72	1.35	1.9	1.9	0.72 (2)	1.9 (2)	0.72 (3)	1.9 (2)	0.72 (2) + 1.9	0.72 (4)	1.9 (4)	0.72 (6)
	Rated Load Ampere	A	0.94	0.94	1.88	1.88	1.4	1.4	2.2	3.2	3.61	1.34 (2)	3.61 (2)	1.34 (3)	3.61 (2)	1.34 (2) + 3.61	1.34 (4)	3.61 (4)	1.34 (6)
Dimension	Width	mm	896	896	896	960	1,200	1,200	1,200	1,170	1,170	2,000	2,000	2,000 1,200	1,170 (2)	2,000 1,170	2,000 (2)	2,000 (2)	2,000 (3)
	Length	mm	330	330	330	375	600	600	600	1,100	1,100	1,100	1,100	1,100 600	1,100 (2)	1,100 1,100	1,100 (2)	1,100 (2)	1,100 (3)
	Height	mm	705	705	1,105	1,218	950	950	1,050	950	950	1,050	950	1,050 950	950 (2)	1,050 950	1,050 (2)	950 (2)	1,050 (3)
Weight		kg	105	110	143	167	187	205	220	286	330	400	550	400 + 205	330 (2)	400 + 330	400 (2)	550 (2)	400 (3)
Indoor Unit																			
Coil	Material		Aluminum Fins on Inner Grooved Copper Tubes																
	Face Area	m^2	16.5	16.5	27.1	27.1	31.8	39.8	53.1	63.7	106.2	127.4	148.6	173.4	198.2	217	244.2	289.4	361.7
Fan	Type		Direct Driven - Forward Curved Centrifugal Fan											Belt Driven - Forward Curved Centrifugal Fan					
	Airflow	CFM	1,100	1,100	1,900	1,900	2,100	2,700	3,900	5,050	7,060	7,650	9,000	10,600	12,300	12,300	12,300	13,500	17,600
		CMH	1,870	1,870	3,230	3,230	3,570	4,590	6,630	8,585	12,002	13,005	15,300	18,020	20,910	20,910	20,910	22,950	29,920
	External Static Pressure	in WG	0.3	0.3	0.4	0.4	0.8	0.8	0.6	1.2	1.2	1.2	1.2	1.2	1.6	1.6	1.6	1.4	1.6
		Pa	80	80	110	110	200	200	150	300	300	300	300	300	400	400	400	350	400
	Diameter	mm	225	225	250	250	280	315	315	355	355	355	400	500	500	500	500	560	630
	Quantity	Pcs	1	1	1	1	1	1	1	1	2	2	2	1	1	1	1	1	1
	Power Input	kW	0.25	0.37	0.55	0.55	0.8	1.1	1.5	1.8	1.1 (2)	1.5 (2)	1.8 (2)	4	5.5	7.5	7.5	11	15
	Rated Load Ampere	A	0.95	0.98	1.55	1.73	2.13	3.18	4.19	4.92	3.18 (2)	4.19 (2)	5.02 (2)	8.36	12.1	15.6	15.6	21.8	29.3
Dimension	Width	mm	900	900	1,350	1,350	1,400	1,400	1,700	1,700	2,200	2,200	2,400	2,200	2,400	2,400	2,400	2,400	2,600
	Length	mm	650	650	700	700	830	950	1,030	1,030	1,030	1,065	1,065	1,250	1,400	1,400	1,400	1,400	1,800
	Height	mm	510	510	510	510	590	635	730	730	750	850	950	1,140	1,240	1,390	1,390	1,390	1,540
Duct Connection	Supply	mm	258 x246	258 x246	321 x273	321 x273	300 x305	338 x338	400 x338	431 x375	1300 x338	1400 x375	1400 x375	638 x638	638 x638	638 x638	638 x638	715 x715	801 x801
	Return	mm	800 x370	800 x370	1250 x370	1250 x370	1300 x440	1300 x495	1600 x570	1600 x570	2100 x590	2100 x700	2300 x790	2100 x695	2300 x980	2300 x1080	2300 x1080	2300 x1080	2400 x1280
Weight		kg	67	70	88	92	116	146	180	185	254	302	349	389	437	493	509	580	683

* Nominal Cooling Capacity Conditions: Evaporator Air Inlet Temp. 26.6°C / 55%; Evap. Temp. 7.2 °C and Cond. Temp. 50 °C
We improve our products continuously, therefore we reserve the right to make modifications without prior notice.

FD/APR07-R3

A. 2.9 Single-double-effect absorption chiller KTE

Features Air Conditioning using Solar Thermal Energy

- Freon Free:
  Absorption chiller-heaters contain "water" as refrigerant and Freon gas, which has high global warming potential, is not used.
- Low Electricity Consumption:
  Absorption chiller-heaters provide chilled water by means of renewable energy or natural gas combustion, which contributes to significant reduction of electricity consumption.
- Application for Solar Thermal Energy:
  Solar absorption chiller-heaters preferentially utilize solar thermal energy, which can reduce consumption of natural gas.
- The lower limit temperature of the solar hot water is "75˚C".
- The base model is a worldly high efficient machine with high COP and CO_2 emission can be reduced.
- Waste heat from Gas Engine or Gas Turbine Co-generation system is also applicable.

Basic Concept or Summary

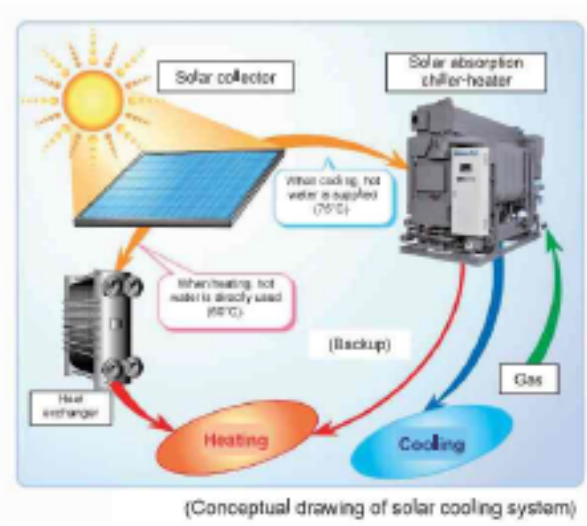

(Conceptual drawing of solar cooling system)

- The hot water heated by the solar thermal energy through solar collectors is supplied to the solar absorption chiller-heater. The solar absorption chiller-heater thermally recovers heat from hot water and exchanges it to lithium bromide solution in the machine, and then the natural gas consumption is reduced.
- As the solar absorption chiller itself is equipped with a burner, which provides combustion heat necessary in the machine, back-up system is not necessary even if the solar heat is insufficient. Furthermore, as hot water by the solar heat is preferentially used, the cooling operation is possible with the solar heat alone when cooling load is low.
- The newly developed heat exchanger specifically for the solar hot water has realized to set lower limit temperature up to "75˚C". (The previous lower limit temperature for hot water recovery was "83˚C".)
- For the heating in winter, the solar hot water can be supplied for the heating.

Great reduction of natural gas consumption can be realized by utilizing hot water by the solar thermal energy.

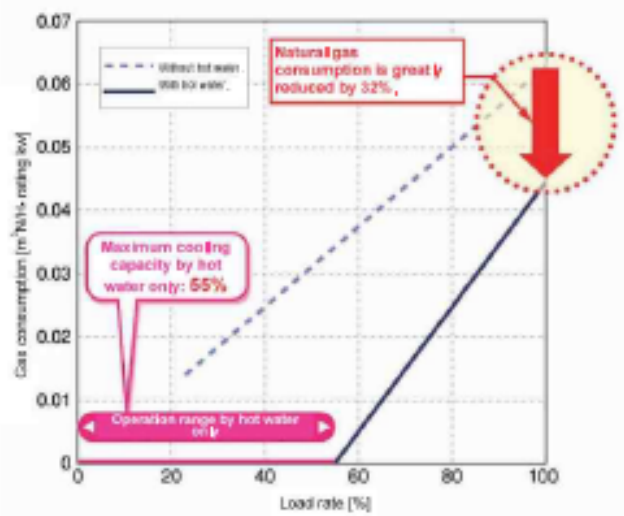

- Natural gas consumption at a rated operation can be saved by 32% compared with the base type.
  (In the case that hot water inlet temperature is 90°C.)
- The Maximum cooling capacity with hot water only is "55%".
  (In the case that hot water inlet temperature is 90°C.)
  <Example> In the case of 100 RT, the machine is capable to supply chilled water up to 55 RT by hot water only.
- CO_2 emission can be significantly reduced by solar thermal energy compared with the direct fired type.
- Total motor output is only "4.85 kW in the case of 185 RT.

Installation in Practice or Schedule

Domestic

Launched in June 2010.

Overseas

Launched in June 2010.

Contact: **Sales, Service Management Department, Kawasaki Thermal Engineering**
Tel: +81.3.3615.5821 Fax: +81.3.3615.5822
URL: http://www.khi.co.jp/english/index.html

Specifications

Items			Model	TZU80	TZU100	TZU120	TZU150	TZU180	TZU210	TZU250	TZU300
Capacity	Cooling		kW	281	352	422	528	633	739	879	1055
			(USRT)	80	100	120	150	180	210	250	300
	Heating		kW	196	233	280	350	419	490	583	699
			(Mcal/h)	169	200	241	301	360	421	501	601
Chilled (Hot)	Inlet – Outlet Temp.		℃	15.0 → 7.0							
	Inlet – Outlet Temp.		℃	54.7 → 60.0							
	Flow Rate		m³/h	39.2	37.8	45.4	56.7	68	79.4	94.5	113.4
	Pressure Loss		kPa	43.3	41.5	38.6	39.5	45.8	47.3	51.8	56.3
	Retained Water Volume		m³	0.12	0.14	0.16	0.18	0.27	0.29	0.34	0.38
Cooling	Inlet – Outlet Temp.		℃	32.0 → 37.6							
	Flow Rate		m³/h	80	100	120	150	180	210	250	300
	Pressure Loss		kPa	124.8	132.0	125.8	148.9	88.3	99.3	108.8	129.5
	Retained Water Volume		m³	0.29	0.33	0.38	0.44	0.67	0.74	0.85	0.98
Solar Hot Water	Inlet – Outlet Temp.		℃	90.0 → 79.5							
	Flow Rate		m³/h	9.2	11.5	13.8	17.3	20.7	24.2	28.8	34.5
	Heat Recovery Rate		kW	112	140	168	211	253	295	351	421
			Mcal/h	97	121	145	181	217	254	302	362
	Pressure Loss		kPa	35.2	48.5	22.0	31.6	21.5	27.0	45.0	58.7
	Retained Water Volume		m³	0.08	0.09	0.11	0.12	0.16	0.18	0.21	0.24
Fuel	With Solar Hot Water		m³N/h	11.8	14.7	17.7	22.1	26.5	30.9	36.8	44.1
	Without Solar Hot Water		m³N/h	17.3	21.6	26.4	32.5	38.9	45.4	54.1	64.9
	Gas Inlet Pressure		kPa	1.96							
Electricity	Power Source		–	200V 3 φ							
	Capacity (50Hz/60Hz)		kVA	5.7/5.7	5.7/5.7	8.4/8.4	8.4/8.4	9.5/9.4	10.5/10.4	13.0/12.8	13.0/12.8
	Current (50Hz/60Hz)		A	18.2/18.2	18.2/18.2	25.9/25.9	25.9/25.9	29.1/28.9	31.9/31.6	39.3/38.6	39.3/38.6
	Motor Power (50Hz/60Hz)		kW	2.25/2.25	2.25/2.25	4.1/4.1	4.1/4.1	4.85/4.85	5.6/5.6	7.1/7.1	7.1/7.1
Connection	Chilled (Hot) W. In/Out		A	100	100	125	125	150	150	200	200
	Cooling W. In/Out		A	125	125	125	125	150	150	200	200
	Solar Hot W. In/Out		A	40	40	50	50	65	65	65	65
	Fuel Gas Inlet		A	25	25	32	32	32	50	50	65
	Exhaust Gas Outlet		mm	100×700	100×730	100×550	100×550	100×650	100×650	115×850	115×850
Dimensions / Weight	Indoor Type	Length (L)	mm	3138	3138	3818	3818	3953	3953	5254	5254
		Width (W)	mm	1652	1852	1872	1879	2182	2200	2261	2286
		Height (H)	mm	2038	2038	2038	2038	2096	2096	2096	2096
		Operation Wt.	ton	7.3	7.6	9.2	9.7	12.7	13.1	16.2	16.9
		Shipping Wt.	ton	6.9	7.1	8.7	9.1	11.7	12.1	15	15.6
	Outdoor Type (with Casing)	Length (L)	mm	3600	3600	3698	3698	3856	3856	5166	5166
		Width (W)	mm	1944	1944	2014	2014	2460	2460	2574	2574
		Height (H)	mm	3072	3072	3073	3073	3345	3345	3345	3345
		Operation Wt.	ton	7.7	8	9.7	10.3	13.2	13.6	16.9	17.7
		Shipping Wt.	ton	7.3	7.5	9.2	9.6	12.3	12.6	15.8	16.4
Heat Transfer Area			m²	7.6	9.2	11.5	12.9	16.2	17.8	23.2	25.7
Energy Saving Rate			%	32							
Max. Cooling Cap. only Solar H.W.			%	55							

Specifications at the Inlet Temperature 75 degree C of Solar Hot Water

Items		Model	TZU80	TZU100	TZU120	TZU150	TZU180	TZU210	TZU250	TZU300
Solar H.W.	Inlet – Outlet Temp.	℃	75.0 → 71.9							
	Heat Recovery Rate	kW	33	41	50	62	75	87	104	124
		Mcal/h	29	36	43	53	64	75	89	107
Gas Consumption With Solar H.W.		m³N/h	15.7	19.7	23.7	29.6	35.4	41.3	49.2	59.1
Energy Saving Rate		%	9							
Max. Cooling Cap. only Solar H.W.		%	28							

TABLE LIST OF MAIN SPECIFICATIONS(SigmaAce1.43Solar)

Model				ΣTZU-80HQ9C		
Control Method		Capacity		PID Ctrl. for the Chilled Water Outlet Temp.		
		Combustion		ON-OFF Ctrl. + PID Ctrl. Method		
		Waste Heat Hot Water		ON-OFF Ctrl. + PID Ctrl. Method		
Capacity	Cooling		kW (*1)	239		
	Heating		kW (*1)	186		
Chilled and Hot Water	Chilled Wtr. Temp.		℃	Entering 15.0	Leaving 7.0	
	Hot Wtr. Temp.		℃	Entering 53.8	Leaving 60.0	
	Flow Rate		m3/h	25.7		
	Pressure Drop		kPa	30.4		
Cooling Water	Temperature		℃	Entering 32.0	Leaving 37.6	
	Flow Rate		m3/h	68.0		
	Pressure Drop		kPa	93.9		
Waste Heat Hot Water	Temperature		℃	Entering 90.0	Leaving 79.5	
	Flow Rate		m3/h	7.8		
	Pressure Drop		kPa	26.4		
Fuel	Fuel Consumption (*2)	Cooling (WITHOUT W. H. Hot Water)	MJ/h	662	NG	(598) 15.1 m3N/h
		Cooling (WITH W. H. Hot Water)	MJ/h	450	NG	(406) 10.3 m3N/h
		Heating (WITHOUT W. H. Hot Water)	MJ/h	778	NG	(703) 17.8 m3N/h
	Fuel Inlet Pressure		kPa	7.85		
	Air Required (*3)		m^3/h	243		
	Ex. Gas Vol. (*4)		m^3/h	347		
Electric	Power Source		———	3Phase	380V	50Hz
	Total Motor Power (*5)		kW	2.25		
	Capacity		kVA	5.8		
	Current		Amp	9.7		
Connec -tion	Chilled/Hot Wtr. In/Out		A	100		
	Cooling Wtr. In/Out		A	125		
	W. H. Hot Wtr. In/Out		A	40		(Standard Type)
	Fuel Inlet		A	50		
	Ex. Gas Outlet		mm×mm	—×—		
External Dimen -sions	Length (L)		mm	3,790		
	Width (W)		mm	2,198		
	Height (H)		mm	3,119		
Weight	Operation Weight		ton	8.0		
	Shipping weight (NET)		ton	7.5		
Energy Saving Rate (*5)			%	32		
Max. Cooling Capacity only Waste Heat Hot Water (*6)			%	33		

Appendix 3 Dimensional of single-double-effect absorption chiller

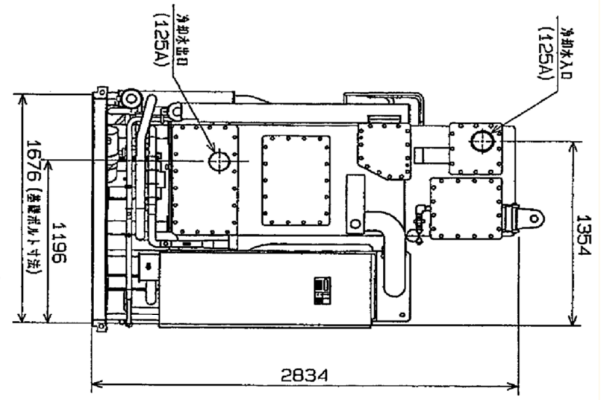

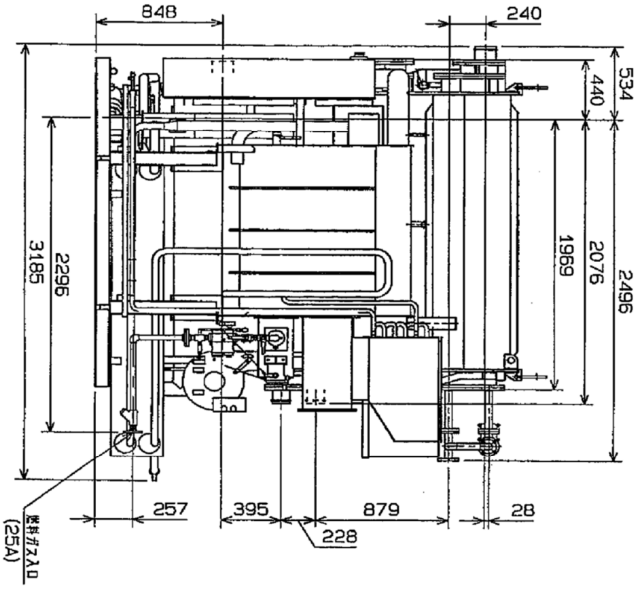

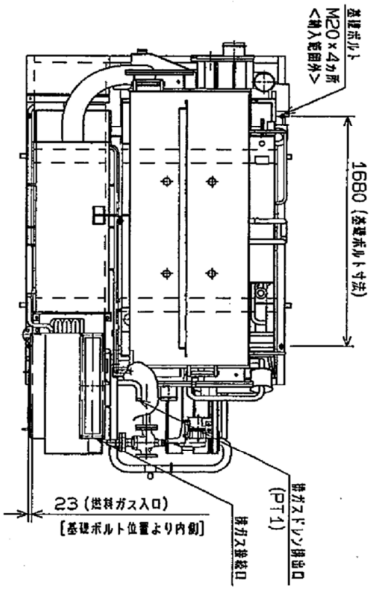

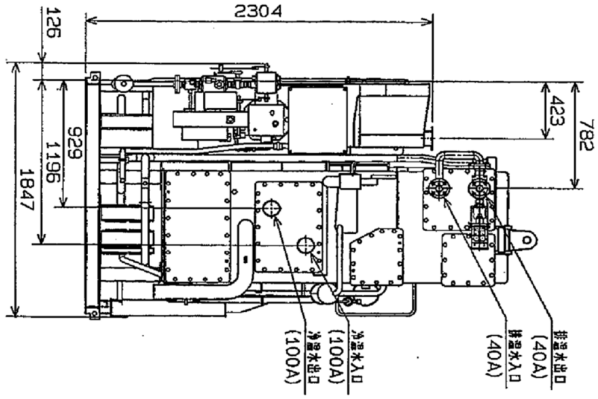

Performance data based on JIS (1)

Customer University of Indonesia 殿

Type Σ T Z U -80 H Q 9 C

Serial No. 94121

Condition Cooling 100% (Gas & Hot Water Combined)

Date 26/9/2013

1) Specification

Cooling	Qc0	239	kW				Electricity		380 V 50 Hz
Fuel Gas		13A		Press.	7.80	kPa	Moter & Control		
Heating Value(High)	Qg1	45.0	MJ/m^3_N	Qg0	450	MJ/h	A	2.25	kW
Fuel Gas Consumption		10.0	m^3_N/h	(100%)					
COP	COP0	2.08					Solar Heat	Qe0 92.4	kW

(COP based on JIS = Qc0/(Fuel Gas Input(LHV: Lower Heating Value) + Electricity Consumption))

*Without Solar Heat, Fuel Gas Only

2) Actual Data

Time	Chilled Water			Cooling Water		
	Flow Rate Wc ① m^3/h	Inlet Temp. tc1 ② ℃	Outlet Temp. tc2 ③ ℃	Flow Rate Wco ④ m^3/h	Inlet Temp. tco1 ⑤ ℃	Outlet Temp. tco2 ⑥ ℃
Spec.	25.7	15.0	7.0	68	32.0	37.6
Allowance	±5%	———	±0.5℃	±5%	±0.5℃	———
13 : 30	25.7	15.13	7.13	68.0	31.90	37.55
Average	25.7	15.13	7.13	68.0	31.90	37.55

Time	Solar Hot Water			Fuel Gas		
	Flow Rate We ⑦ m^3/h	Inlet Temp. te1 ⑧ ℃	Outlet Temp. te2 ⑨ ℃	Flow Rate Wg1 ⑩ m^3/h	Temperature td ⑪ ℃	Pressure Ps ⑫ kPa
Spec.	7.8	90	79.5	10.0 (m^3_N/h)		7.80
Allowance	±5%	±0.5℃	———	105%以下	———	———
13 : 30	7.8	90.0	79.4	11.0	26.0	7.68123
Average	7.8	89.98	79.37	11.0	26.0	7.68

Performance data based on JIS (2)

3) Calculation

1	Specific Heat(Chilled Wter)	Cc	4.20	kJ/(kg·K)	Average of Inlet and Outlet
2	Density(Chilled Water)	γc	998.9	kg/m³	Average of Inlet and Outlet
3	Higher Heating Value	Qg1	45.0	MJ/m³N	
4	Lower Heating Value	Qg2	40.6	MJ/m³N	
5	Fuel Gas Consumption	Wg1	10.0	m³N/h	Wg1=Qg0/Qg
6	Energy Input	Qi0	112.8	kW	Qi0=(1/3600)·Wg1·Qg2·1000
7	Gas Correction Factor	K1	0.982	–	K1=(101.325+Ps)/101.325·273/(273+td)
8	**Fuel Gas Consumption (Standard Condition)**	Wg	**10.04**	m³N/h	Wg=Wg1·K1·(1-L)
9	Heat loss rate	L	0.07	–	By calculation of Heat Loss
10	Electrisity Consumption	A	2.25	kW	Moter + Control
11	**Cooling Capacity**	Qc	**239.8**	kW	Qc=(1/3600)·Wc·Cc·γc·(tc1-tc2)
12		Qc/Qc0	**100.3**	%	> 95% (JIS B8622:2002 7.2)
13	**Heat Input**	Qi	**113.2**	kW	Qi=(1/3600)·Wg·Qg2·1000
14		Qi/Qi0	**100.4**	%	< 105% (JIS B8622:2002 7.4)
15	**COP**	COP	**2.08**		COP=Qc/(Qi+A)
16		COP/COP0	**100.0**	%	> 95% (JIS B8622:2002 7.5)
17	Specific Heat(Hot Wter)	Ce	4.19	kJ/(kg·K)	Average of Inlet and Outlet
18	Density(Hot Water)	γe	968.7	kg/m³	Average of Inlet and Outlet
19	**Heating Value(Hot Water)**	Qe	**93.3**	kW	Qe=(1/3600)·We·Ce·γe·(te1-te2)
20		Qe/Qe0	**100.92**	%	

早稲田大学　博士（工学）　学位申請　研究業績書

(List of research achievements for application of doctorate (Dr. of Engineering), Waseda University)

氏 名(ARNAS)　　印

（As of February, 2019）

種類別 (By Type)	題名、　発表・発行掲載誌名、　発表・発行年月、　連名者（申請者含む） (theme, journal name, date & year of publication, name of authors inc. yourself)
論文	
1	Operation performance enhancement of single-double-effect absorption chiller, Applied Energy 219 (2018), pp. 299–311, Arnas Lubis, Jongsoo Jeong, Niccolo Giannetti, Seiichi Yamaguchi, Kiyoshi Saito, Hajime Yabase, Muhammad Idrus Alhamid, Nasruddin. **Peer Reviewed**
2	Start-up behaviour of a combined air-conditioning system in cooling and heating operating modes, Energy and Buildings 158 (2018), pp. 1346–1357, Jongsoo Jeong, Arnas Lubis, Kiyoshi Saito, Sarngwoo Karng, Seoyoung Kim, Kwangho Kim. **Peer Reviewed**
3	Experimental performance of a double-lift absorption heat transformer for manufacturing-process steam generation, Energy Conversion and Management 148 (2017), pp. 267–278, Arnas Lubis, Niccolo Giannetti, Seiichi Yamaguchi, Kiyoshi Saito, Naoyuki Inoue. **Peer Reviewed**
4	Solar-assisted single-double-effect absorption chiller for use in Asian tropical climates, Renewable Energy 99 (2016), pp. 825–835, Arnas Lubis, Jongsoo Jeong, Kiyoshi Saito, Niccolo Giannetti, Hajime Yabase, Muhammad Idrus Alhamid, Nasruddin. **Peer Reviewed**
5	Entropy parameters for falling film absorber optimization, Applied Thermal Engineering 93 (2016), pp. 750–762, Niccolo Giannetti, Andrea Rocchetti, Arnas Lubis, Kiyoshi Saito, Seiichi Yamaguchi. **Peer Reviewed**
6	SOLAR AIR-CONDITIONING SYSTEM AT THE UNIVERSITY OF INDONESIA, International Journal of Technology (2016) 2: pp. 212-218, Hajime Yabase, Kiyoshi Saito, Arnas Lubis, Idrus Alhamid, Nasruddin. **Peer Reviewed**
国際発表	
7	Energy Saving on Solar Air-Conditioning System Using Single-Double-Effect Combined Absorption Chiller at Universitas Indonesia, 13th IIR – Gustav Lorentzen Conference on Natural Refrigerants 2018, M. Idrus Alhamid, Hajime Yabase, Kiyoshi Saito, Akira Hirai, Arnas, Nasruddin, Tatsuo Dantoku.
8	Effect of solar energy on high operation performance of single-double-effect absorption chiller, International Sorption Heat Pump Conference 2017, 7-10 August 2017, Arnas Lubis, Jongsoo JEONG, Kiyoshi SAITO, Hajime YABASE.
9	Single-double-effect absorption chiller performance by adjusting the combination of the solution mass flow rates, 5th IIR International Conference on Thermophysical Properties and Transfer Processes of Refrigerants, 23 – 26 April 2017, Arnas Lubis, Jongsoo Jeong, Kiyoshi Saito, Hajime Yabase, Muhammad Idrus Alhamid, Nasruddin.
10	Performance of solar air-conditioning system using absorption chiller. In ACRA 2016 - 8th Asian Conference on Refrigeration and Air-Conditioning (ACRA), Yabase, H., Hirai, A., Saito, K., Lubis, A., Alhamid, M. I.,Nasruddin, N.

早稲田大学　博士（工学）　学位申請　研究業績書

(List of research achievements for application of doctorate (Dr. of Engineering), Waseda University)

種類別 (By Type)	題名、　発表・発行掲載誌名、　発表・発行年月、　連名者（申請者含む） (theme, journal name, date & year of publication, name of authors inc. yourself)
発表 (11)	Performance improvement of single-double-effect absorption chiller by solution mass flow rate and distribution ratio controls, 第 27 回　環境工学総合シンポジウム 2017〔2017.7.10－7.12（静岡県浜松市）〕, Arnas Lubis, Jongsoo JEONG, Kiyoshi SAITO, Hajime YABASE.
(12)	Maximization of solar energy utilization on single-double-effect absorption chiller, 2016 年度日本冷凍空調学会年次大会講演論文集(2016.9.6- 9，神戸), Arnas Lubis, Jongsoo Jeong, Kiyoshi Saito, Hajime Yabase, Muhammad Idrus Alhamid, Nasruddin.
(13)	Application of single-double-effect absorption chiller to utilize solar energy in the tropical regions, 第 26 回　環境工学総合シンポジウム 2016〔2016.6.29－7.1（石川県金沢市下本多町）〕, Arnas Lubis, Jongsoo Jeong, Kiyoshi Saito, Hajime Yabase, Muhammad Idrus Alhamid, Nasruddin.
(14)	Performance Evaluation of Absorption Chiller Using Solar Energy in The Tropical Regions, 2015 年度日本冷凍空調学会年次大会講演論文集（2015.10.20- 23，東京）, Arnas Lubis, Jongsoo Jeong, Kiyoshi Saito, Hajime Yabase, Muhammad Idrus Alhamid, Nasruddin.
15	The Effect of Hot Water Flow Rate in The Solar Collector Flow Loop at Solar Thermal Cooling System, The 24th IIR International Congress of Refrigeration, August 16th – 22nd 2015, Nasruddin, Arnas, M. Idrus Alhamid, Kiyoshi SAITO, Hajime YABASE.
16	Performance of Solar Air-Conditioning System in Indonesia, QIR Annual Conference 2015 in Indonesia, H. Yabase, K. Saito, Arnas, M. Idrus Alhamid, Nasruddin.
(17)	Development of general–purpose energy system analysis simulator -ENEGY FLOW + M-Simulation of single-double effect absorption chiller type, 2014 年度日本冷凍空調学会年次大会講演論文集（2014.9.10- 13，佐賀）, Arnas, J. Jeong, K. Ohno, K. Saito, H. Yabase.
18	Field test of air conditioning system using solar absorption chiller in Indonesia, 2014 年度日本冷凍空調学会年次大会講演論文集（2014.9.10- 13，佐賀）, H. Yabase, A. Hirai, K. Saito, J. Jeong, K. Ohno, Arnas.